

THERMAL IMAGING
DURING LASER SURGERY

Brian James Gibson

Glasgow University

Department of Physics and Astronomy

1995

ProQuest Number: 11007817

All rights reserved

INFORMATION TO ALL USERS

The quality of this reproduction is dependent upon the quality of the copy submitted.

In the unlikely event that the author did not send a complete manuscript and there are missing pages, these will be noted. Also, if material had to be removed, a note will indicate the deletion.



ProQuest 11007817

Published by ProQuest LLC (2018). Copyright of the Dissertation is held by the Author.

All rights reserved.

This work is protected against unauthorized copying under Title 17, United States Code
Microform Edition © ProQuest LLC.

ProQuest LLC.
789 East Eisenhower Parkway
P.O. Box 1346
Ann Arbor, MI 48106 – 1346

Thesis
10288
Copy 1

GLASGOW
UNIVERSITY
LIBRARY

Abstract

This thesis considers the problems of remote temperature measurement, using a pyro-electric vidicon (PEV) to image small areas of biological tissue heated by laser irradiation. This is applied specifically to laser-assisted vascular anastomosis (LAVA), which is a surgical technique that aims to bond apposed tissue edges. It is a technique which has shown potential but the results have not been consistently successful. In order to understand the bond mechanism and to ascertain the optimum bond temperature, a number of authors have measured the temperature at the bond site using remote thermal imagers. However, if the limitations of the imager are not taken into account, then the temperature will be underestimated.

These limitations were investigated extensively for the PEV but the principles apply to all thermal imagers. In particular, a minimum source width of 6 mm was required in order to avoid an underestimation of the temperature and considering the laser spot size was approximately 1.5 mm, large errors could be expected depending on the imager employed. In our case, errors of 20 °C were measured.

However, if we have adequate knowledge of the limitations of the imaging device, then a more realistic estimation of the temperature can be made by use of a computational model. A major part of the work presented here comprised of the

development of a suitable model. Central to this was the determination of the point spread function (PSF) of the imager. This describes mathematically how a point in object space is imaged and the objective of the computational model is to run this process in reverse, that is to infer the object distribution from knowledge of the PSF and the image distribution. The PSF was found by two independent techniques, whose results were in close agreement.

In order to assess the accuracy of the model another independent temperature measuring technique was required. A number were investigated, the most reliable being the picrosirius red staining technique which causes tissue to become optically inactive when viewed with polarised light if it is heated to a well defined threshold temperature. This temperature can readily be found and used to determine the accuracy of the model. It was found that the model could estimate tissue temperatures to an accuracy of 4 °C.

Table of Contents

i	Title Page
ii	Abstract
iv	Table of contents
x	List of tables and illustrations
1	Chapter 1: Introduction
	1.1: Laser applications in surgery and medicine
	(i): Development of the laser
2	(ii): A survey of laser applications in surgery and medicine
3	(a): Ablation of tissue
5	(b): Photo-coagulation of tissue
6	(c): Photo-chemical effects in tissue
	(iii): Lasers in cardiac surgery
8	1.2: Laser assisted vascular anastomosis (LAVA)
11	1.3: Infrared thermography - remote temperature measurement at the bond site
13	Chapter 2: Laser Assisted Vascular Anastomosis (LAVA)
	2.1: The need for LAVA
14	2.2: The need for accurate temperature measurement during LAVA
16	2.3: Published investigations of LAVA
17	(i): Type of laser / type of blood vessel

21	(ii): Type of bond / apposition of vessel edges
23	(iii): Applied energy density / temperature at bond site
24	2.4: Other methods of tissue bonding
26	2.5: Conclusion
28	Chapter 3: Thermal Imaging and the Pyro-electric Vidicon (PEV)
	3.1: Introduction
30	3.2: Basic Concepts of Thermal Radiation
33	3.3: Principles of Detection of Thermal Radiation
	(i): Thermal Detectors
34	(ii): Photon Detectors
35	3.4: The PEV
	(i): The pyro-electric effect
38	(ii): The development of the PEV
40	(iii): Operation of the PEV
45	3.5: The problems of temperature measurement with thermal imagers
	(i): Introduction
47	(ii): The emissivity problem
51	(iii): The spatial resolution problem
55	3.6: Literature review of temperature measurements
61	3.7: Other thermographic techniques in medicine
	(i): Vascular disorder investigations
	(ii): Assessment of inflammatory conditions

62	(iii): Assessment of pain and trauma
	(iv): Oncological investigations
	(v): Metabolic studies
63	Chapter 4: The Performance of the PEV
	4.1: Detector performance
	(i): Time constant
64	(ii): Responsivity
	(iii): Noise
65	(iv): Detectivity
66	4.2: Performance of the imaging system
68	(i): Spatial resolution
	(a): Modulation Transfer Function
70	(b): Spatial resolution in terms of minimum source widths
71	(c): Angular resolution
72	(d): Note on some quoted values for spatial resolution in literature relating to laser surgery
73	(ii): Temperature resolution
	(a): Noise equivalent temperature difference
	(b): Minimum resolvable temperature difference
74	4.3: Equipment
	(i): The argon ion laser
76	(ii): The PEV

	(iii): Visualising and measuring the temperature profiles
	(a): Monitor
78	(b): Oscilloscope
	(c): Recording the signals
81	4.4: Results
	(i): Spatial resolution
	(a): Subjective measurement
86	(b): Objective measurement (I): Variable slit
90	(c): Objective measurement (II): Circular aperture
94	(d): Correction factors
101	(e): 12.5 mm heat source
	(f): Angular resolution
103	(ii): Temperature resolution
104	(iii): Linearity of response
	(iv): Depth of field
109	(v): Curvature
115	Chapter 5: Temperature Measuring Techniques for the Corroboration of the Computer Model
	5.1: Introduction
117	5.2: Micro-thermocouples
121	5.3: Differential Scanning Calorimetry
	(i): Principles of the technique
122	(ii): Experimental set-up and results

126	5.4: Tissue staining with picrosirius red
	(i): Principles of the technique
130	(ii): Results
132	5.5: Conclusion
133	Chapter 6: Computer Modelling (I): Convolution and the Point Spread Function
	6.1: Introduction
134	6.2: Mathematical description
139	6.3: Application to the model
142	6.4: Determination of the PSF
	(i): Computational model approach
147	(ii): Edge spread function approach
154	6.5: Effect of the experimental set-up on the PSF
	(i): PSF as a function of magnification
157	(ii): PSF as a function of source temperature
160	(iii): Effect of temperature range
164	(iv): Effect of orientation of temperature step
	(v): Effect of aperture size
165	6.6: Conclusion
166	Chapter 7: Computer model (II): Deconvolution
	7.1: Deconvolving constant temperature sources
168	(i): Description of the computational models
	(a): The PSF model
170	(b): The equal area model

	(ii): Estimation of source width
175	(iii): Extrapolating the image down to room temperature
177	(iv): Results
	(a): The equal area model
	(b): The PSF model
182	7.2: Deconvolving a Gaussian temperature profile
193	7.3: Estimating the temperature of laser-irradiated tissue
	(i): Description of the experiment
195	(ii): Results
197	(iii): Conclusions
200	Chapter 8: Conclusions

List of Tables and Illustrations

Chapter 1

- 3** Table 1.1: Commonly used lasers
- 4** Table 1.2: Biological changes as a function of temperature
- 10** Table 1.3: Preliminary LAVA results

Chapter 2

- 18** Table 2.1: Summary of LAVA results
- 21** Table 2.2: Laser penetration depths in tissue
- 22** Fig. 2.1: Examples of anastomoses

Chapter 3

- 32** Fig. 3.1: Typical black body spectra for different source temperatures
- 42** Fig. 3.2: Schematic of PEV
- 43** Fig. 3.3: Target voltage-current characteristics for the PEV
- 47** Table 3.1: Estimations of the emissivity of biological tissue
- 52** Fig. 3.4: Temperature error as a function of source width
- 54** Fig. 3.5: Effect of source width smaller than resolution limit
- 57** Fig. 3.6: Effect of different resolution limits on the temperature measurement errors
- 58** Fig. 3.7: Effect of conduction on temperature profile

Chapter 4

- 67** Fig. 4.1: Detectivities of various imagers

69	Fig. 4.2: Modulation transfer functions
75	Fig. 4.3: Typical experimental set-up
77	Fig. 4.4: Monitor display
79	Fig. 4.5: Oscilloscope output
80	Fig. 4.6: Recording signals with an x-t recorder
82	Fig. 4.7: Proposed effect of increasing magnification
85	Fig. 4.8: Device for measurement of resolution
87	Fig. 4.9: Experimental set-up
88	Fig. 4.10: Spatial resolution (I)
89	Fig. 4.11: Spatial resolution (II)
91	Fig. 4.12: Spatial resolution (III)
92	Fig. 4.13: Spatial resolution (IV)
93	Fig. 4.14: Spatial resolution (V)
95	Fig. 4.15: Circular aperture compared with slit
97	Fig. 4.16: Thermostrips
98	Fig. 4.17: Correction factors for thermostrips
100	Fig. 4.18: Thermostrip emissivity
102	Fig. 4.19: 12.5 mm heat source
105	Fig. 4.20: Linearity of response
107	Fig. 4.21: Depth of field (I)
108	Fig. 4.22: Depth of field (II)
111	Fig. 4.23: Effect of curvature on measured temperatures (I)
113	Fig. 4.24: Effect of curvature on measured temperatures (II)

Chapter 5

- 119 Table 5.1: Repeatability of micro-thermocouple measurements
- 120 Fig. 5.1: Temperature measurements : thermocouple compared with
thermal imager
- 123 Fig. 5.2: Example of DSC analysis
- 125 Fig. 5.3: DSC:- Area under curve versus sample thickness
- 127 Fig. 5.4: DSC results
- 128 Fig. 5.5: Example of picrosirius red staining technique
- 131 Fig. 5.6: Stained tissue samples heated to (a) 64 °C, (b) 65 °C, (c)
66 °C, (d) 67 °C as viewed with polarised light

Chapter 6

- 136 Fig. 6.1: Visualisation of the generalised convolution equation
- 140 Fig. 6.2: Visualisation of the computational model
- 143 Fig. 6.3: Computer output for the prediction of image distribution
- 145 Fig. 6.4: Computational model prediction of effect of triangular PSF
- 146 Fig. 6.5: Computational model prediction of effect of Gaussian PSF
- 148 Fig. 6.6: Comparison of PSF and LSF
- 150 Fig. 6.7: ESF for magnification of 0.1
- 151 Fig. 6.8: ESF for magnification of 0.2
- 152 Fig. 6.9: Normalised ESF's for different magnifications
- 153 Fig. 6.10: Comparison of PSF's
- 156 Fig. 6.11: Comparison of normalised PSF's
- 159 Fig. 6.12: Gaussian Constant as a function of source temperature
- 160 Table 6.1: PSF as a function of source temperature

161 Fig. 6.13: Effect on ESF of varying temperature range

163 Fig. 6.14: Why the ESF's of Fig. 6.13 are different

Chapter 7

169 Fig. 7.1: Image distribution for analysis by computational model

172 Fig. 7.2: Comparison of PSF for 4 and 5 mm slit widths for different temperatures

173 Fig. 7.3: Experimental data used to determine source width

174 Table 7.1: Position corresponding to half maximum signal

Table 7.2: Computational model estimates of source width

176 Fig. 7.4: Example of extrapolation of image distribution below threshold temperature

177 Table 7.3: Temperature estimates of constant temperature sources by equal area model

178 Table 7.4: Temperature estimates of constant temperature sources by PSF model

179 Fig. 7.5: PSF computational model output for 2 mm source

180 Fig. 7.6: PSF computational model output for 4 mm source

181 Fig. 7.7: PSF computational model output for 6 mm source

184 Fig. 7.8: Example of convolved Gaussian source

185 Fig. 7.9: Comparison of errors for Gaussian and rectangular temperature profiles

187 Fig. 7.10: Computer output for estimation of temperature of Gaussian source using PSF model

188 Fig. 7.11: Computer output for estimation of temperature of Gaussian source using PSF subtraction model (I)

- 190** Fig. 7.12: Computer output for estimation of temperature of Gaussian source using PSF subtraction model (II)
- 191** Table 7.5: Temperature estimates of Gaussian sources using the PSF subtraction model
- 192** Fig. 7.13: Computer output for estimation of temperature of constant temperature source using PSF subtraction model
- 193** Table 7.6: Temperature estimates of constant temperature sources using the PSF subtraction model
- 196** Fig. 7.14: Stained tissue samples heated with laser energy to temperatures of (a) 44 °C, (b) 45 °C, (c) 46 °C, (d) 47 °C
- 197** Table 7.7: Temperature estimates of irradiated tissue samples using the PSF subtraction model - contrasted with the outcome of the picrosirius red staining technique
- 199** Fig. 7.15: Computer output for estimation of temperature of tissue irradiated by laser energy

Acknowledgements

My thanks go to the British Heart Foundation who funded this project. Also to my supervisors, Dr. D.V. Land at the Department of Physics and Astronomy, University of Glasgow and Prof. D.J. Wheatley at the Department of Cardiac Surgery, Glasgow Royal Infirmary.

In addition, thanks go to Dr. John Fenner, also at the Department of Cardiac Surgery for his help and encouragement and to Mr. John Morrison for technical assistance and the processing of the biological samples. Also to Dr. David Taggart, aided by Mr. Bill Dunn, for the initial surgical experiments. The biological samples were provided free by the Glasgow Abattoir Company Ltd.

CHAPTER 1:

INTRODUCTION

1.1: LASER APPLICATIONS IN SURGERY AND MEDICINE

1.1(i): Development of the laser

The principle of the stimulated emission of radiation was first described by Einstein in 1917 [1]. This involves the interaction of an excited atom with a photon whose energy corresponds to one possible transition energy in the excited atom. The result of this interaction is the emission of 2 photons of identical wavelength and polarisation, travelling in the same direction with the same phase.

This is the underlying principle of the laser (Light Amplification by the Stimulated Emission of Radiation) but the construction of the first successful laser did not come about until 1960. It was built by T. H. Maiman using a pink ruby rod as the lasing medium [2]. This was preceded by the construction of a maser, a similar device which emits microwaves rather than optical radiation, by C. H. Townes in the early 1950's [3].

Townes and A. H. Schawlow then went on to describe the principles of the optical laser or maser [4] which was subsequently built by Maiman. The laser quickly found applications in materials processing and communications and it is the basis for modern optical data processing and holography.

Lasers are classed according to the medium which is excited into a state that allows the stimulated emission of radiation. This medium can be gas, liquid or solid and some common examples are given in Table 1.1 [5].

1.1(ii): A survey of laser applications in surgery and medicine

In 1971, the first clinical use of the laser as a tissue welding device was reported by F. A. L'Esperance, who used an argon and a ruby laser to seal choroidal leaks which, otherwise, would have led to the destruction of the rods and cones and connecting nerves of the retina with the subsequent loss of central vision [6].

This was followed by an explosion of ideas relating to the potential applications of lasers in surgery and medicine, most of which never or have not yet moved beyond the experimental stage and into routine clinical application. These applications can generally be split into 3 categories [7]:

- (a): ablation of tissue; (b): photo coagulation of tissue;
- (c): photochemical effects in tissue

Table 1.1: Commonly used lasers

<u>Laser medium</u>	<u>Examples</u>	<u>Wavelength(s)</u>
solid	Ruby	692, 694 nm
	Neodymium:yttrium aluminium garnet (Nd:YAG)	1.06 μm
	Semi-conductor, e.g. Gallium arsenide (GaAs)	850-900 nm (temperature dependent)
	liquid	Dye, e.g. Rhodamin 6G
gas	Helium neon(HeNe)	633 nm
	Argon	9 discrete wavelengths between 454.5- 528.7 nm
	CO ₂	10.6 μm

1.1(ii)(a): Ablation of tissue

The first two categories involve the conversion of radiant energy into heat and the biological changes effected by the increase in temperature are summarised in Table 1.2 [8].

Table 1.2: Biological changes as a function of temperature

Temperature (°C)	Biological change
37 - 60	warming, welding
60 - 65	coagulation
65 - 90	protein denaturation
90 - 100	drying
> 100	vaporisation, carbonisation

When ablating tissue, the conversion of radiant energy to heat is both rapid and intense and it results in the vaporisation of tissue. The CO₂ laser is the most commonly used in the operating theatre for this purpose and its secondary cauterising effects are also useful. The Nd:YAG laser is also popular for this purpose. Its applications are increasing rapidly due to the ease of fibre optic delivery, The availability of high power when required and the use of contact probes for fine cutting and vaporising. Its versatility has led to a rapid growth in general surgery and ophthalmology.

1.1(ii)(b): Photo coagulation of tissue

The lasers' referred to above can also be used in a controlled manner to photo coagulate tissue, simply by reducing the power density or the time of application. (For numerous references to this work, see Chapter 2). This results in lower tissue temperatures and rather than vaporising the tissue, The laser energy brings about a coagulation of the tissue thought to be related to the denaturation and/or the dehydration of the tissue. The actual mechanism of tissue bonding will be dealt with in more detail in the next chapter.

Another popular laser in this category is the argon ion laser utilised by L'Esperance [6]. The argon lasers' primary use remains in ophthalmology as a retina photo coagulator but it is beginning to find widespread use in dermatology to photo coagulate pigmented lesions such as port wine stains and tattoos and intra-abdominally in endometriosis. Certain tissue pigments, principally melanin and haemoglobin, absorb the argon wavelengths very effectively and the light passes through the overlying skin without significant absorption and reaches the pigmented lesion to effect capillary desiccation and protein coagulation.

1.1(ii)(c): Photochemical effects in tissue

A third area of application of lasers in medicine is a non-thermal effect which works through the laser energy initiating a chemical reaction in the tissue. A particularly active area of research relating to this effect is Photo Dynamic Therapy (PDT) [9] which involves the administration of the drug haematoporphyrin derivative to patients suffering from inoperable cancer. After a few days, the drug is retained by the tumour(s) and when irradiated by light of around 630 nm wavelength, the drug is activated, producing a cytotoxic substance. This substance is relatively short-lived and, hence, nearby healthy tissue is spared. The necessity of using a laser with a definite optical wavelength is readily achieved by the use of a tuneable dye laser.

1.1(iii): Lasers in cardiac surgery

The laser application relevant to this project is Laser Assisted Vascular Anastomosis (LAVA), a technique which is introduced in the next section and described in detail in Chapter 2. It concerns the photo coagulation/welding of vascular tissue by means of a laser, with the aim of replacing the conventional suturing technique during by-pass surgery.

obstruction, with relative ease, though this method has thus far proven difficult to control and vessel walls are easily damaged in the process.

In addition to these investigations into the recanalisation of occluded blood vessels the laser has been used to ablate cardiac and arterial lesions [14] and it is likely that many more applications will be investigated in the future.

1.2: LASER ASSISTED VASCULAR ANASTOMOSIS (LAVA)

The LAVA technique has been widely investigated as a means of improving on the suturing technique currently used to bond by-pass grafts during open heart surgery. The saphenous vein or internal mammary artery is grafted from the aorta to the occluded coronary artery such that the blood supply by-passes the occlusion. It requires a high degree of surgical skill in order to achieve a lasting bond and to minimise the length of time that the patient has to be anaesthetised for.

K. K. Jain and W. Gorisch [15] first proposed a new method of tissue bonding in 1979, utilising laser energy to effect the anastomosis and since then many other groups have investigated the lasers' potential as a tissue bonding tool. It has been proposed that the laser induced bond has many advantages over that produced by sutures including improved sterility and long term patency rates, increased precision and shorter times to perform

the operation. These investigations are comprehensively reviewed in Chapter 2.

This project follows on from preliminary investigations carried out at the Department of Cardiac Surgery, Glasgow Royal Infirmary on the carotid artery of the New Zealand white rabbit. This animal model was chosen because of its similar histology to the human coronary artery. It was approximately 1 mm in diameter with a wall thickness of 0.1-0.2 mm. A longitudinal incision was made in the exposed artery and laser energy was applied to produce a seal. An argon ion laser was used, with an approximate beam diameter of 1.5 mm, and the energy was delivered by an optical fibre which was held in an articulated arm positioned over the artery.

The results have not yet been published [16] but Table 1.3 summarises the results.

The results should not be taken to mean that the technique is unsuccessful. The early results, in Group A (laser only) looked promising but no attempt was made to optimise the laser output parameters such as applied power density. Also, it is to be expected that some of the failures were related to inexperience with the technique.

Table 1.3: Preliminary LAVA results

group	no.	technical failures	early	examination		patency rate
			<24hrs	4-14 days	thrombosed	
A	18	0	5(28%)	6	7	33%
B	8	0	4(50%)	0	4	0%
C	5	1	3(60%)	1	0	20%
D	45	4	2(4%)	13	26	29%

Group A: laser only; Group B: chromophore applied before laser

Group C: chromophore, laser, collagen patch

Group D: chromophore, laser, cyano-acrylate glue

In Group B, a chromophore (1% fuchsin in alcohol) was applied before the laser irradiation. This is a dye which absorbs the laser wavelengths and although the laser output power was reduced by a factor of 3, there was no way to tell whether or not this was close enough to an optimal output.

The collagen patch used in Group C was not extensively investigated as it was very awkward to use and it gave poor results.

The cyano-acrylate glue, used in Group D, had the principal advantage of dramatically reducing the early failure rate but not of improving the overall patency rate. In addition to the 45 experiments with

the laser and the glue, the glue was applied to 10 arteries in 5 animals to test its thrombogenic effect. No effect was found in any of the arteries.

In summary, then, the initial investigations seemed to show a poor patency rate ($\approx 30\%$) and widespread tissue disruption and cellular necrosis were found histologically in all groups. However, other investigations by different research groups have reported much greater success and, therefore, the technique should not be abandoned on the basis of these results. At this stage, though, it was clear that a number of issues had to be resolved before proceeding further with the animal experimentation. To address these issues, a number of groups have been attempting to measure the tissue temperatures at the bond site. This is the subject of the next section.

1.3: INFRARED THERMOGRAPHY -Remote Temperature measurement at the bond site

Infrared thermography has wide-ranging clinical applications and has already been utilised in cardiac surgery to visualise coronary artery blood flow and assess myocardial perfusion during aorta to coronary artery bypass surgery [17]. However, this only involves a qualitative comparison of areas at different temperatures and for this purpose the thermal imager can be relied upon. Quantitative temperature measurements, however, present

us with problems which have to be carefully addressed if we are to avoid making highly inaccurate temperature measurements.

Surmounting these problems constitutes the bulk of the work carried out for this thesis and they are described in detail in Chapters 3 and 4. A computer model is developed in Chapters 6 and 7 which allows an analysis of the temperature distributions obtained during LAVA. This is preceded in Chapter 5 by an analysis of other temperature measuring techniques which may be used to corroborate the model. These techniques are only useful if the biological sample is available for microscopic analysis after irradiation by the laser and hence it is necessary to develop a computer model which allows temperature measurement without the subsequent destruction of the tissue.

It is hoped that reliable temperature measurements will allow an understanding of the bonding mechanism to be developed which in turn should help to give an insight into the possible causes of the inconsistencies in the results. In addition to this, correct temperature measurements will allow the process to be controlled in a far more rigorous manner.

CHAPTER 2:

LASER-ASSISTED VASCULAR ANASTOMOSES (LAVA)

2.1: THE NEED FOR LAVA

As outlined in Chapter 1, laser-induced tissue bonding was first introduced in 1979 by Jain and Gorisch in the investigation of the repair of small blood vessels. Up until this time, the only accepted method of vessel repair was by the application of stay sutures around the vessel wall. Although laser-induced tissue bonding and other alternative techniques have been widely investigated, the suturing technique remains standard clinical practice.

The original paper by Jain and Gorisch related to blood vessels up to 1mm diameter as these were particularly difficult and sometimes impossible to repair successfully by the suturing technique but many authors since have investigated the repair of larger vessels with varying degrees of success (see section 2.3). It has also been pointed out that there is no possibility of

foreign body reaction in the tissue as the laser energy is sterile and non-tactile and many authors have reported the preservation of the mechanical properties, decreased intimal hyperplasia and the unrestricted enlargement of growing vessels subsequent to the laser-induced bond.

2.2: THE NEED FOR ACCURATE TEMPERATURE

MEASUREMENT DURING LAVA

The overwhelming problem that has prevented the clinical application of LAVA has been the lack of consistency in the results. Many authors have suggested that this inconsistency could be eliminated if the bonding mechanism was understood and the bonding process properly controlled. The laser-irradiated bond sites have been examined histologically in an attempt to elucidate this mechanism.

Serure et al. [18] concluded that the bond resulted from collagen denaturation in the media and adventitia of the vessel with subsequent fibrin polymerisation. Schober et al. [19] found through histological analyses that a homogenising change had taken place in the collagen with interdigitation of individual fibrils and suggested this to be the structural basis for the bond.

This prompted researchers to attempt to monitor tissue temperatures during laser-irradiation in order to corroborate histological findings and to control the temperature-dependant events taking place at the bond site.

Badeau et al. [20] reported that welds took place between 80-120°C and Kopchok et al. [21] similarly reported temperatures in excess of 100°C, suggesting that the bond was formed by a coagulum of denatured collagen and cells.

The findings noted above relate to bonding with the CO₂ laser. However, as Kopchok et al. pointed out, although this coagulum was adequate to withstand low pressures such as those found in micro-vessels and veins, it was inadequate to withstand systemic arterial pressures. Therefore, they attempted laser bonded arteriovenous fistulas with the argon laser which has a greater penetration depth in tissue, and found that successful bonds occurred in the estimated range of 43-48°C. This temperature range would not be adequate to denature the collagen and they suggested that the bond was established by the formation of cross-linkages in annealing collagen.

In addition to the role played by the denaturation of tissue in the bonding mechanism, a further factor has been suggested by Fenner et al. [22]. Most authors have concluded that the bonding comes about through a thermal effect as opposed to a photo-chemical effect and Fenner et al. simulated this thermal effect of the laser using a heat lamp to bond tissue under dry and wet conditions. They found that the bonds created in dehydrated tissue were far stronger than the bonds created in the hydrated specimens. They also showed that the strength of the bond was temperature

dependent with a disproportionate increase above the denaturation temperature of the tissue. This temperature has been estimated as 62 °C.

From the above, although the bonding mechanism is not fully understood, it is apparent that the denaturation and the dehydration of the tissue play a significant role. As both of these factors are highly temperature dependent, the need for the accurate monitoring and controlling of temperatures during LAVA is obvious. However, as will be shown in later chapters, the apparent temperatures will be underestimated to varying degrees if full account is not taken of the resolution characteristics of the imaging device. This point applies to the temperature estimates of Badeau et al. and Kopchok et al. and they are therefore unreliable.

2.3: PUBLISHED INVESTIGATIONS OF LAVA

Since the first report of the successful bonding of blood vessels by laser-induced irradiation, many investigators have published the results of their work on this technique. Their conclusions were largely optimistic throughout the 1980's with most authors suggesting that it was a matter of time before the laser technique replaced the suturing technique in a wide variety of clinical applications.

To date there have been two reports of successful human LAVA trials [23, 24], both of which chose low risk peripheral vessels in patients with

chronic renal failure to perform their evaluation. On the basis of these results Okada predicted that the same technique would be used for aortcoronary bypasses in the near future.

However, at the other extreme, in two more recent reports by Gennaro et al. [25] and Lawrence et al. [26], it was concluded that there was no evidence as yet to suggest that lasers are likely to replace the conventional suturing technique in the near future. In fact, Lawrence showed that absorbable sutures (see Section 2.4) exhibited most of the supposed advantages of LAVA without the concomitant expense.

It is impossible to compare the findings of the many authors work directly as their are so many variables involved, the most important of which are as follows:

- (i) Type of laser / type of blood vessel
- (ii) Type of bond / apposition of vessel edges
- (iii) Applied energy density / temperature at bond site

2.3 (i): Type of laser / type of blood vessel

Table 2.1 gives a summary of the results from various authors. The groups have been split according to laser type and vessel diameter. The vast majority of research has centred around the CO₂ laser, the argon ion laser and the Nd:YAG laser although other lasers have been employed, such as the dye and the excimer lasers. Vessels with diameters of less than 3 mm have

been defined as small vessels and diameters of 3 mm or greater as large vessels.

TABLE 2.1: SUMMARY OF LAVA RESULTS

(L) = LASED SPECIMEN
(S) = SUTURED SPECIMEN

(i) CO₂ SMALL

<u>AUTHOR &YEAR</u>	<u>TYPE</u>	<u>NO.</u>	<u>BOND TIME</u>	<u>SACRI -FICED</u>	<u>PATENCY</u>
Serure'84 [18]	1mm;rat	(L)32	faster	9wks	100%
	femoral	(S)32	''	''	100%
Frazier'84 [27]	1.6mm;swine	(L)9	20mins	13wks	100%
	femoral	(S)5	30mins	''	100%
J.V.White '85[28]	1.4mm;rabbit carotid	(L)16		6wks	82%
Nakata'89 [29]	2mm;rabbit carotid	(L)80	5mins	1yr	98%
		(S)80	11mins	''	79%
		(L)40			95%
Gennaro'91 [25]	1.2mm;rabbit jugular	(L)15	12.9mins	30 days	87%
		(S)10	19.1mins	''	90%(*)
		(S)5	12.5mins	''	20%**)

(*) = interrupted sutures
(**) = continuous sutures

(ii) CO₂ LARGE

<u>AUTHOR & YEAR</u>	<u>TYPE</u>	<u>NO.</u>	<u>BOND TIME</u>	<u>SACRI -FICED</u>	<u>PATENCY</u>
Ashworth '87 [30]	mongrel carotid	(L)12 (S)12	7mins 25mins	6wks ''	100% 92%

R.A. White '86 [31] 6mm; canine arteries thick-walled, high pressure which seals could not withstand

(iii) Nd:YAG SMALL

<u>AUTHOR & YEAR</u>	<u>TYPE</u>	<u>NO.</u>	<u>BOND TIME</u>	<u>SACRI -FICED</u>	<u>PATENCY</u>
Schober '86 [19]	rat carotid			11wks	100%
Nijjima '87 [32]	rat carotid	61		30days	92%

(iv) Nd:YAG LARGE

R.A. White '86: initially successful but majority failed within 20-40 mins [31]

(v) ARGON LARGE

<u>AUTHOR & YEAR</u>	<u>TYPE</u>	<u>NO.</u>	<u>BOND TIME</u>	<u>SACRI -FICED</u>	<u>PATENCY</u>
R.A. White '86 [31]					4-6 wks with less foreign body reaction
Kuroyanagi '91 [33]	6mm; mongrel femoral	(L)12 (S)8	13.4mins 27.6mins	1yr ''	100% 100%
Lawrence '91 [26]	mongrel femoral & carotid	(L)104 (S)28 (S)32	10.45mins 5.87mins ''		59% 100% 100% (*)

(*) = absorbable sutures

The first reports of LAVA concerned the application of CO₂ or Nd:YAG laser energy to micro vascular anastomoses and they showed patency rates comparable with conventional suturing techniques with the advantages of being faster and showing less foreign body reaction. However, when applied to larger vessels, Kopchok et al. [21] found that, although all 3 lasers were effective for venotomies, only the argon laser provided satisfactory bonds when arteriotomies, arteriovenous fistulas and artery to vein anastomoses in reverse vein by-pass were attempted. Similarly, R.A. White et al. [31] reported, for large vessel arteriotomies, that the CO₂ laser did not produce seals that could withstand arterial pressures and that the Nd:YAG laser was initially successful, but the majority failed within 20-40 mins. The argon laser, however, uniformly sealed 5 vessels which healed rapidly within 4-6 weeks, although stay sutures were required every 5 mm in order to appose the vessel edges, otherwise the LAVA were largely unsuccessful because of their low initial tensile strength. Additional sutures were sometimes required to close sites not fully sealed by the laser energy. Kopchok et al. suggested that this was due to a difference in the bonding mechanism between the CO₂ / Nd:YAG and the argon laser.

The difference between the lasers lies principally in their penetration depths in tissue.

Table 2.2: Laser penetration depths in tissue

<u>Laser</u>	<u>Penetration depth</u>
CO ₂	10 μ m
Argon	0.6 mm
Nd:YAG	2 mm

Table 2.2 shows clearly why the CO₂ lasers' success has been primarily with microvasculature as the laser energy could only penetrate the superficial layer of the blood vessel, whereas the argon laser appears to be well suited for larger vessels. However, this simplistic approach does not explain the reported success of the Nd:YAG laser for micro vascular anastomoses, nor the CO₂ laser for larger vessels. Further to this a study by Lawrence et al. [26] produced a very poor patency rate for the argon laser applied to larger vessels. These results suggest that although the type of laser chosen undoubtedly has an effect, there are many other factors producing inconsistencies in the results.

2.3 (ii): Type of bond / apposition of vessel edges

There have been 4 principal types of anastomoses attempted with LAVA (Fig. 2.1): (i) the repair of a longitudinal incision, (ii) end-to-end, (iii) side-to-side and (iv) side-to-end. Fig. 2.1(iv) is an example of the anastomosis required during heart by-pass surgery.

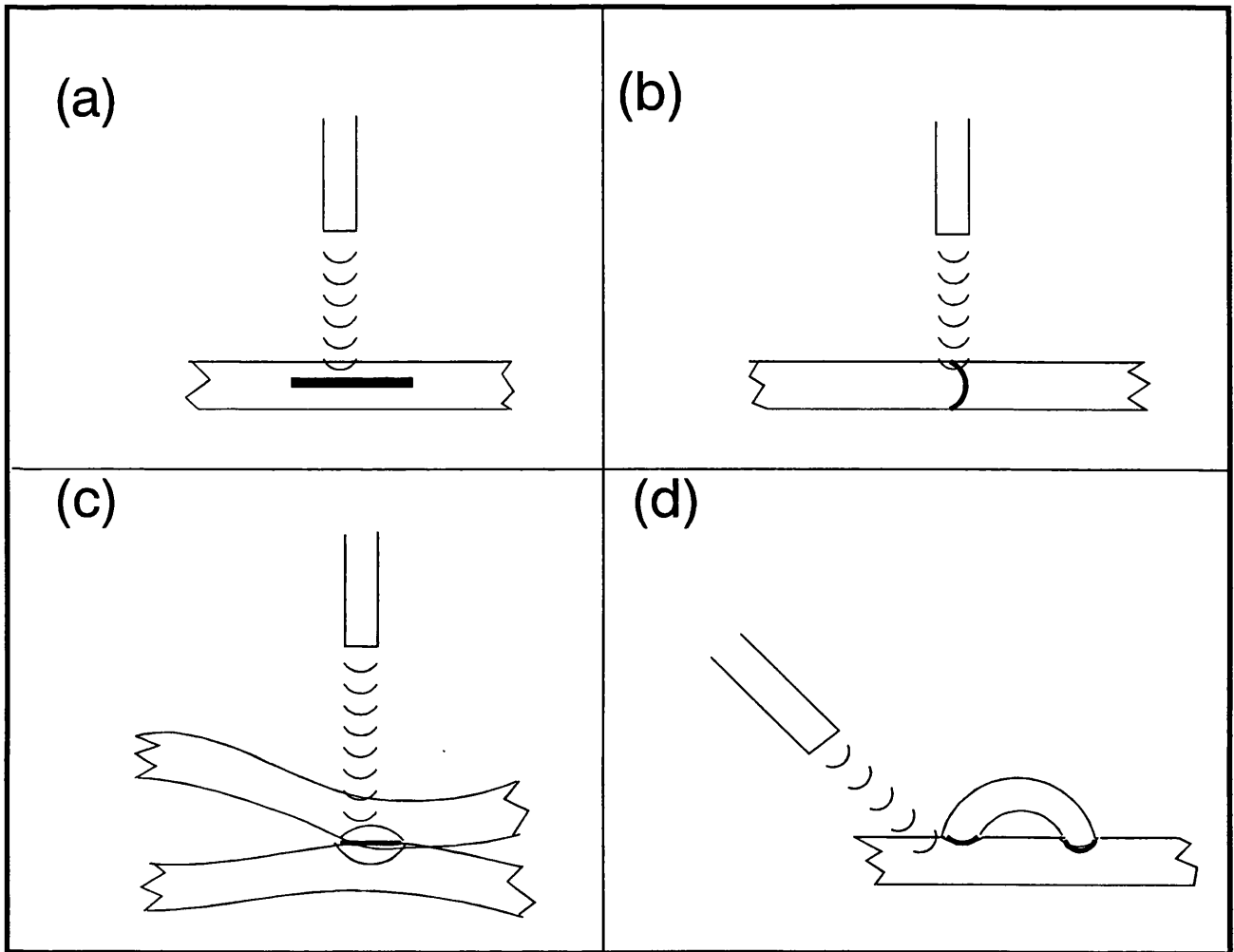


Fig. 2.1 Examples of anastomoses

The longitudinal incision appears to be technically less demanding but this is not borne out by the results which show a similar degree of success for all 4 kinds. However, it should be noted that 3 or 4 additional sutures were required to appose the vessel edges and in a number of cases, additional sutures were required to close the bond [18, 25, 26, 29, 30].

The problem of apposing the vessel edges has been pointed out by many authors', in particular Fenner et al. pointed out that visible air gaps were trapped between the bonded faces and although this experiment did not involve a laser, the same principle would apply to laser bonded tissue.

Lawrence et al. went further and suggested that the difficulty of apposition and temperature monitoring combined with the longer time for LAVA reported in their paper and the much greater cost should rule out the clinical application of LAVA for the moment. They also showed that absorbable sutures could provide the proposed advantages of LAVA without the reported disadvantages. However, this report should not be given more weight than the many others that have reported considerably more success.

2.3(iii): Applied energy density / temperature at bond site

Most publications on LAVA state the applied energy density and the time taken for the bond, allowing a calculation of the average power density. However, although the power density will have a great contribution

efficacy of the bond, the average power density is not a very helpful parameter. This is because the laser energy is applied in a non-uniform manner, the speed that the laser traverses the vessel being controlled by the operator. Under these conditions, if the power density fluctuates to a great enough extent, then it would be more likely that the bond would fail, either too great a power density or too low a power density at a particular point.

This could be overcome in a laboratory situation using a motorised device which moves the laser head uniformly over the tissue but it would prove impracticable in a clinical situation as "straight-line" bonds are rarely encountered.

2.4: OTHER METHODS OF TISSUE BONDING

Alternative methods of vascular anastomoses have been the subject of investigation for decades, largely as a result of the need to re-establish blood flow as quickly as possible during surgical procedures and also to overcome the difficulty of suturing small blood vessels. Androsov [34], in 1956, reported the development of a prosthesis for connecting and mechanically suturing blood vessels with tantalum wire clips, but although the technique was far less time consuming than the conventional suturing technique and produced favourable results, it never achieved widespread clinical application.

During the 1950's plastic materials were developed which were well tolerated by and adhered to animal tissue. This led to Nathan et al. [35] attempting to close arterial incisions with a rapidly polymerising adhesive. However, their inflexibility and tendency to produce tissue reaction remain significant drawbacks to date.

High-frequency alternating currents have been used since the start of the century for the purposes of hemostasis by causing the formation of a limited, heat-formed adherent coagulum. Sigel et al. [36], in 1962, attempted to use this method in a more controlled fashion in order to seal blood vessels whilst maintaining lumen patency and continuity. This method, although successful in some aspects, e.g. minimal tissue reaction, speed of closure, etc., failed to provide the necessary tensile strength required to withstand arterial pressures.

Absorbable sutures were introduced experimentally in the 1980's. The first kinds tried were found to be too stiff for general use. However, Steen et al. [37] found in a comparison of a more flexible material (Polydioxanone sutures) with the widely used polypropylene (Prolene) sutures, that the macroscopic findings, histological examination and the calculated blood flow pointed to a far more pronounced inflammatory tissue reaction with the Prolene sutures. This study was followed by Stillman et al. [38] who found that adhesion formation, fibrosis and foreign body reaction were common in

the non-absorbable groups and negligible in the absorbable groups and these results were emulated by Chiu et al. [39]. The previous 3 reports all relate to growing blood vessels and they all confirm that the growth of the blood vessels was relatively unimpaired with the use of absorbable sutures.

In a more recent study, Lawrence et al. [26] compared absorbable sutures, non-absorbable sutures and LAVA. They found the absorbable sutures to yield marginally more favourable results than the non-absorbable sutures but found both kinds of suture to give far better results than LAVA. Contrary to numerous other reports, they found that the suturing techniques took approximately half the time to perform as LAVA. Allied to the fact that LAVA was far more expensive than the suturing technique, they concluded that this will remain the conventional clinical choice for the foreseeable future.

2.5: CONCLUSION

LAVA has been widely investigated throughout the 1980's as a possible replacement for the standard suturing technique. The optimism of the early researchers has slowly been replaced by a belief that the problems involved are too great to provide a method of anastomoses as reliable as suturing. These problems include controlling the applied energy, measuring the temperature at the bond site and apposing the vessel edges. However,

although the inconsistent results have prevented the clinical application of the technique to high risk arteries, there have been 2 reports of successful human LAVA trials on low risk arteries. It remains to be seen whether these trials will be extended to more complex surgical procedures.

CHAPTER 3:

THERMAL IMAGING AND THE PYRO-ELECTRIC VIDICON

(P.E.V.)

3.1: INTRODUCTION

The need for accurate temperature measurement during LAVA was outlined in section 2.2. Various research groups have employed thermal imagers for this purpose. This seems to be the only feasible approach as a non-tactile method is required, otherwise the temperature pattern being measured will be altered, both by changing the heat dissipation and the laser absorption characteristics of the tissue volume.

Other methods of measuring tissue temperature include the use of thermocouples, liquid crystal thermography, microwave thermography and the mercury-in-glass thermometer, which is obviously not appropriate for this

application. The thermocouple has, in fact, been used as a tissue temperature measuring probe, but experiments utilising a micro-thermocouple described in Chapter 5 show this to be far from reliable. Liquid crystal thermography could not be considered because the crystals absorbed the laser energy before it could reach the tissue and, in practice, it would be a very clumsy method to attempt with small arteries. This also applies to microwave thermography which, in any case, measures tissue temperatures with a spatial resolution of the order of centimetres.

Infrared thermography surmounts these problems, though it is not without its own. In particular, the spatial resolution characteristics of the imager can lead to the underestimation of the temperature when imaging small heat radiation sources. There are two main classes of thermal imagers, viz. photon detectors and thermal detectors and their different modes of operation are described in Section 3.3. The photon detector minimises, but does not overcome, the resolution problem referred to above. However, photon detector imagers are very expensive and require cooling to liquid nitrogen temperatures. The only thermal detector currently utilised as a thermal imager is the P.E.V. which is cheaper, fully TV-compatible and is operated at room temperature. Although its spatial resolution characteristics are inferior to most photon detectors, used in conjunction with a computer model, it can yield reliable temperature measurements for LAVA.

3.2: BASIC CONCEPTS OF THERMAL RADIATION

Infrared radiation was discovered in 1800 by William Herschel whilst studying the refraction of visible light through a prism. He measured a temperature increase due to radiation beyond the visible red and demonstrated that this radiation obeyed the laws of reflection and refraction. Since this discovery scientific effort has produced infrared detectors of ever increasing sensitivity and resolving power and thermal imagers now have wide-ranging civil, industrial, military, medical and scientific applications.

All objects emit thermal radiation with a wavelength distribution and a power which is solely dependent on the temperature, T , and the emissivity, ϵ , of the object. This relationship is expressed as

$$W = \epsilon \sigma T^4 \text{ ----- (3.1)}$$

where W is the radiant emittance or power per unit area (W m^{-2}) and σ is a universal physical constant called the Stefan-Boltzmann constant and is equal to $5.67 \times 10^{-8} \text{ W m}^{-2} \text{ K}^{-4}$. It was deduced in the 19th century by Josef Stefan on the basis of experimental measurements by John Tyndall and was later derived by Ludwig Boltzmann from theoretical considerations. From this relationship a body's temperature can be deduced from knowledge of its

emissivity and its radiant emittance. This principle forms the basis of thermal imaging.

A black body is defined as an object of emissivity equal to one. That is, it absorbs all incident radiation and conversely, by Kirchhoffs law, it emits the maximum theoretically possible energy for a given temperature. The law describing this behaviour was derived by Max Planck in 1901 and is given by

$$W_{\lambda}d\lambda = \frac{8\pi hc}{\lambda^5} \left[\exp\left\{\frac{hc}{\lambda kT}\right\} - 1 \right]^{-1} d\lambda \text{----- (3.1)}$$

where $W_{\lambda}d\lambda$ is the radiative power, h is the Planck constant equal to 6.63×10^{-34} J s, c is the speed of light equal to 3×10^8 m s⁻¹, λ is the wavelength in m and k is the Boltzmann constant equal to 1.38×10^{-23} K J⁻¹. The infrared spectrum for bodies at various temperatures is shown in Fig. 3.1.

Wien had given an incomplete form of this law in 1893, but from this he was able to derive the correct displacement law:

$$\lambda_m = \frac{2,898}{T} \text{----- (3.3)}$$

where λ_m is the wavelength of the most strongly emitted radiation.

Atmospheric absorption by water vapour and carbon dioxide molecules largely restricts the use of infrared detection to two windows at 3-5 μ m and 8-13 μ m. However, the surface temperature of the human body is approximately 307

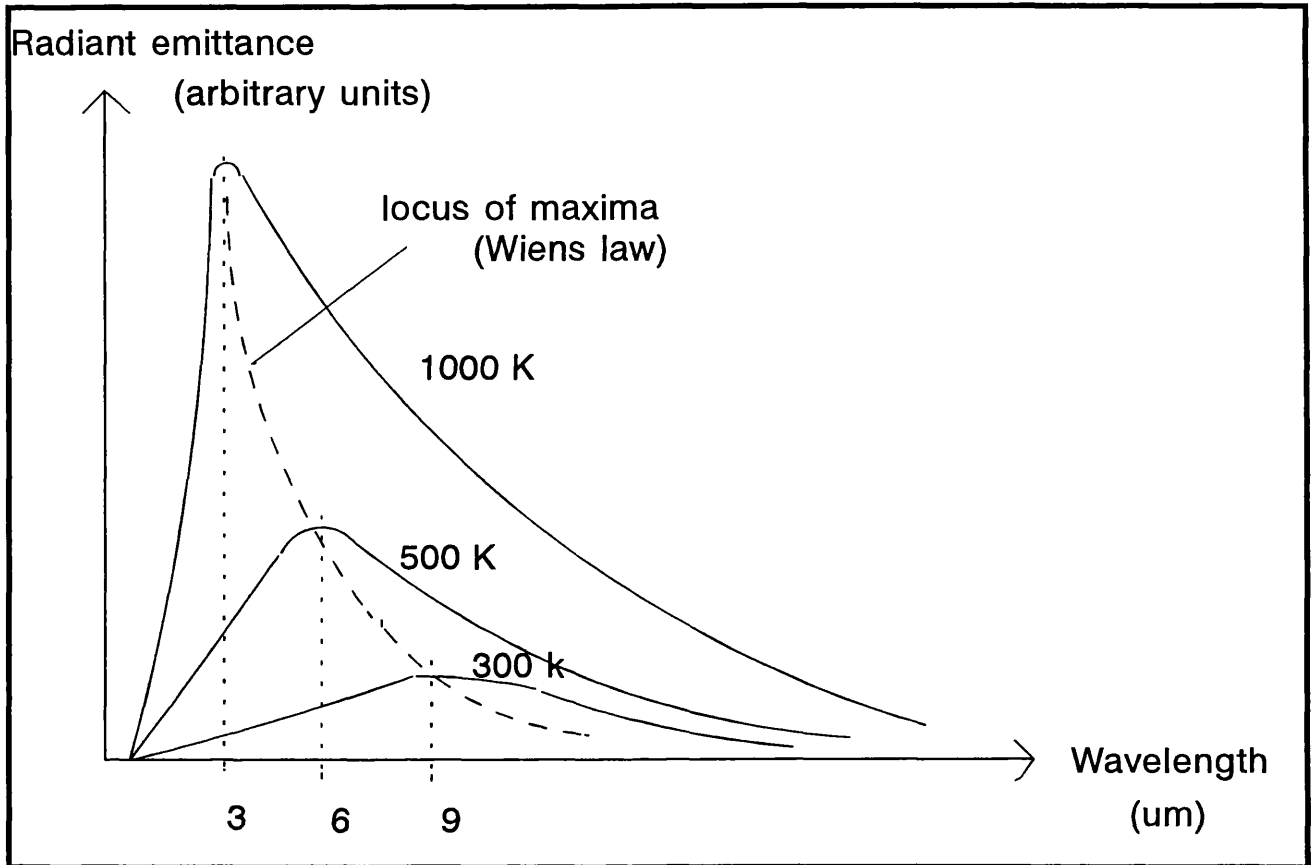


Fig. 3.1: Typical black-body spectra for different source temperatures

K and by Wiens displacement law, this gives $\lambda_m = 9.4 \mu\text{m}$ which is ideal for imaging in the infrared.

3.3: PRINCIPALS OF DETECTION OF THERMAL RADIATION

Thermal radiation can be detected and measured by the conversion of electromagnetic energy to an electrical signal. In practice, this can be achieved in two different ways, differentiated by their different methods of transduction.

3.3(i): Thermal detectors

The detecting element in thermal detectors is responsive to temperature changes induced by the incident radiation. Various effects are utilised to achieve this. These include the bolometric, thermovoltaic and pyroelectric effects.

The bolometer consists of two semi-conductor or metal strips connected to adjacent arms of a Wheatstone bridge. One strip is irradiated while the other is shielded and the infrared radiation causes a rise in temperature of the exposed strip which alters its conductivity. This imbalance is detected by an electronic circuit which enables the radiant energy to be measured.

The thermovoltaic effect is the production of a voltage across the junction of two dissimilar materials when heated. Thermocouples utilise this principle. Both ends of the two materials are welded together with one end at a reference temperature (normally ice temperature) and the other end exposed to the

temperature to be measured. The voltage generated is then measured by a suitable millivoltmeter. A more sensitive device is the thermopile which is basically a series of thermocouples in one responsive element.

Both of these thermal detectors have less sensitivity and longer time constants than photon detectors and neither are currently employed to image thermal radiation. The only thermal detector in use as an imager is the pyroelectric detector. A detailed description of this class of detector is deferred until Section 3.4, when the pyro-electric vidicon is described.

3.3(ii): Photon detectors

The detecting element in photon detectors is responsive to the number of incident photons in the incident radiation. They are semi-conductor devices, the majority of which utilise either the photoconductive or the photovoltaic effect.

In the case of photoconductive detectors, a change in the number of absorbed incident photons produces a change in the number of free charge carriers which, in turn, alters the conductivity of the device. This change in conductivity is detected, amplified and processed by the associated electronic circuitry. In the photovoltaic effect, the irradiation produces an e.m.f. at the junction of two different layers of semi-conductor material, which can then be processed in a similar manner to photoconductive detectors.

Photovoltaic detectors tend to be preferred as a bias current is not necessary. The bias current leads to high power dissipation in photoconductive detectors which can cause self-heating problems, although they have the advantage of ease of coupling to low-noise preamplifiers.

The most frequently used detecting materials in medical imaging are indium antimonide (InSb) and cadmium mercury telluride (CdHgTe) often abbreviated as CMT. Lead telluride (PbTe) is also common. They have a number of advantages of the P.E.V., principally, greater sensitivity and spatial resolution and a shorter time constant. These concepts will be dealt with in greater detail in the following chapter. The principal disadvantage of photon detectors is that cryogenic cooling is required to lower the detector noise enough. The detector is cooled to -196°C with liquid nitrogen.

3.4: THE P.E.V.

3.4(i): The pyroelectric effect

All crystals can be classified into 32 groups depending on their rotational symmetry [40]. 11 of these groups possess a centre of symmetry and are highly isotropic. Of the remaining 21 groups, 20 are piezoelectric, i.e. they exhibit electrical polarisation when subjected to an applied stress. They do not possess a centre of symmetry, are generally anisotropic but exhibit vectorial properties along one or more axes.

10 of the 20 piezoelectric crystals possess a unique polar axis, along which they are spontaneously polarised. In general this polarisation is neutralised through external or internal conductivity. However, the magnitude is temperature dependent and when the temperature is altered, electrical charges can be detected on the crystal faces perpendicular to their polar axis. This is the pyroelectric effect and when the crystal is subject to a temperature change (e.g. through infrared irradiation), it behaves like a capacitor which can then be discharged and the charge measured through an external load.

The mathematical description of the process is as follows [41]:

The bound surface charge, q , is given by

$$q = A P \text{ ----- (3.4)}$$

where A is the area of the crystal face and $P = \chi E + P_S$ is the total polarisation, χ is the electric susceptibility, E is the electric field inside the crystal (principally, the biasing field) and P_S is the spontaneous polarisation of the crystal.

The current, i , flowing from the crystal is then

$$i = A \frac{dP}{dt} = A \frac{d}{dt} (\chi E + P_S) \text{ ----- (3.5)}$$

If E is maintained constant and χ and P_S are functions solely of temperature, then

$$i = A \left(E \frac{\delta \chi}{\delta T} + \frac{\delta P_s}{\delta T} \right) \frac{dT}{dt} = A p \frac{dT}{dt} \text{ ----- (3.6)}$$

where p is the pyroelectric coefficient. Therefore the current is proportional to the rate of change of temperature.

A vast number of different pyroelectric materials exist but investigators have chosen materials which were ferroelectric since their spontaneous polarisation and rate of change of polarisation was high, thus yielding a large pyroelectric current. The dipole moments of ferroelectric crystals are readily aligned in the same direction, thus the pyroelectric effect is a maximum. This process is referred to as poling and is achieved by the application of a suitable d.c. electric field.

Ferroelectric materials which have been widely investigated include triglycine sulphate (TGS), deuterated TGS (DTGS), triglycine fluoroberyllate (TGFB), lead zirconate titanate (PZT) and barium titanate (BT) [41, 42, 43, 44, 45, 46]. The DTGS crystal has been most effective to date and is used in the 80 Series P.E.V. It has a high pyroelectric coefficient, low relative permittivity and is readily grown from water solution into large crystals that are readily thinned into large plates normal to the polar axis [47, 48].

3.4(ii): The development of the P.E.V.

The name pyroelectricity was introduced by Brewster in 1824 to describe the temperature dependence of polarisation in certain crystals [85]. However, until 1955, any measurements of the effect utilised electrometers which are not very sensitive. Chynoweth [45], in 1955, was the first to measure the effect, by its discharge through an external circuit. He subjected single crystals of barium titanate (BT) to small changes of temperature by illumination from flashlights and showed the technique to be a sensitive and non-destructive method for studying the state of polarization of a crystal.

In 1962 Cooper [44] developed a fast response pyroelectric thermal detector, again from a crystal of BT, and suggested its use for the measurement of large, short duration radiation fluxes, e.g. to give total radiation energy loss in pulsed gas discharges as used in controlled thermonuclear research.

The first thermal imagers became commercially available soon afterwards [46, 48, 49]. In these systems, the image was mechanically scanned point by point across a single detector, which was either a cooled photoconductor or a pyroelectric bolometer. They suffered from a poor sensitivity as only a small part of the imaged radiation was collected at any given time. This was not, in fact, a new technique as pioneering work had been done at British Air Defence

in the 1930's to detect hot aircraft engines but the results were not published [50].

The first suggestion that a pyroelectric material might be used in a camera tube was made by Hadni in 1965 and adopted by LeCarvenec in 1969 [51]. Here the pyroelectric target was used as a temperature-sensitive dielectric in the region of the Curie temperature and when the target temperature is changed, a voltage is produced because of the change in relative permittivity. However, this suffers from the disadvantages of the occurrence of the random switching of electric domains around the Curie temperature and of maintaining this temperature uniformly over the target area [52].

The use of a thin slice of pyroelectric material as a target in a conventional vidicon tube was first investigated by Holeman et al. and Putley et al. [53, 54] in the early 1970's. Since then improvements have been made in the sensitivity and the modulation transfer function (MTF). TGS and DTGS have been the most widely investigated materials and produce a signal current of 5 and 12 nA respectively at a target temperature of 30 °C, a target thickness of 14 µm, a chopping frequency of 25 Hz and an irradiance of 20 W m⁻². For this reason DTGS has been the preferred target material. The thermal diffusivity has been the main factor affecting the spatial resolution (usually described by the MTF). Steps taken to improve this have included the reticulation of the target to limit heat spread over the frame period [55]. Although this method provides

considerable improvement, it is costly to implement and therefore only appropriate for specific applications [56].

Other advances include the reduction of image noise and the improvement in image uniformity and with the addition of image analyses, the overall system meets the requirements of many medical thermographic applications relatively inexpensively.

3.4(iii): Operation of the P.E.V.

The 80 Series P.E.V. is essentially a conventional vidicon with a few modifications. A vidicon is a generic term for any TV camera tube in which the same target material serves as the radiation sensor, the charge storage device and the signal output electrode which is scanned by a beam of low velocity electrons. They are described in more detail in Ref. [57]. The P.E.V. differs from the conventional vidicon in three fundamental ways:

1. The standard vidicons light-sensitive photo-conductive target is replaced by a thin slice of DTGS.
2. The glass faceplate and lens is replaced by a germanium faceplate and lens on the P.E.V., allowing maximum transmission in the 8-12 μm spectral band.

3. Negative voltages have to be read from the target material and as it cannot be discharged by the negatively charged scanning electron beam, a positive pedestal current is required (described in more detail below).

The basic structure of a P.E.V. is outlined in Fig. 3.2. The purpose of the chopper is to modulate the incoming radiation as the pyroelectric target does not respond when subject to constant temperatures. The chopper blade interrupts the incident radiation in synchronisation with the scanning electron beam so that at any point on the target the transition occurs just after the scanning electron beam has discharged it. Thus, the target alternatively views the scene area then the chopper blade. If the scene area is hotter than the chopper blade, the target will heat up during exposure and produce a corresponding positive charge pattern, subsequently discharged by the scanning electron beam. However, during exposure to the chopper blade, the target cools, resulting in a negative charge pattern which cannot be discharged by the electron beam. A positive pedestal current is therefore required.

Two methods are commonly used to produce this current: Cathode Potential Stabilised (CPS) and Anode Potential Stabilised (APS). Their respective voltage-current characteristics are shown in Fig. 3.3. In the CPS mode, negative voltages are read with positive ions created when the electron beam collides with inert gas atoms purposefully introduced into the tube before sealing. Since a uniform pedestal current should reach each part of the target,

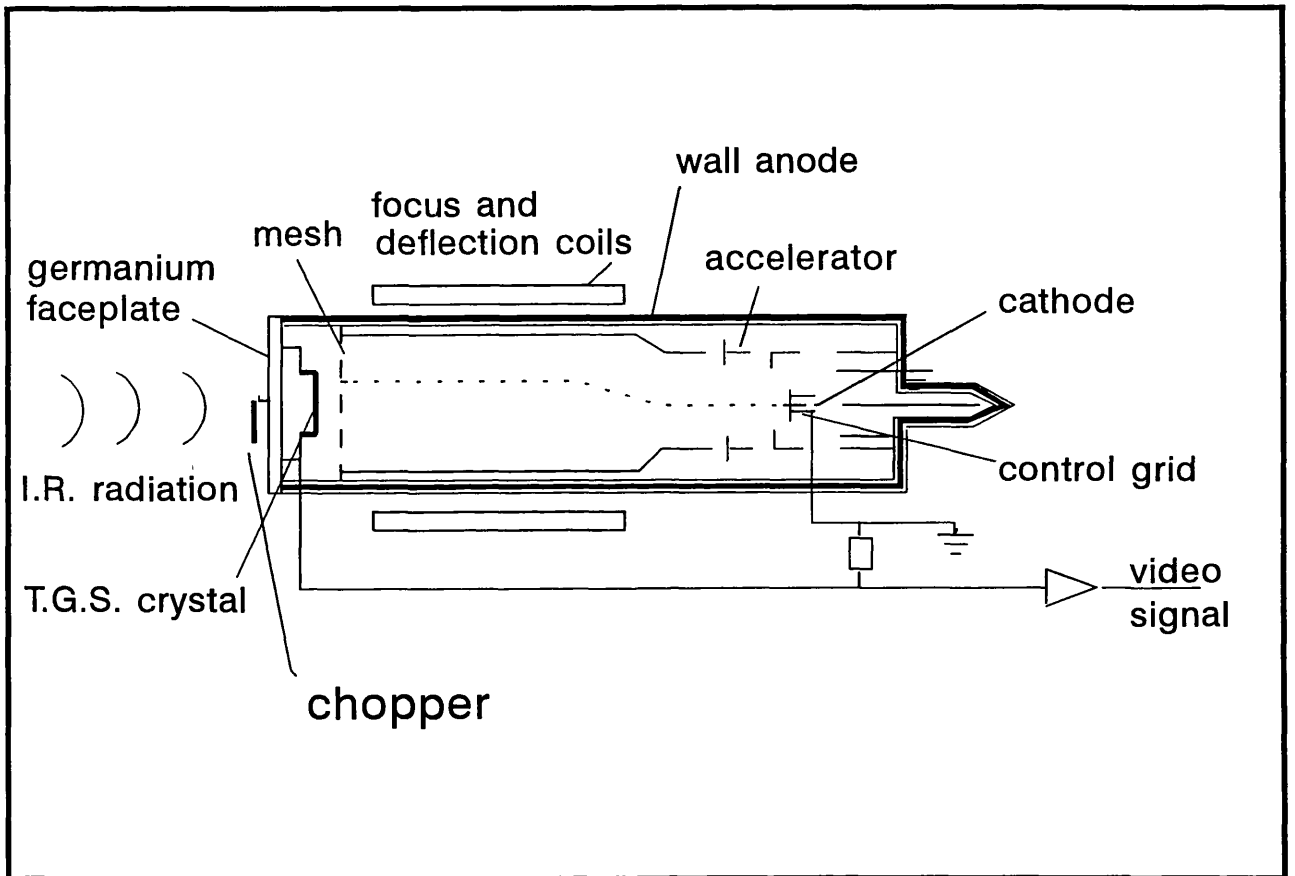


Fig 3.2: Schematic of P.E.V.

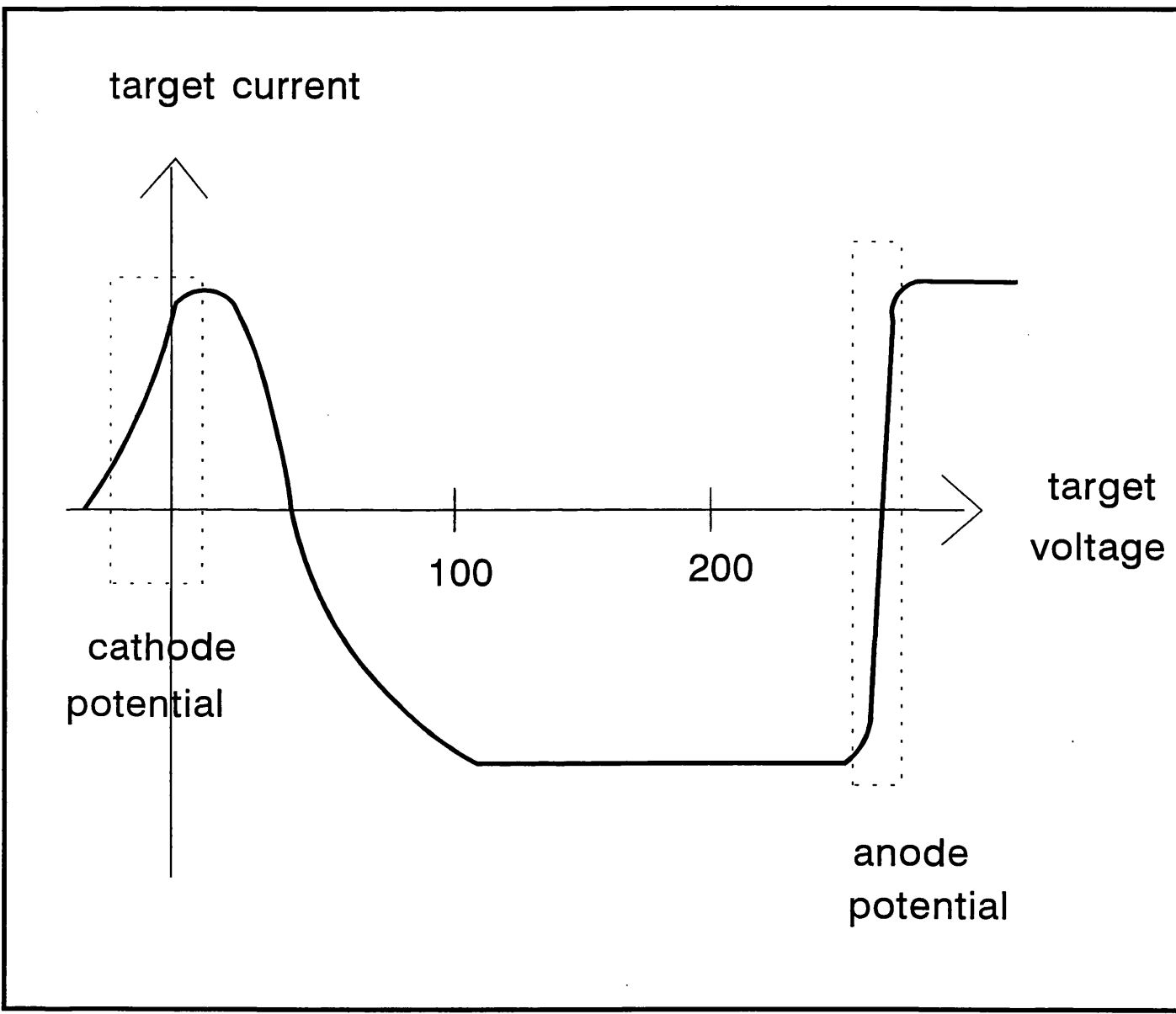


Fig. 3.3: Target voltage-current characteristics for the P.E.V.

ions from the deflection region should not be used because more ions are created near the tube axis. To overcome this, the field mesh electrode is kept approximately 20 V more positive than the focusing cylinder, thereby accelerating these ions back towards the electron gun.

The APS mode, which is less common, uses higher energy electrons which produce secondary electrons which are collected by the field mesh electrode and allow the discharge of a negative charge pattern.

The net effect of this is to produce alternate fields which are the negative of each other. This could be overcome by simply inverting every second field. However this produces image flicker as any fixed-pattern tube defects are then inverted every other field. A better method involves storing one field and subtracting it from the next field. The fixed-pattern tube defects then cancel each other out whilst the true signal is doubled.

The scanning electron beam raster pattern is chosen to coincide with conventional television systems, i.e. 625 lines, 50 Hz (field frequency), interlaced 2 : 1. The output signal is presented to a low noise preamplifier where the signal is increased to a more practical amplitude. The output signal is of the order of 1.5 nA / °C (c.f. 500 nA for photoconductive targets) so in order to avoid the signals being buried in noise, the amplifier bandwidth must be reduced which also reduces the number of lines which can be displayed. As the thermal diffusivity of the target imposes a fundamental limitation on the

resolution, the bandwidth must be chosen to minimise system noise and still permit all the electronic resolution that the thermal resolution will permit [42, 58, 59].

3.5: THE PROBLEMS OF TEMPERATURE MEASUREMENT WITH THERMAL IMAGERS

3.5(i): Introduction

In common with other temperature measuring devices, problems arise when attempting to make absolute temperature measurements with a thermal imager because of the indirect way in which this is done. All infrared detectors respond to the radiant flux per unit solid angle weighted by the spectral response of the detector. In principle, this flux consists of radiation emitted from the source, radiation reflected from the source and radiation emitted by the intervening atmosphere. However the atmosphere only presents a problem in the spectral region 8-12 μm when imaging objects at distances of the order of 1 km or greater. A typical working distance for all the results presented in this thesis is 1 m, in which case atmospheric transmission of 8-12 μm radiation is greater than 99.9%[42]. Therefore, by Kirchhoffs law, the atmosphere will not emit significant radiation in this region.

The problem of reflected radiation is deferred until section 3.5 (ii) where again the conclusion is that the effect is negligible. However, much more care must be taken with this conclusion.

This then leaves only the radiation emitted by the source. From equation 3.1, the power per unit area emitted by a source is proportional to T^4 . This is further complicated by the fact that only a small proportion of the emitted radiation is transmitted through the germanium lens and faceplate. However, provided that the temperature of the surface being measured is within a few tens of degrees of ambient temperature, the output from the crystal will be approximately proportional to the surface temperature as the T^4 dependence will not be significant over a small enough temperature range [60]. This is confirmed in section 4.4(iii).

Given that the temperature variations, ΔT , that are being measured are very small compared with ambient temperature, the contrast is very poor in thermal imagers, viz. $\Delta T/300$ or of the order of a few percent. However, in P.E.V.'s, the modulation of the incident radiation by the chopper blade provides an AC coupling of the radiation flux with the pyroelectric signal and this eliminates the large 300 K pedestal on which the useful signal variations sit. This considerably improves the thermal contrast.

3.5(ii): The emissivity problem

This problem involves two related aspects. The intensity of emitted radiation from a source is proportional to its emissivity, ϵ , which has a maximum value of 1. Objects with $\epsilon = 1$ are known as black bodies. Sources with $\epsilon < 1$ will therefore emit less radiation with a resultant underestimation of the temperature. However, this is complicated by the fact that non-black bodies reflect a proportion of the radiation incident on their surface. Ideally, a black body source should be used to calibrate the temperature range of the camera and the source whose temperature is to be measured should approximate a black body as closely as possible.

Various researchers have attempted to measure the emissivity of human skin with the results shown in Table 3.1.

Table 3.1: Estimations of the emissivity of biological tissue

<u>AUTHOR</u>	<u>MATERIAL</u>	<u>WAVEBAND(μm)</u>	<u>EMISSIVITY</u>
Hardy [64]	human skin	0.54 - 12.5	"essentially" 1.0
Elam [60]	human epidermis	1- 3	0 - 0.7
		3 - 6	0.7 - 1.0
		> 6	1.0
Watmough [63]	human skin	2 - 6	≥ 0.98
Mitchell [64]	black human skin	0.2 - 19	0.991 - 1.015
Steketee [65]	black human skin	1 - 14	0.98 ± 0.01
	white human skin		0.97 ± 0.02
	burnt skin		0.98 ± 0.01
	human pericardium		0.95 ± 0.04
	epicardium		0.98 ± 0.01
Welsh [66]	vascular tissue	8 - 12	0.93 - 0.99

The table indicates very good agreement between the different authors work although it should be noted that for the relevant waveband for our purposes, 8 - 12 μ m, the material used experimentally was bovine pericardium. This latter point was particularly important as it is not included in the table as no relevant references could be found. However it has been assumed that its infrared properties are very close to those of human pericardium. This will give rise to a small systematic error which could be accounted for, though it should be noted that the emissivity of the material should be compared with the emissivity of the "blackbody" calibration source, which may itself be slightly less than 1.

If the reflectivity of the source is not insignificant, then it is important that the environment is relatively cold compared to the source and that all warm objects (heaters, operator, etc.) are suitably distant from the source. These precautions should ensure that reflected radiation is reduced to a negligible degree.

In addition to the previously mentioned problems, Anbar [67] has shown that the infrared emission spectrum may be altered by fluorescence and increased reflectivity induced by visible light. This problem can be overcome by viewing the source in subdued light.

One further point should be considered, particularly when viewing sources heated by laser irradiation. The infrared energy emitted by the source originates in a thin surface layer. For a true blackbody this would be infinitesimal. However, for a real material, the thickness of this layer is dependent on the absorption co-efficient for the emitted radiation (in this case, 8 - 12 μm infrared radiation). The CO_2 laser emits radiation at 10.6 μm and so its absorption co-efficient will be very similar and is approximately equal to 100 mm^{-1} for biological tissue. This means that the contribution to the emitted energy will have fallen to a value of $1/e$ at a depth of $1/100 \text{ mm} = 10 \mu\text{m}$. This will not present a problem if the tissue temperature is constant to this depth. However, the laser energy deposited as a function of depth has an exponential decay complicated by the effects of scattering and so the tissue temperature will not be constant. The temperature error involved is described thus (neglecting conduction and scattering)(see appendix) :

$$\Delta T_a = \left(\frac{a_i}{a_i + a_o} \right) \Delta T_o \text{ ----- (3.7)}$$

where ΔT_a = apparent surface temperature rise, ΔT_o = true surface temperature rise, a_i = absorption co-efficient in the 8 - 12 μm region, a_o = absorption co-efficient for the laser wavelength.

So for the argon laser,

$$\frac{\Delta T_a}{\Delta T_o} = \frac{100}{100 + 2} = 0.98$$

Heat conduction, which tends to produce a more constant temperature distribution will improve this value further and so there is not a serious problem. But for the CO₂ laser,

$$\frac{\Delta T_a}{\Delta T_o} = \frac{100}{100 + 100} = 0.5$$

This suggests that there could be a serious underestimation of the surface temperature when irradiating tissue with a CO₂ laser, although, again, heat conduction will dramatically improve this figure.

Although a number of potential problems relating to emissivity have been outlined, it has been assumed that they have a negligible effect on measuring the temperature of biological tissue irradiated by the argon laser. As mentioned previously, the systematic error introduced by this assumption can be accounted for, given accurate information on the tissue, laser and detector properties. However, as will be outlined in the next section and shown in more detail in following chapters this error is very small compared to errors caused by the spatial resolution problem.

3.5(iii): The spatial resolution problem

If adequate account is taken of the problems outlined in section 3.5 (ii), then the thermal imager can be used to measure temperatures of relatively large objects with confidence. By "relatively large" it is meant that the object must have a spatial dimension equal to or greater than the spatial resolution limit of the imager, otherwise the temperature will be underestimated as shown in Fig. 3.4. In addition to this, the temperature should be approximately constant over this distance. The curve of Fig. 3.4 was determined experimentally for the P.E.V. giving a spatial resolution of 6mm (see section 4.4 (i)(b) for experimental details). It should be noted, however, that there are a number of definitions of spatial resolution and the reason for choosing this one will be explained in the following chapter.

This problem arises as a consequence of the fact that point sources are not imaged as points but are spread out over small but finite areas. This could be due to heat dissipation through the detector over a frame period, an imperfect optical system, the finite electronic bandwidth, the finite scanning electron beam and/or scattering at the detector surface. The biggest contribution in the P.E.V. comes from heat dissipation and research has shown that reticulated DTGS targets can reduce this effect by a factor of 4 [55]. However, a great deal of expense is required to achieve this.

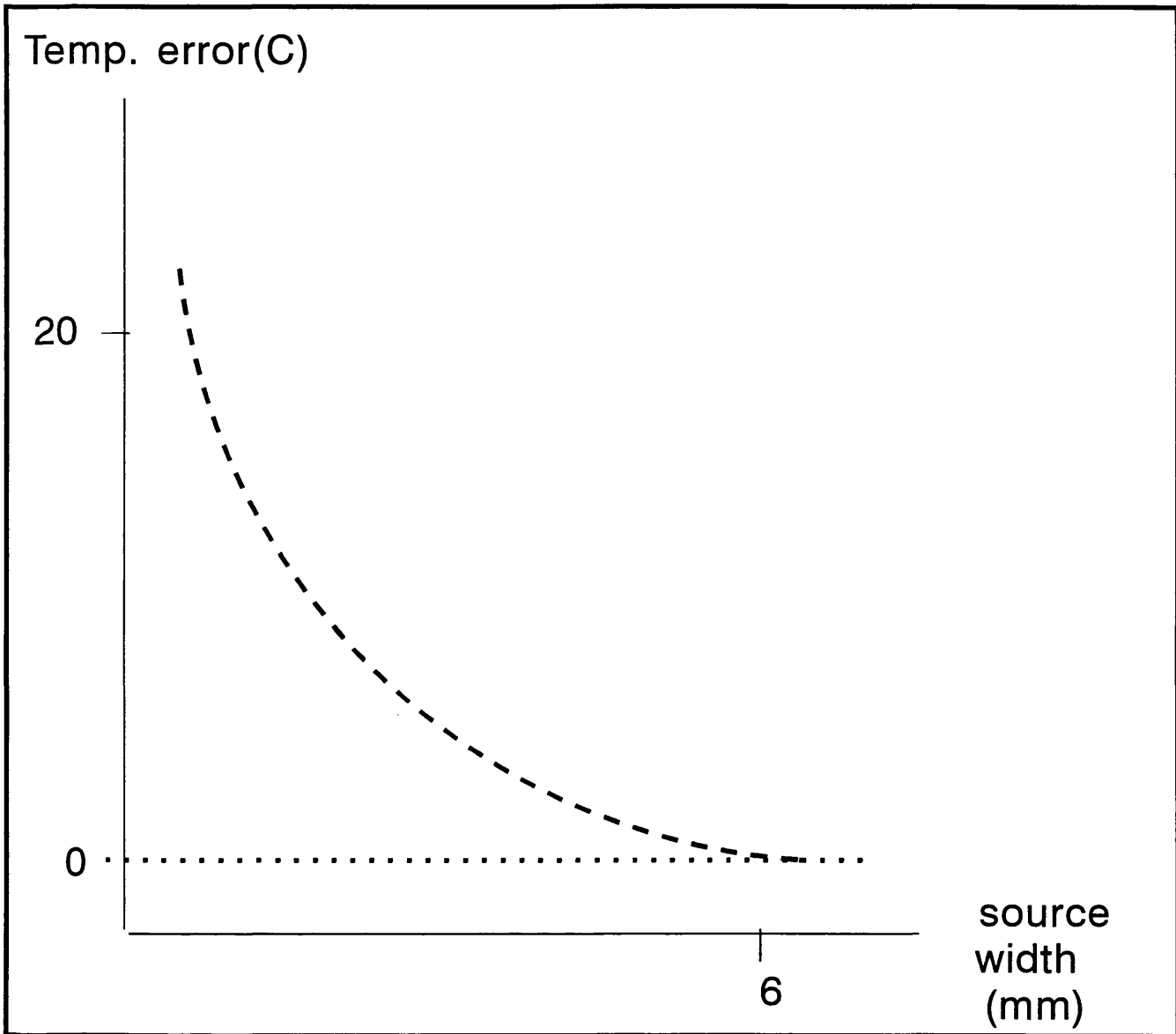


Fig. 3.4: Temperature error as a function of source width

The next biggest contribution comes from the optical system and, again, improvements are costly. Modern electronic systems ensure that the bandwidth and the electron beam do not have a great effect although the bandwidth should be kept to a minimum in order to reduce noise.

Finally, the scattering problem mentioned can be reduced to a negligible level by use of an efficient absorber at the detector surface. Fortunately, all of these effects give rise to the same outcome, so it is not necessary to know which of them has the predominant influence.

The effect of the above problems is illustrated in Fig. 3.5. The central point at the image receives radiation, not only from the corresponding point at the object plane but from a circle of radius 3mm around the central point. If the whole of this area is not at the maximum source temperature then the temperature will be underestimated. This is the case in Fig. 3.5 (a) because some of the radiation received at the central image point was emitted by objects with $T_a < T_s$.

This problem can be overcome by modelling "true" temperatures from a knowledge of the apparent temperature and of how the radiation from a point source is spread at the image plane. The mathematical description of this spread is known as the point spread function (PSF) and a detailed description of it is deferred until Chapter 6.

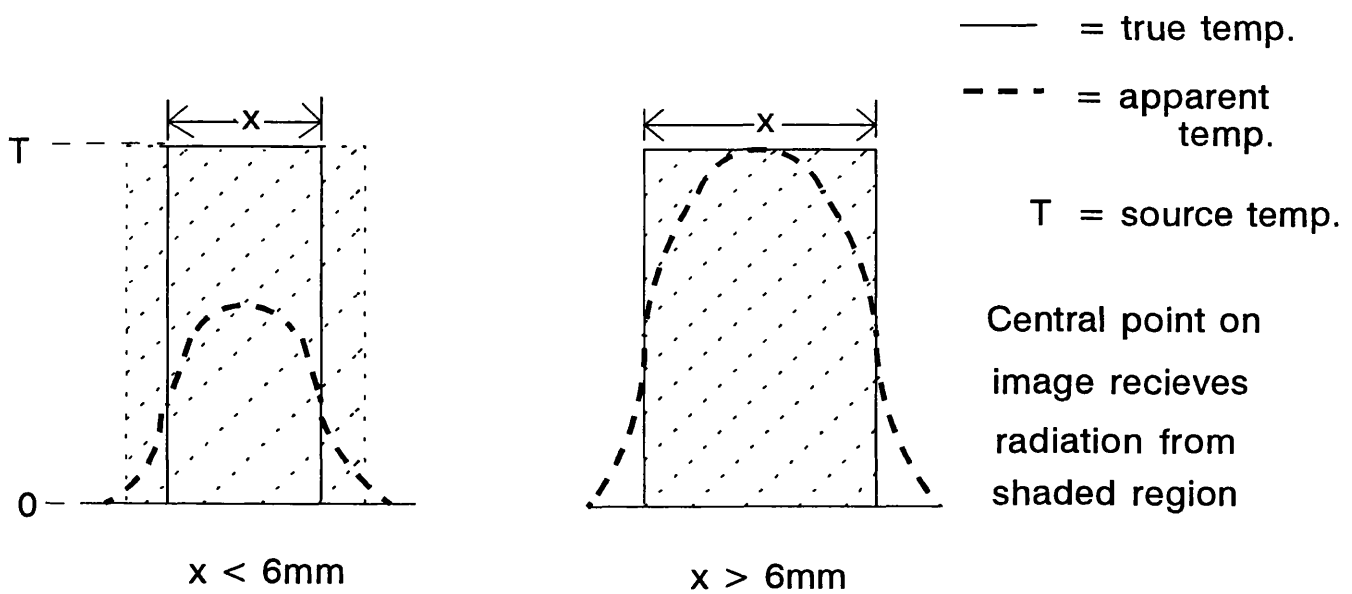


Fig. 3.5: Effect of source width
smaller than resolution limit

3.6: LITERATURE REVIEW OF TEMPERATURE

MEASUREMENTS

As the research into the laser bonding of tissue progressed in the 1980's, it became clear that a knowledge of the tissue temperatures was required in order to address some important questions. These questions included:

- (a) What is the mechanism underlying the tissue bond?
- (b) What is the optimal temperature required to create a reliable seal without irreversibly damaging surrounding tissue?
- (c) How accurate are the temperature distributions predicted by computer models?

This section attempts to show how the thermal imager can be employed in addressing these questions, whilst emphasising the limitations of the imager which, if not taken into account, will lead to erroneous conclusions.

The spatial resolution problem outlined in section 3.5 (iii) affects all thermal imagers to different degrees. In general, photon detectors have much greater resolving powers than thermal detectors.

The P.E.V. used in all experimental work in this thesis required a source width of 6mm, in order to avoid an underestimation of temperature.

A similar analysis of 2 photon detectors by Torres et al. [68] showed the required source width to be 90 μm and 2mm, respectively. Macey et al. [69]

also performed this analyses on a photon detector in 1972 and found the required width to be 8mm. This gives a rough indication of the progress that has been made in the last 20 years but it also highlights the fact that it is impossible to have confidence in a temperature measurement unless this parameter has been measured and its effect taken into account. Fig. 3.6 shows how different minimum source widths affect the measurement of temperature.

Kopchok et al. have published numerous papers relating the bonding mechanism to the temperature at the bond site. Their findings are summarised in ref. [70]. They concluded that LAVA was most effective at temperatures below 50 °C for the argon laser and between 60 and 84 °C for the CO₂ laser. However, there is no way of knowing how well their imager resolves the thermal pattern. They quote a spatial resolution of 0.2 mm but this is an entirely different concept from the one discussed in section 3.5 (iii). A full discussion of the different definitions of spatial resolution is deferred until Chapter 4.

There is a significant difference between the spot size produced by the CO₂ and the argon laser, viz. 0.22 mm and 2.7 mm, respectively, a consequence of the different optical systems employed. It is clear that the temperature measured on the specimen irradiated by the CO₂ laser will be an underestimation. This error will be offset somewhat by heat conduction which will make the affected area larger than the laser spot size. Fig. 3.7 illustrates how a cross-section of the temperature pattern will change as a

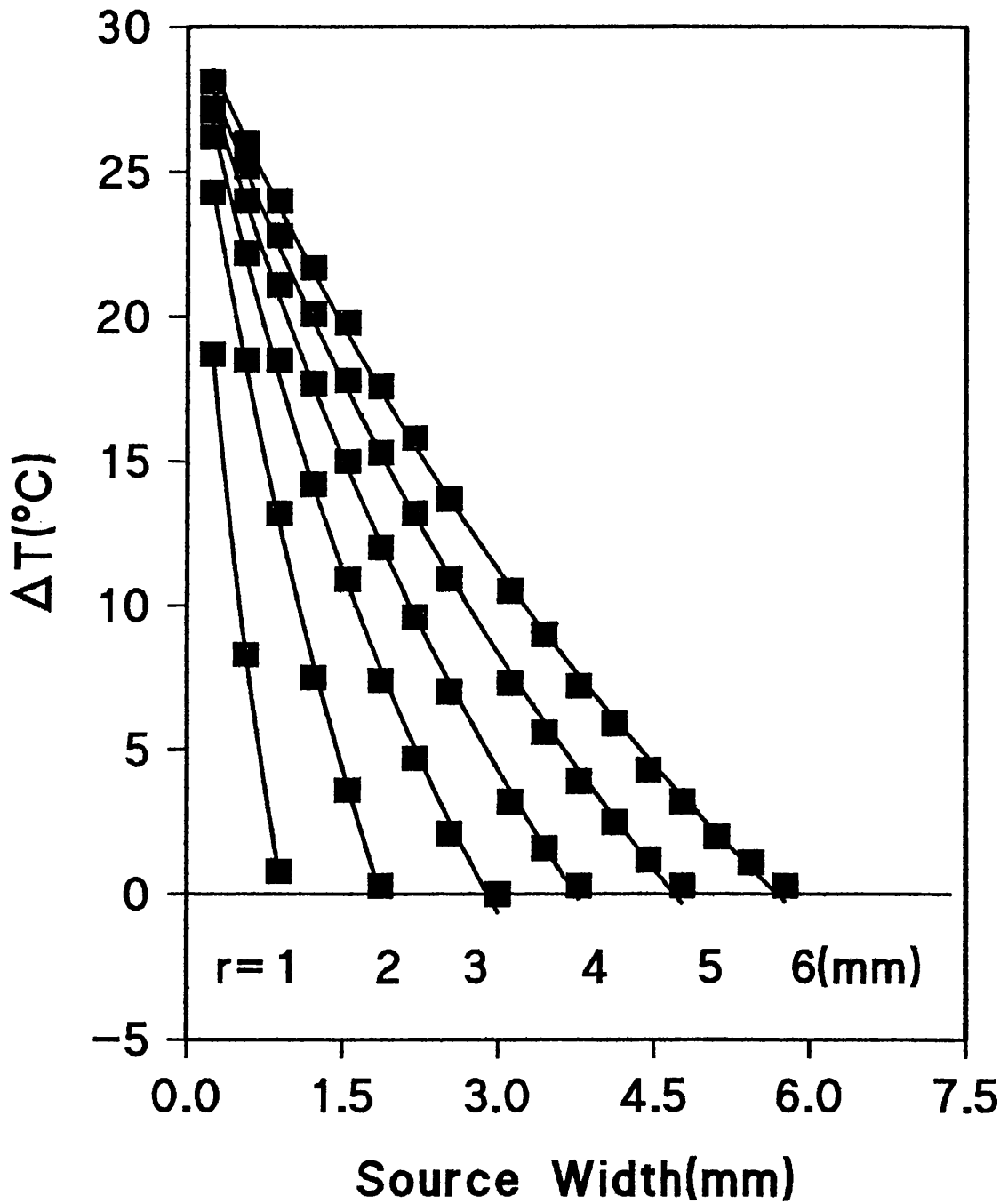


Fig 3.6: Effect of different resolution limits on the temperature measurement errors

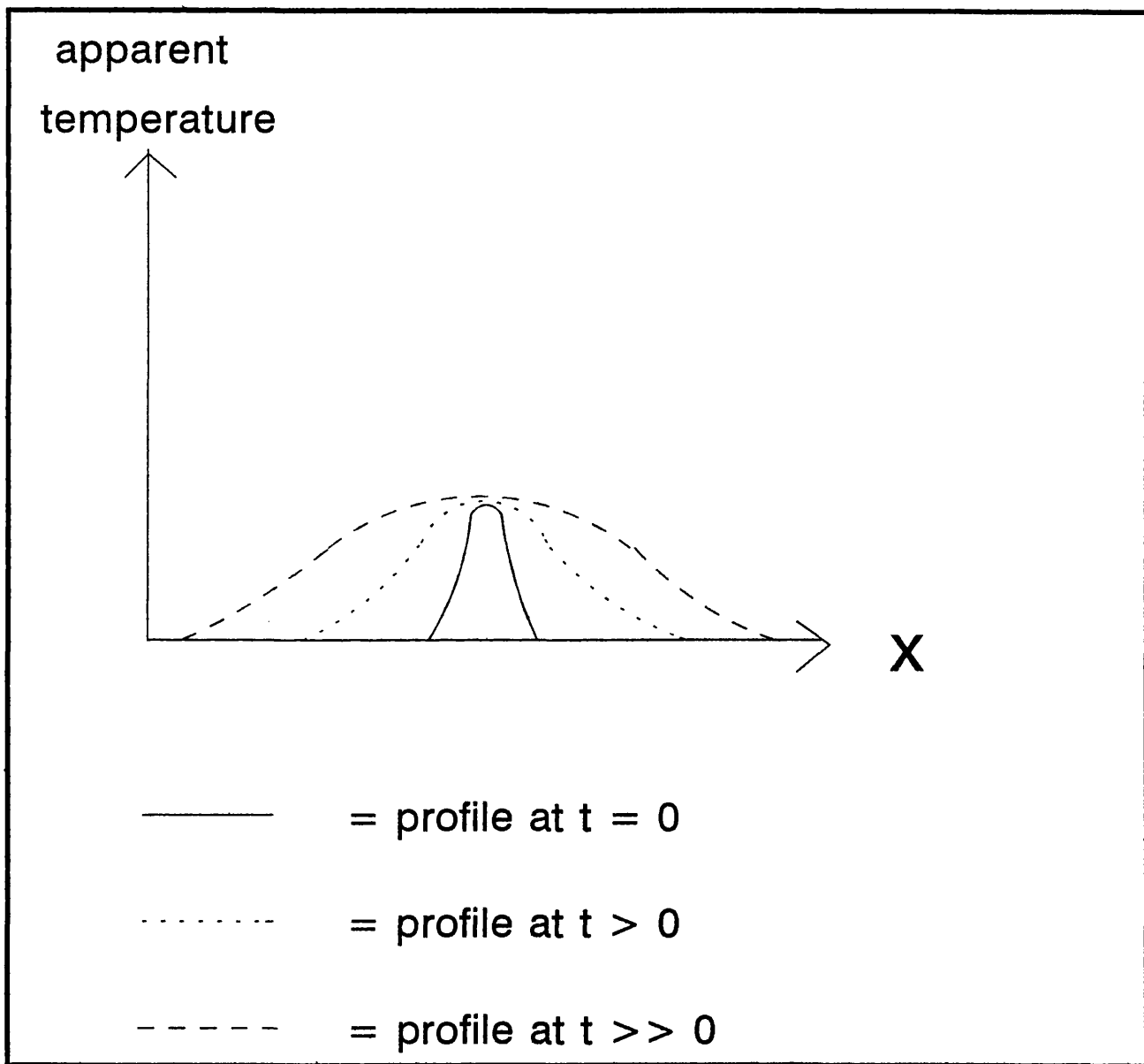


Fig. 3.7: Effect of conduction
on temperature profile

function of time. The Gaussian shape and the fact that a pulsed laser beam was used complicates the matter further.

Although the argon laser has a beam diameter more than 10 times greater than that of the CO₂ laser, there is some evidence to suggest that the temperatures measured here have been underestimated too. Fenner et al. [22] have shown that the shear strength of bonds increases significantly above the denaturation temperature of tissue, whereas Kopchoks results suggest that the best results occur at temperatures more than 10 °C below denaturation temperature. In view of this, their results must be treated with some scepticism.

The same criticisms can be levelled at the authors who have attempted to define optimum bond temperatures [70, 71, 72]. In this case, the authors may have found the optimum apparent temperature for their particular experimental set-up but this cannot be taken as the optimum temperature for any other. As explained above, the temperature underestimation, if any, is dependant on the spatial resolution characteristics of the imager and on the heat spread (see Fig. 3.7). This in turn is dependant on the power density, time of application and type of laser. All of these factors must be taken into account when defining optimum temperatures.

This may not be the case, however, when measuring the optimum temperature of a metal tipped optical fibre or laser probe used in the revascularisation of occluded arteries [13]. This laser probe has a high

conductivity which should lead to a relatively constant temperature. It also has a diameter of 2 mm which would allow it to be resolved by a high resolution imager. The measured temperatures were confirmed with a micro-thermocouple, although, as will be shown in Chapter 5, care must be taken with these measurements.

Marchesini et al. [73] used a thermal imager to test the "decrepitation theorem". This is a computer model which predicts the temperature distribution in tissue, based on laser parameters (wavelength, power density, etc.) and tissue parameters (conductivity, specific heat, etc.). They concluded that the peak temperature occurred at a depth of 1 mm and that a temperature rise of 25 °C could not be achieved beyond a depth of 3 mm, irrespective of power density and exposure time. The former conclusion can be confidently accepted as the spatial resolution problem will not obscure the position of the maximum temperature but it will cause an underestimation of the maximum value. Therefore, the latter conclusion must be treated with some caution. The authors quote a value of spatial resolution (0.1 mm) but, again, this is not the same as the spatial resolution referred to in section 3.5 (iii).

Finally, Mnitentag et al. [74] used a thermal imager to compare the effects of the irradiation of tissue by different lasers. The criticism of this work sums up the criticisms levelled at all the papers referred to in this section, viz. thermal imagers allow a qualitative comparison between different lasers or the same

laser with different output parameters, but they do not allow quantitative analysis unless the spatial resolution problem has been accounted for.

3.7: OTHER THERMOGRAPHIC TECHNIQUES IN MEDICINE

Thermal imaging has been applied to a variety of clinical investigations, generally as an adjunct in diagnosis, to assess disease prognosis and/or to monitor therapy. The most important of these are briefly described below [43, 75].

3.7(i): Vascular disorder investigations

These investigations largely involve the observation of the rewarming after the affected part has been cooled. This has been applied to assess deep-vein thrombosis, identify varicosity's and to assess the potential for increased blood flow in Raynauds disease.

It is also used to assess male infertility by monitoring scrotal temperatures and it provides useful physical data when determining the site of an amputation.

3.7(ii): Assessment of inflammatory conditions

Rheumatoid arthritis frequently results in the overperfusion of the affected tissue which gives rise to an increase in skin temperature. Thermography allows the assessment of the depth at which this is occurring and an evaluation of the effects of drugs and physical therapy.

3.7(iii): Assessment of pain and trauma

Thermography has been used in the identification of neurological dysfunction's and chronic pain syndromes that cause asymmetrical heat production. This is thought to be related to reflex sympathetic vasoconstriction and metabolic changes. It can also be used to assess tissue damage from burns, frost bite and pressure sores.

3.7(iv): Oncological investigations

It has been observed that temperature increases are generally found over malignant tumours due to increased metabolism and vascular changes surrounding the tumour. Benign tumours usually cause a reduced blood flow and hence a decrease in surface temperature. In general it has been found that tumours that bring about a large temperature change have a poor prognosis.

3.7(v): Metabolic studies

This has been limited because of the complexity of the interaction of subcutaneous heat production, blood perfusion and the thermal properties of tissue but it has been observed that metabolic stimulation by adrenaline produces an increase in skin temperature in the neck and upper back.

CHAPTER 4:

THE PERFORMANCE OF THE P.E.V.

4.1: DETECTOR PERFORMANCE

The performance of a detector is generally categorised by a measurement of 4 parameters, viz. *time constant*, *responsivity*, *noise* and *detectivity* [42, 46, 56, 75]. This section defines and briefly describes the significance of these parameters.

4.1(i): Time constant

The time constant of a thermal imager is defined as the time taken between incident radiation being cut off and the output falling to $1/e$ of its maximum value. Typically, photon detectors have a time constant of $0.2 - 5 \mu$ s whereas the P.E.V. has a time constant of approximately 1 ms. According to Jones [55], a detector must be permitted to view a pixel corresponding to part of a scene for at least 2 time constants or the output will be significantly

degraded. As the P.E.V. output is set with television display in mind, any point on the detector is discharged at the frame frequency of 25 Hz or with a period of 40 ms, well within the limit defined by Jones.

4.1(ii): Responsivity

The responsivity, R , is the ratio of the output voltage to the radiant input power, usually measured in r.m.s. volts per r.m.s. watts as the output voltage is generally a very small fraction of the d.c. bias voltage across the detector. However, this tells us nothing about how small a radiation input is detectable, except when measured in combination with the detector noise (section 4.1(iii)). The detectivity (section 4.1(iv)) is a parameter which takes account of both responsivity and noise.

The responsivity for a typical photon detector is of the order of 10^5 V W^{-1} compared with approximately 10^3 V W^{-1} for a P.E.V. and it is normally specified in terms of a peak wavelength and the chopping frequency.

4.1(iii): Noise

Detector noise is due to both thermal and electrical fluctuations and is a function of frequency. As the detector behaves like a capacitor, the noise decreases with frequency and it consequently yields a useful signal / noise ratio at frequencies far above that corresponding to the time constant [56].

Amplifier noise is dominant in determining the system signal / noise ratio. However, this is limited by the chopper blade imposing a basic frequency on the signal and then an amplifier, tuned to this basic frequency, is employed so that only that part of the noise spectrum which has the same frequency is amplified within a bandwidth set by post detector stages.

In the P.E.V., for an output current of 2 μA , the typical noise current at a bandwidth of 4 MHz is about 2 nA.

4.1(iv): Detectivity

The detectivity is the reciprocal of the noise equivalent power, NEP, which is the value of incident rms signal power required to produce a signal / rms noise ratio of 1. A more common figure of merit is the detectivity normalised with respect to area and electrical bandwidth, D^* . This figure describes the detector performance taking account of the responsivity, noise and detector size:

$$D^* = \frac{(A\Delta f)^{1/2}}{\text{NEP}} = \frac{V_s}{V_n} \cdot \frac{(A\Delta f)^{1/2}}{W} \quad \text{----- (4.1)}$$

where A is the area, Δf is the bandwidth, W is the incident power and V_n and V_s are the rms noise voltage and rms signal voltage, respectively.

The normalised detectivity allows a theoretical maximum detectivity to be calculated that would apply when the performance is limited only by noise

due to the fluctuation of background radiation. Operation in this mode is referred to as BLIP (Background-Limited Infrared Photoconductor).

Fig. 4.1 [56] shows the detectivities for various imagers. Again, the photon detector performs better than the P.E.V., with an ideal P.E.V. detector having $D^* = 10^{10} \text{ W}^{-1}$ compared with $10^{11} - 10^{12} \text{ W}^{-1}$ for photon detectors.

In practice, the detector performance is one of many parameters which affect the image. More general figures of merit which describe the combined effect of all components are described in the next section.

4.2: PERFORMANCE OF THE IMAGING SYSTEM

The previous section described parameters which relate to the detector and processing electronics. However, in order to describe the effects of other components, e.g. the optical system and the display, different figures of merit are required. They describe the spatial and temperature resolution of the system. Again, some of these parameters are of limited value for our purposes, so they are described briefly. The most important parameter is the spatial resolution which has already been introduced in section 3.5 (iii) and the various ways of describing it will now be outlined.

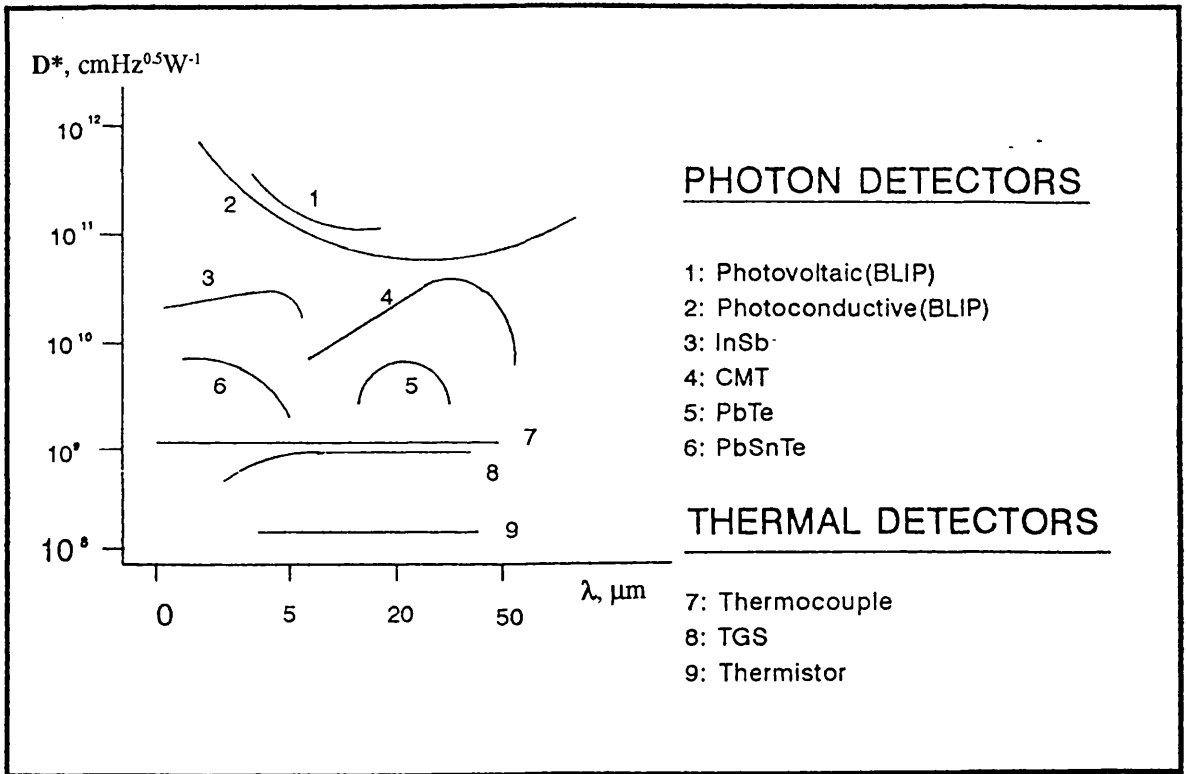


Fig. 4.1: Detectivities of various imagers

4.2(i): Spatial resolution

4.2(i)(a): Modulation Transfer Function (MTF)

This is the most common measurement made of an imaging systems spatial resolution. It describes the ability of the system to transmit the spatial frequency content of a scene. The precise definition of the MTF is the ratio of the contrast of a sinusoidal intensity fluctuation after transmission to that incident, measured as a function of spatial frequency and normalised to unity at zero spatial frequency. Fig. 4.2 shows the MTF for a variety of modes of operation of the P.E.V. Again, photon detectors are superior to the P.E.V. and their MTF differs principally at higher frequencies as the MTF falls off more slowly.

Its principal use is in the comparison of different imagers and in particular, for comparing the contribution towards a blurred output for each component of the imaging system. It is of limited use for our purposes and so a different measure of spatial resolution has been employed.

In order to give a single figure value for the MTF, the 50 % level is sometimes quoted, but this can be misleading because some curves cross over each other (see Fig. 4.2) [84].

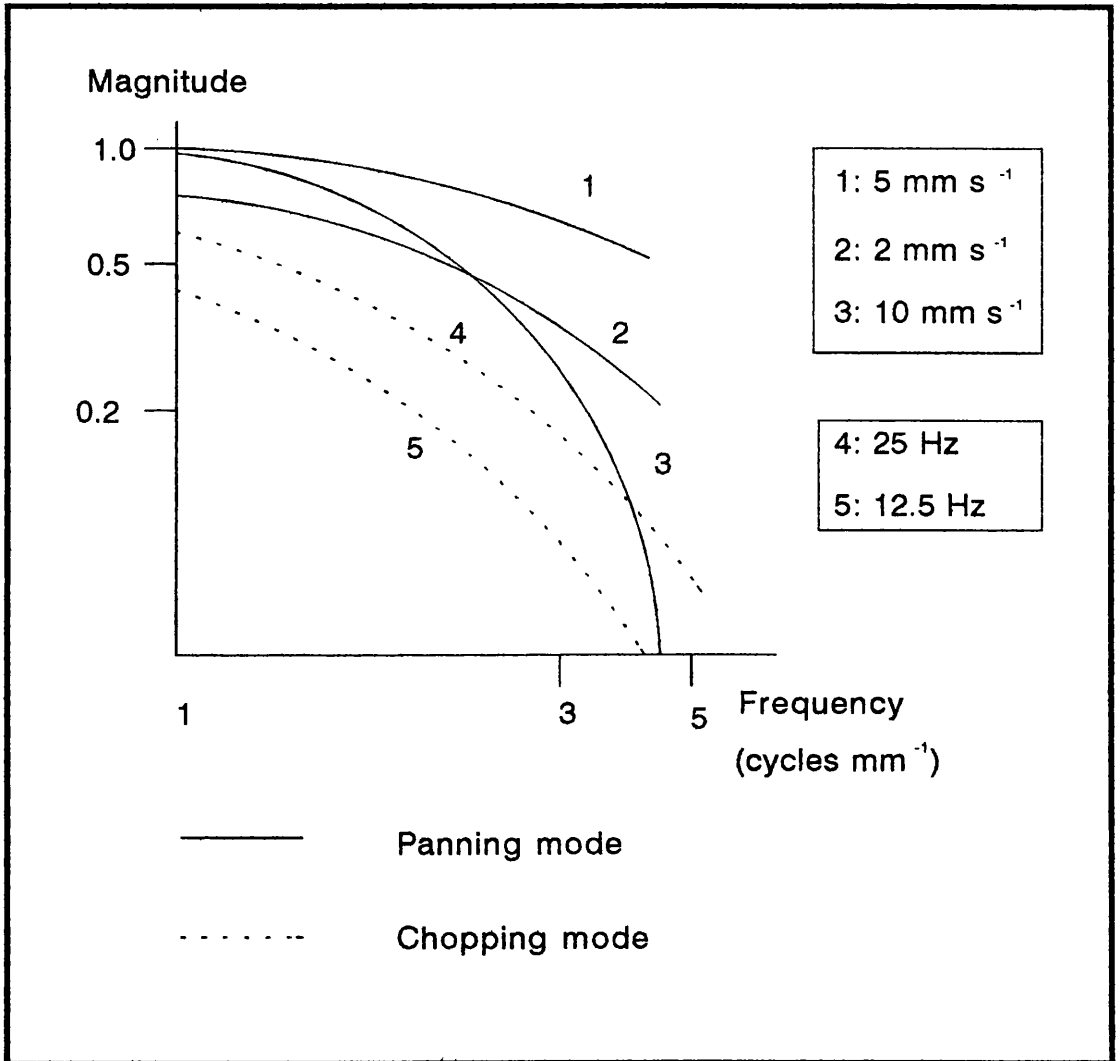


Fig. 4.2: Modulation Transfer Functions

A simpler, subjective approach involves imaging a bar pattern and determining the highest bar frequency that can be visualised in the system in line pairs per mm.

4.2(i)(b): Spatial resolution in terms of minimum source widths

Throughout the remainder of this thesis, spatial resolution is defined in terms of the minimum source width required for the accurate measurement of temperature. As described in section 3.5(iii) and shown in Fig. 3.5, if the source width is below this limiting value then the temperature will be underestimated. This parameter was chosen as the fundamental figure of merit as the MTF was considered to be too general, whereas this parameter gives a single figure value quantifying exactly how big the object has to be for full resolution. This could be useful information to have when purchasing equipment. For example, as outlined in this and the previous section, photon detectors are more powerful imaging devices, no matter what figures of merit are used to specify the performance. However, a lot of infrared imaging work involves measuring temperatures over relatively large areas, in which case, the spatial resolution becomes a far less significant figure of merit. The parameter defined here as spatial resolution gives an absolute value of the dimensions of the area required for reliable temperature measurements.

It is apparent then, that for the kind of work undertaken here, a photon detector would be preferable. Torres et al. [67] quote figures of 900 μm and 2

mm for the spatial resolution of the photon detectors that they studied compared with 6 mm for the P.E.V. studied here. However when dealing with laser-irradiated tissue, then even the camera of 900 μm resolution could not be completely relied upon to give accurate temperature measurements and so a similar computer model would be required in order to measure tissue temperatures with confidence.

The spatial resolution as defined here, also has the advantage of being a measure of how far the Point Spread Function (PSF) actually spreads. The PSF is a mathematical description of how any given point in the object plane gets spread out at the image plane and its significance will be described in detail in Chapter 6.

Another advantage of using this parameter is that it is easier to measure than the MTF and the results are given in section 4.4.

4.2(i)(c): Angular Resolution

This is defined as the angle in radians subtended by an observed object which is small enough to reduce the video signal of the system to half of the maximum signal amplitude obtained for large angles.

Similarly to the MTF, this parameter is useful as a general comparison between different imaging devices but the angular resolution has to be measured in terms of the whole imaging system, whereas the MTF can be split into the component parts of the system. It is, therefore, less usefully

descriptive than the MTF although it has the advantage of offering an unambiguous, single figure number for comparison of imagers.

Again, it is not as useful a figure of merit as that described in the previous section, although it is a particularly simple parameter to measure.

4.2(i)(d): Note on some quoted values for spatial resolution in literature relating to laser surgery

Of the research groups using thermal imagers to measure bond temperatures during laser surgery, two groups have quoted a value for the "spatial resolution" of their imager. In their numerous publications on the subject, Kopchok et al. [21, 70] quote a figure of 0.2 mm for spatial resolution and Marchesini et al. [73] quote a figure of 0.1 mm. However, it is not clear what this actually means. To quote Marchesini : "A magnifying lens mounted on the camera enabled us to obtain 0.1 mm spatial resolution of the isothermic curve." This appears to mean that for a large enough temperature gradient and at maximum gain (contrast) control, 10 isotherms could be discerned per cm. This may be the case, but it does not tell us anything about the accuracy of the temperatures described by the isotherms. For this reason, the temperatures quoted by these and other groups (see section 3.6) must be treated with some scepticism.

4.2(ii): Temperature Resolution

Temperature resolution is a measure of the smallest temperature difference that the system can detect. It can be expressed in two ways.

4.2(ii)(a): Noise equivalent temperature difference (NETD)

The NETD is similar to the NEP described in section 4.1 (iv), but instead of being a measure of the incident power required for a detector signal to noise ratio of unity, it is a measure of the temperature difference required for which the ratio is unity at the input to the display. Typical values for thermal imagers range from 0.05 °C to 0.4 °C. However, it is far more common to describe the temperature resolution by its MRTD.

4.2(ii)(b): Minimum resolvable temperature difference (MRTD)

This is another measure of the temperature resolution of the imager and although it is a more subjective measure than the NETD , it is a good measure of the maximum accuracy that a temperature can be measured to. It is defined as the smallest temperature difference between a 4-bar target and its background which allows the target to be resolved, expressed as a function of spatial frequency. However, the MRTD refers to the equipment operated at its more sensitive range and so it cannot necessarily be used when estimating temperature errors unless operated in this range. For this reason, temperature

resolution is measured in section 4.4(ii) as the MRTD over a typical working temperature range. It is dependent on the MTF and so is a function of spatial frequency and may be different for different target orientations.

Typical values for thermographic systems range from 0.1-0.5 °C. The P.E.V. has an MRTD of 0.1 °C at low spatial frequencies but this increases to 1 °C at higher spatial frequencies.

4.3: EQUIPMENT

A typical experimental set up is shown in Fig. 4.3. and the components will be briefly described.

4.3(i): The Argon ion laser

The Argon ion laser manufactured by Spectra Physics gives a continuous wave output of up to 10 W. There are a number of wavelengths from 485-515 nm giving rise to its characteristic green colour. The output is directed into a fibre optic tube which delivers an easily manipulated laser beam with very little loss of power and very little increase in divergence. In a typical experimental set up 100 mW is delivered with a laser spot size of 1.5 mm diameter, giving an average power density of 56.6 kW m⁻².

The fibre optic is clamped in an articulated arm and the laser beam can be directed by simultaneously sending a beam of red light from a low power

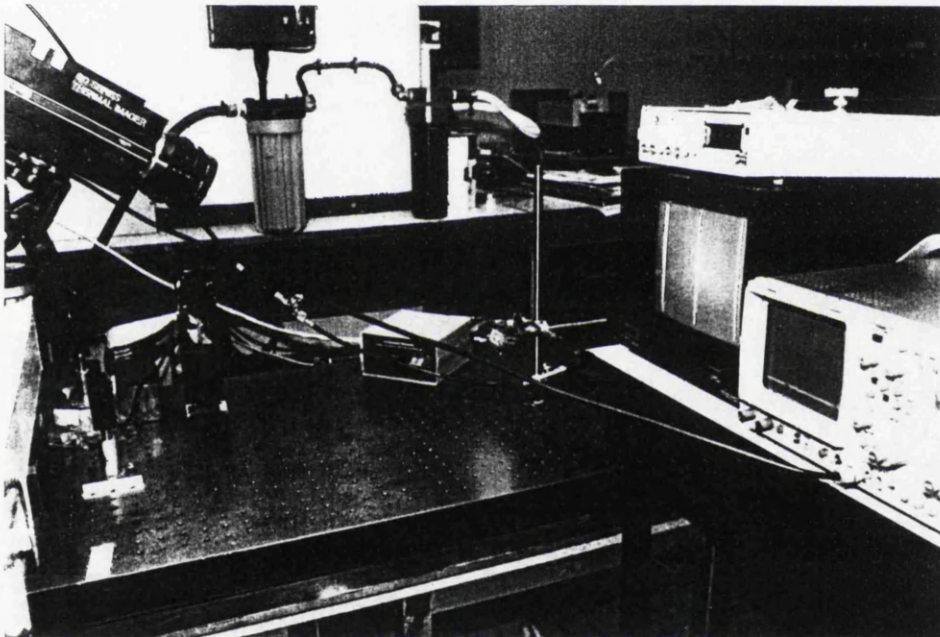


Fig. 4.3: Typical experimental set-up

HeNe laser down the fibre optic tube. This allows the laser beam to be viewed whilst wearing protective goggles which do not transmit the intense green light from the Argon laser.

4.3(ii): The P.E.V.

This was described in some detail in section 3.4. The output video signal is completely compatible with British TV standards, i.e. maximum output voltage of 1 V into 75 Ω , scanning 625 lines with a field frequency of 25 Hz, interlaced 2:1.

4.3(iii): Visualising and measuring the temperature profiles

4.3(iii)(a): Monitor

The display on the monitor is shown in Fig. 4.4. The scale on the left is a colour index, where each shade represents a temperature range, the magnitude of which is dependent on the gain of the imager. At maximum gain, each colour represents a range of 0.4 °C and as there are 7 colours plus white, the total working temperature range is 2.8 °C. In practice, this is of little use for our purposes.

Of more use is the profile on the right of the monitor. This shows a cross-section of the temperature through the centre line of the image, allowing an estimate of the maximum temperature to be read off. This is not a

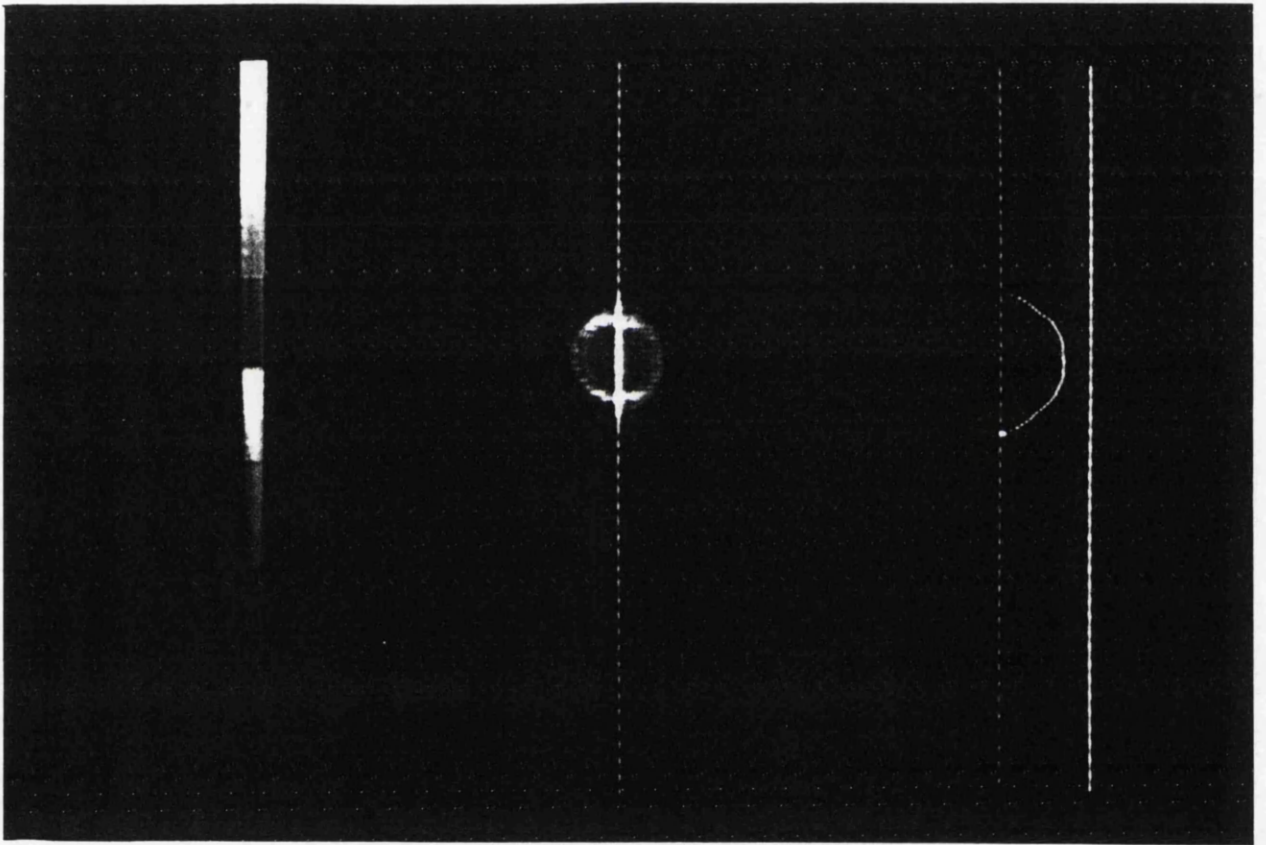


Fig. 4.4: Monitor display

particularly accurate method, allowing estimates of approximately $\pm 8\%$ of the temperature range.

4.3(iii)(b): Oscilloscope

By feeding the signal directly into a oscilloscope an output shown in Fig. 4.5 is obtained. This is another representation of the temperature profile and it is achieved by altering the time base and trigger level in such a way that only that part of the line corresponding to the temperature profile on the right hand side of the monitor is visible on the screen. It can be adjusted or contracted to suit the gradations of the oscilloscope and an accuracy of $\pm 2\%$ of the temperature range is easily obtained.

4.3(iii)(c): Recording the signals

The output from the P.E.V. can be recorded on standard video tape for subsequent analysis and an X-t recorder was used to examine the output of a particular line in detail. This was done with the aid of a device known as a line-lock, a delay generator and a linear gate. The output from the imager is fed to the line-lock input. The line-lock has two outputs, one of which is identical to the input signal and is fed to the linear gate which is a "sample-and-hold" system with a smoothing filter (see Fig. 4.6). The other output is a pulse which is triggered by a TV sync pulse and can be set to trigger on any line that is chosen. It does this by counting sync pulses after each field scan

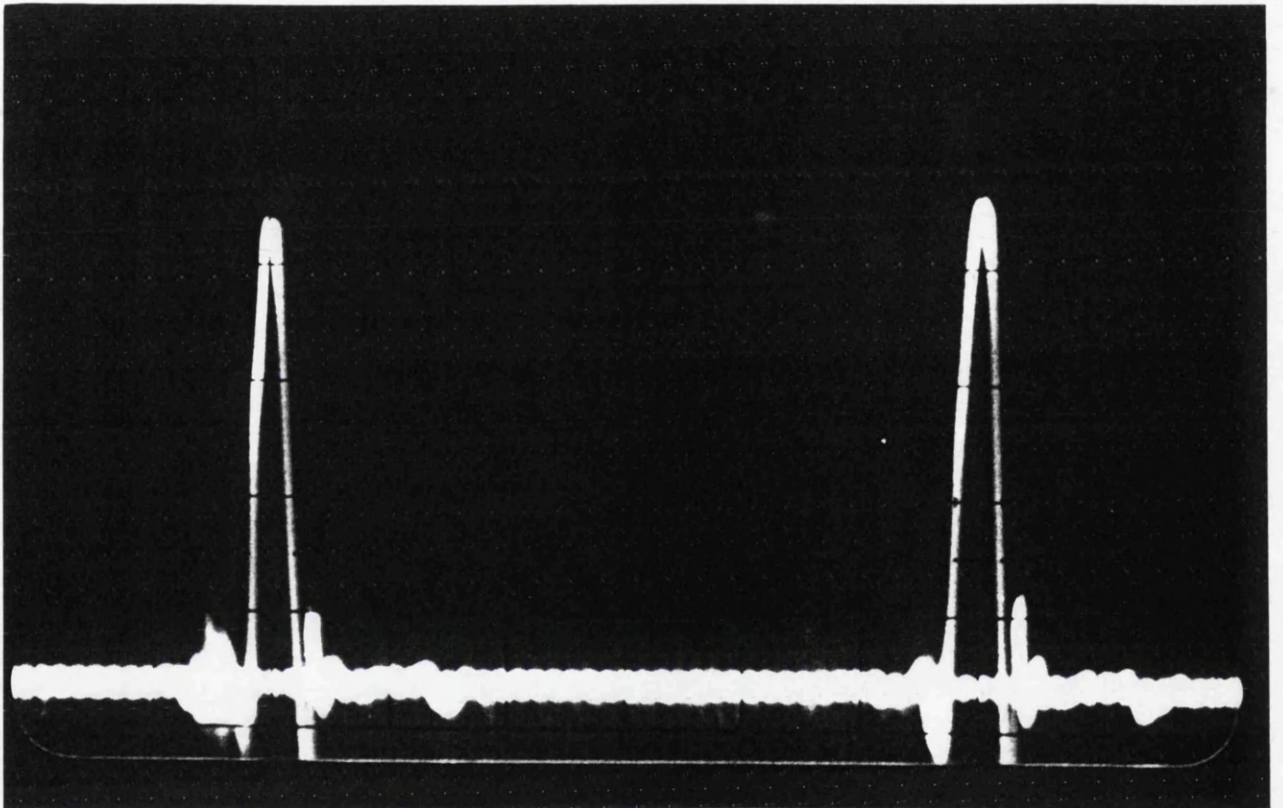


Fig. 4.5: Oscilloscope output

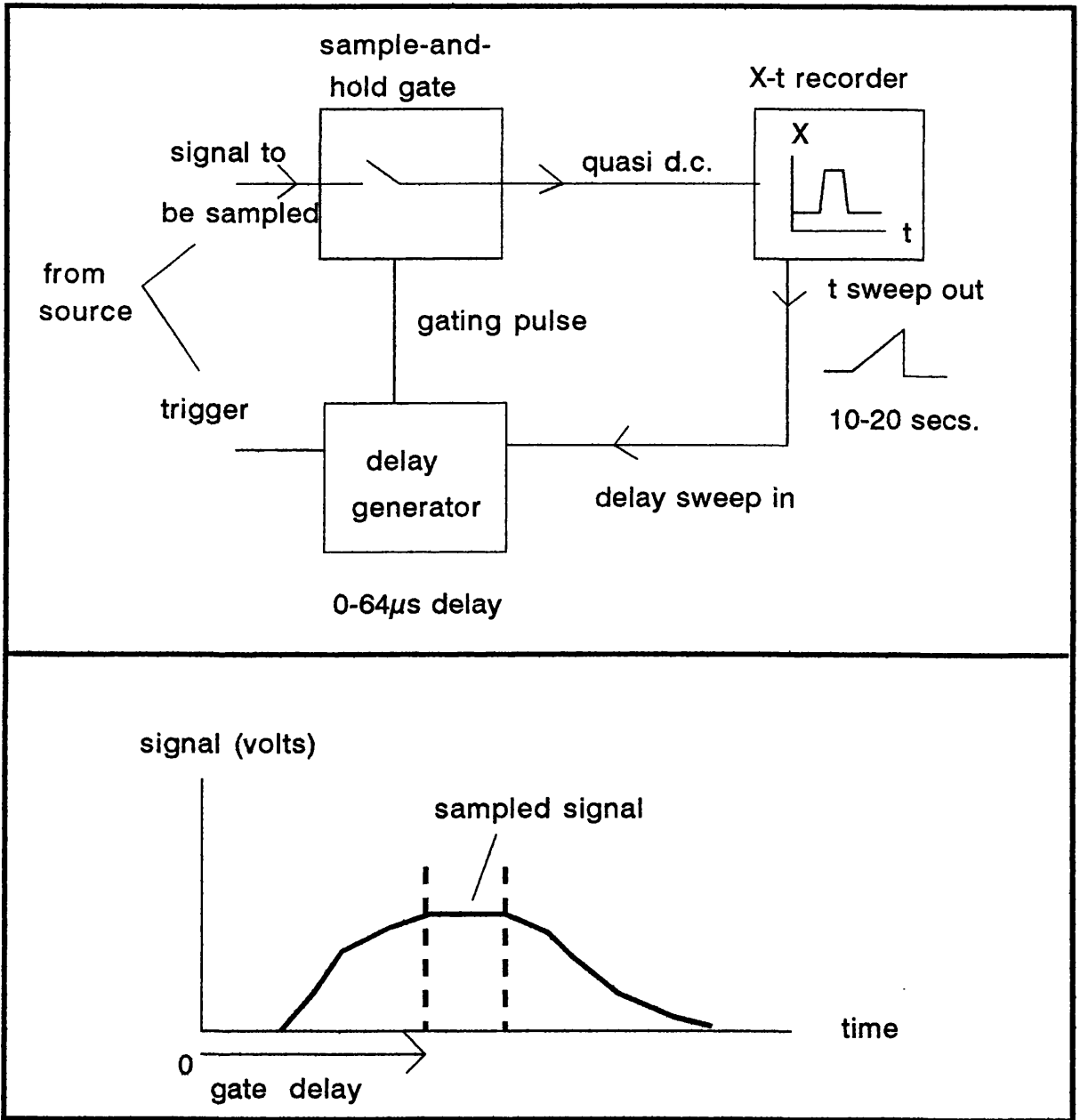


Fig. 4.6: Recording signals with
a X-t recorder

pulse and releasing its own pulse once the required number of pulses have been counted This can be used in conjunction with the oscilloscope to trigger the oscilloscope on any given TV line.

To record the signal, the trigger pulse is used to synchronise the inputs to the X-t recorder. It is fed into a delay generator which sends a gating pulse to the reference input of the linear gate every time it receives the trigger pulse. This tells the gate when to open and the output from the gate is fed to the X input of the X-t recorder. The delay generator also receives a ramp voltage such that the delay is proportional to the sweep voltage. This results in the recording of the signal across any line chosen at the line-lock.

4.4: RESULTS

4.4(i): Spatial Resolution

4.4(i)(a): Subjective measurement

Before any measurements of spatial resolution were made, an attempt was made to improve this quantity by increasing the maximum magnification of the imaging device. This works on other imaging modalities, accompanied by a decrease in sensitivity, and it works on the assumption that the PSF (see section 3.5(iii) and Chapter 6 for description of PSF) does not increase as the magnification increases. This idea is illustrated in Fig. 4.7.

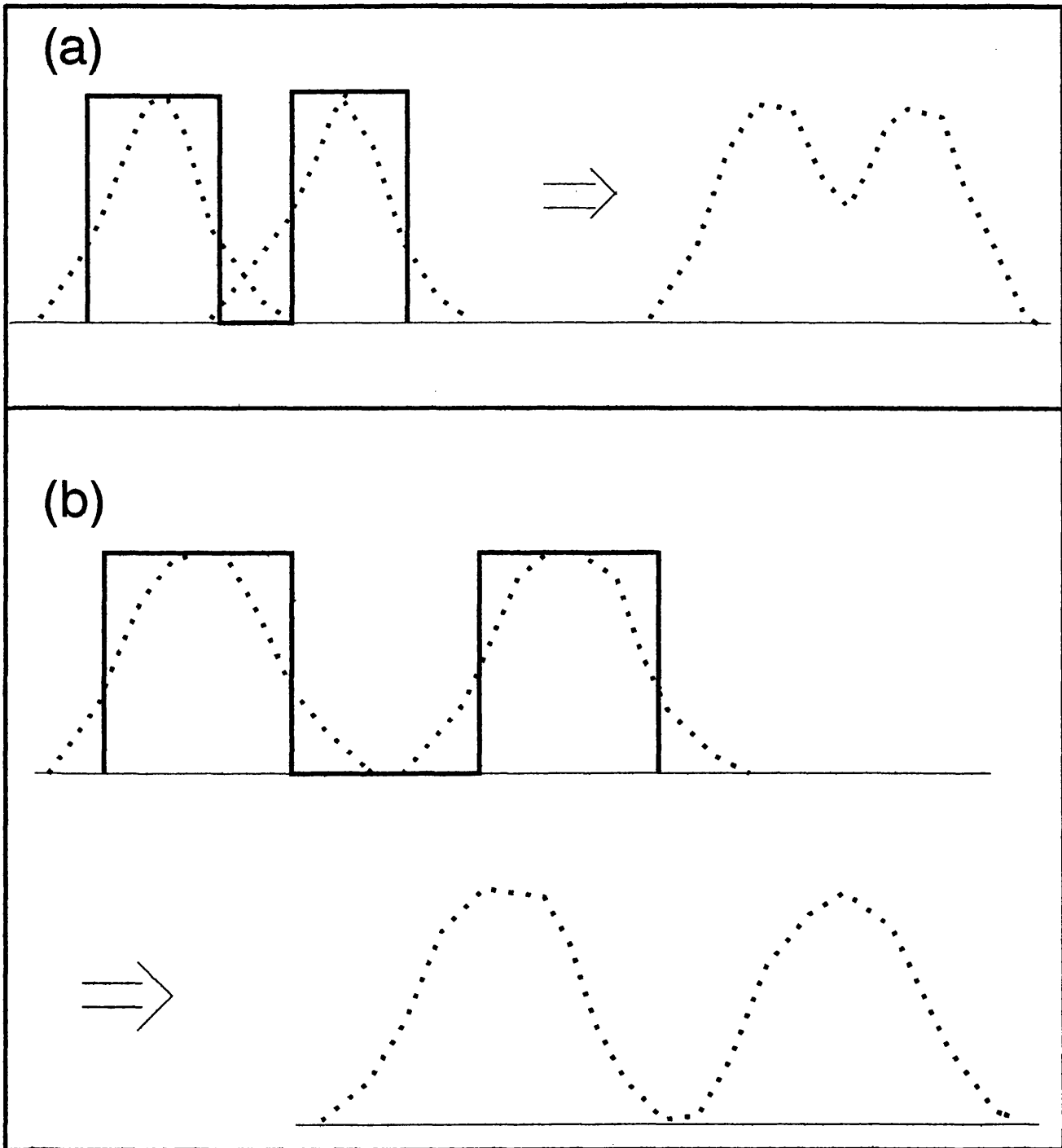


Fig. 4.7: Proposed effect of
increasing magnification

Fig. 4.7(a) represents two arbitrary heat sources. The solid line represents the sources in object space and the dotted lines are representations in image space.

The left hand sketches represent individual images and the right hand sketches represent their addition. When magnified, as in Fig. 4.7(b), the gap between the sources has increased, but the "tails" of the PSF have not. The reason for this can be seen if we consider the PSF to arise purely because of the lateral heat dissipation of the detector which is, after all, the principle cause of it. It is apparent that this heat flow will not be influenced by the magnification of the device and, hence, the PSF will not be affected.

There will be no accompanying decrease in sensitivity for the P.E.V. This is because the imager has to be focused for each object distance and then the black level (brightness) and gain (contrast) are set to give the required temperature range. No matter what the temperature range is, the output voltage is always in the range 0 V (at minimum temperature) to approximately 600 mV (at maximum temperature).

The magnification was increased by simply focusing on the source at close range. This minimises the object distance, U , and requires a correspondingly larger image distance, V , for a focused image. Hence from $M = V / U$, where M is the magnification, we have a larger V for a smaller U and therefore a greater magnification.

If it was found that this did indeed improve the resolution, then it was proposed that a steel ring would be inserted between the lens and the detector, thereby allowing a larger image distance in which to focus objects which are closer to the lens.

This idea was tested by focusing on the device sketched in Fig. 4.8 for various object distances and measuring the separation of the wires at the point where they just become resolvable. The device consists of 35 Ω insulated resistance wire connected to a power supply and wound round nails embedded in a wooden block in such a way that the distance between the wires varies continuously from 0.8-7.5 mm.

The maximum resolution obtained for three different object distances is given in Table 4.1 below.

Table 4.1: Maximum resolution as a function of magnification

OBJECT DISTANCE (mm)	SEPARATION AT RESOLUTION LIMIT (mm)
320	1.0
380	1.2
455	1.6

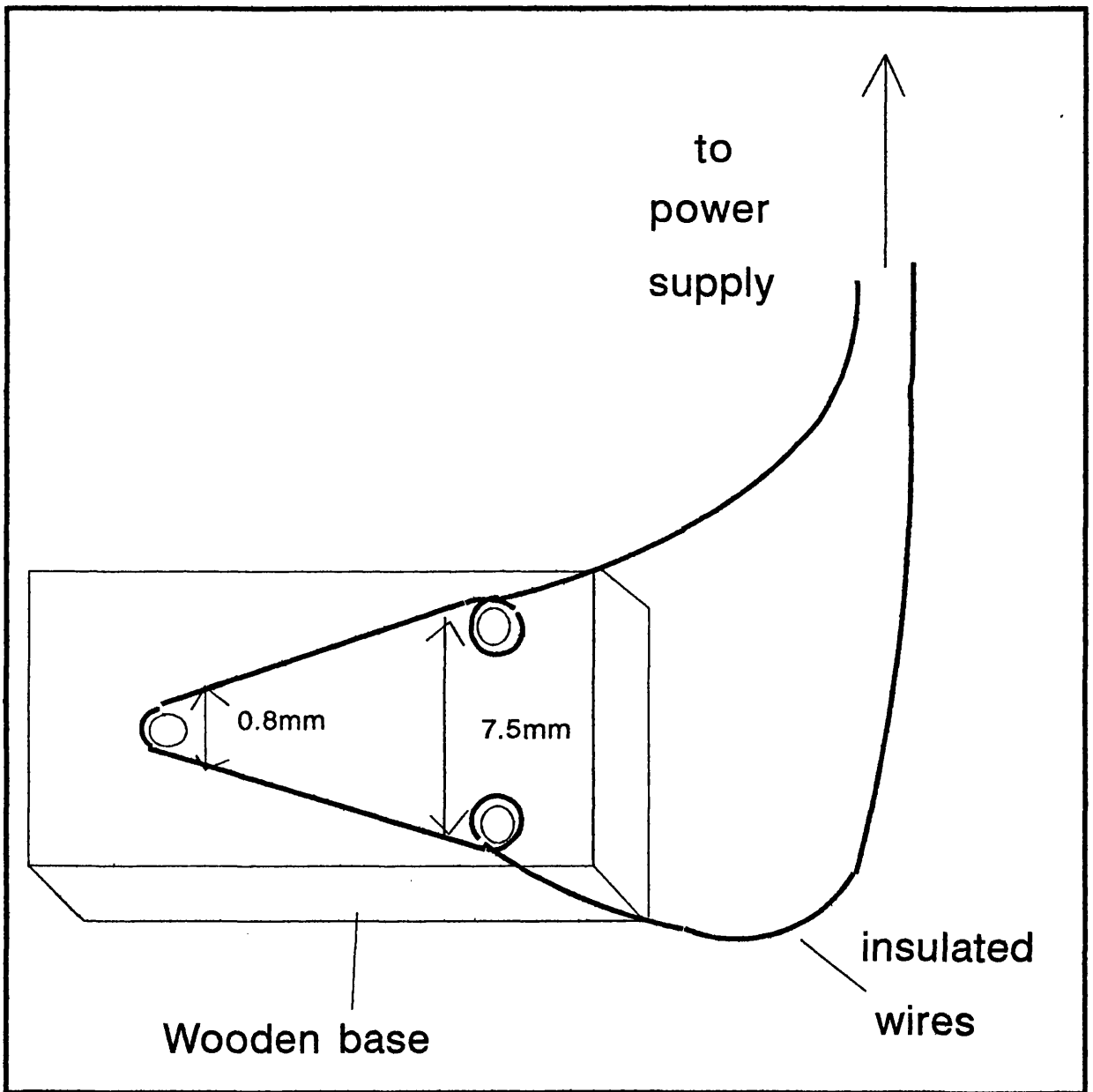


Fig. 4.8: Device for measurement of resolution

This confirms the relationship predicted above. However, as was discovered later (see section (b) below), it has no effect when it comes to improving the accuracy of temperature measurement.

4.4(i)(b): Objective measurement (I): Variable slit

The above effect was discovered when measuring the minimum source width required to measure the temperature correctly. The experimental set-up is sketched in Fig. 4.9. It consists of an optical bench supporting a variable slit. The IR source was glued to a bracket which was screwed on to the slit holder in such a way that it sat immediately behind the slit. The IR source was a metallic disc which was thermally insulated in such a way that it allowed the emission of IR radiation from one surface only. This surface was coated in matt black paint to give an emissivity very close to unity. The disc was connected to a variable power supply which allowed a wide range of source temperatures and the unit also measured the temperature of the source by measuring the voltage produced by a thermocouple which had one junction embedded in the metallic disc.

The signal, or apparent temperature, was measured as a function of slit width for two different object distances and the results are shown in Figs. 4.10 and 4.11 for two different slit orientations. The results show that the underestimation of temperature is independent of object distance and therefore independent of magnification. This is in direct contradiction to the results

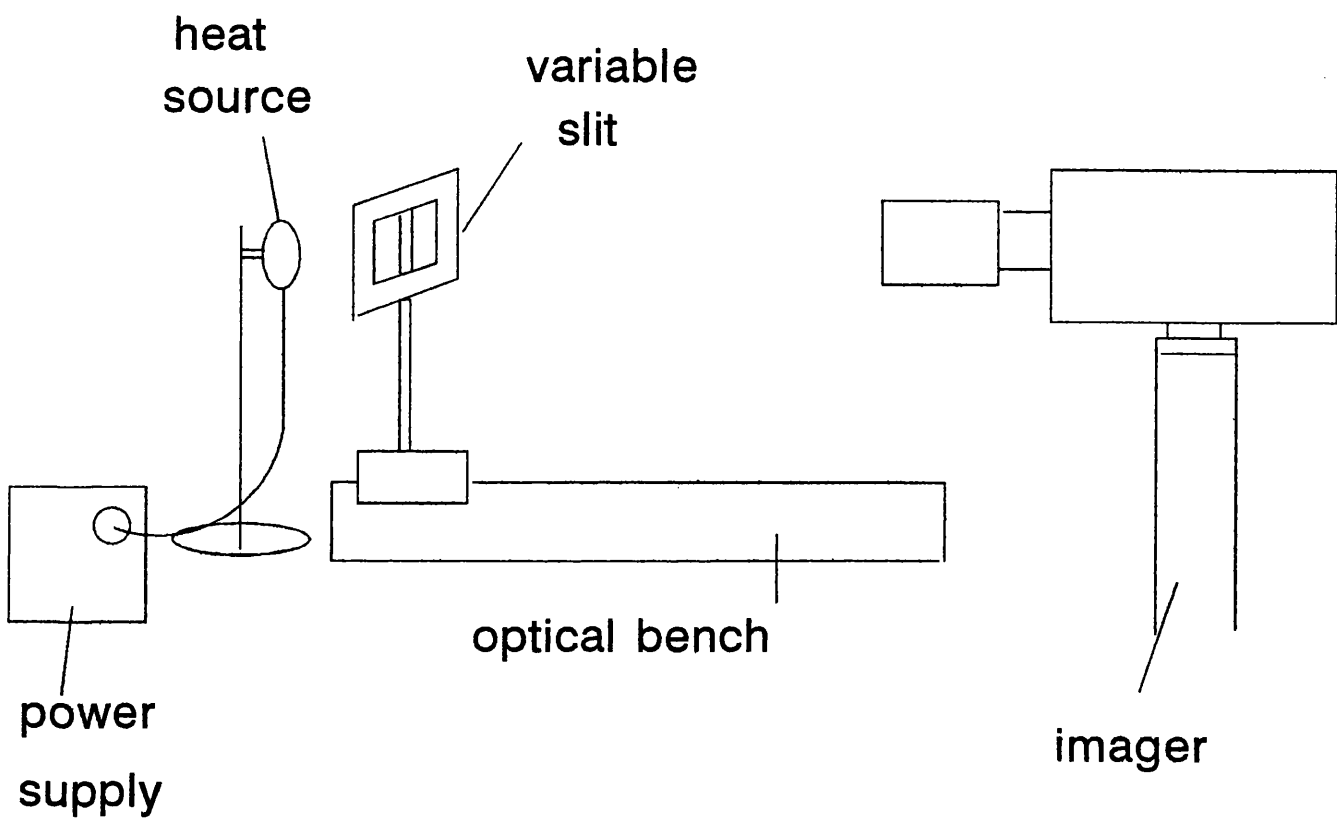


Fig. 4.9: Experimental set-up

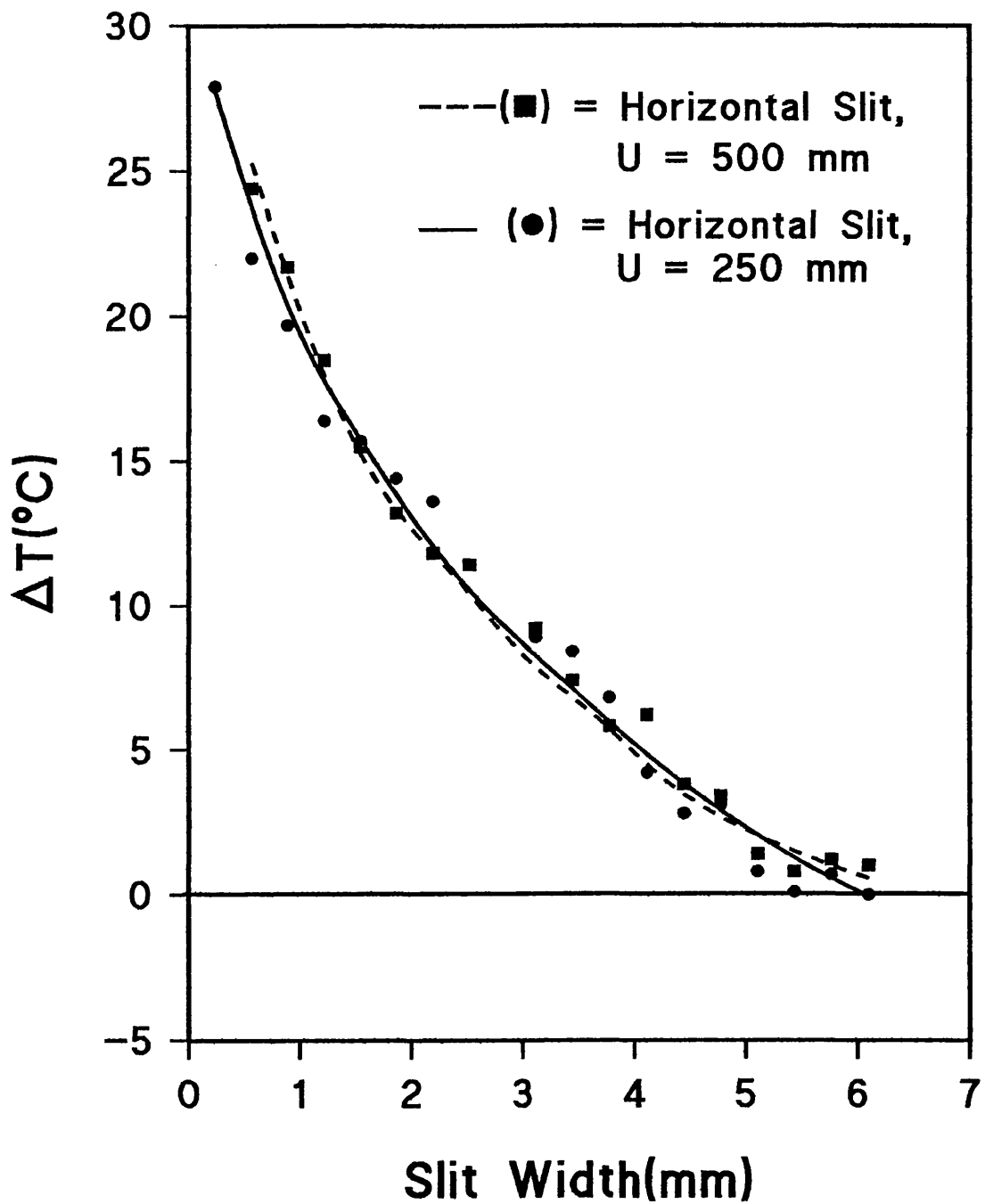


Fig. 4.10: Spatial resolution (I)

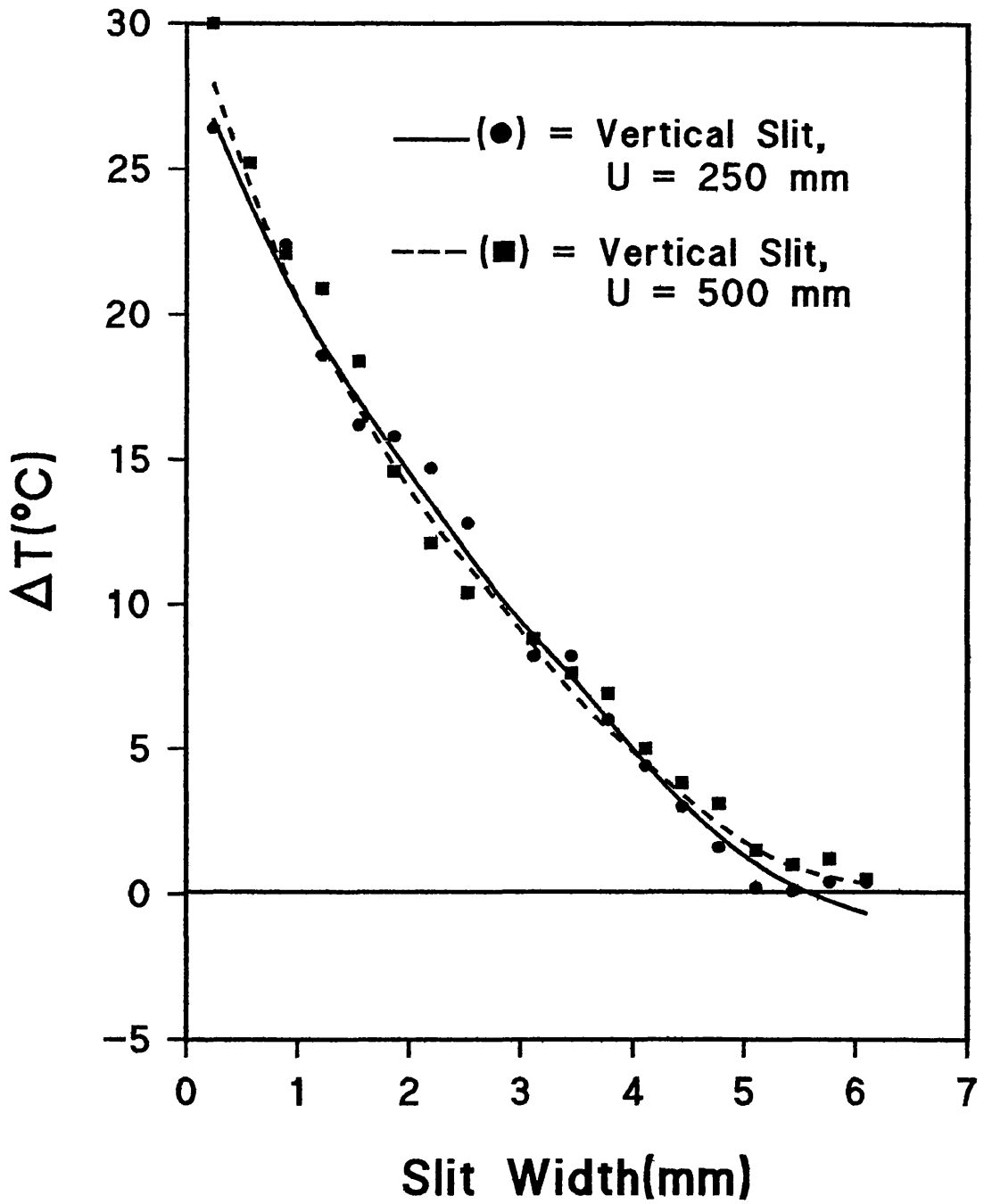


Fig. 4.11: Spatial Resolution (II)

obtained for Table 4.1 and with what was to be expected if the PSF was independent of magnification as outlined at the start of this section. However, the results of Table 4.1 come from a very subjective experiment intended purely to show that the theory had some validity and it could be discounted on the grounds that it lacked objectivity.

A more rigorous experiment, investigating the effect of magnification on the PSF is deferred until Chapter 6 when the PSF is investigated in more quantitative terms. Overall, then, the results show that magnification makes no difference to the imagers ability to estimate temperature.

The results of Figs. 4.10 and 4.11 are transposed in Figs. 4.12 and 4.13 to compare the effects of slit orientation at two different object distances. The figs. show that the horizontal resolution is identical to the vertical resolution to within experimental accuracy. This makes the computation of the effects of the PSF much simpler as only one dimension of the detector has to be considered and all measurements made along this axis can be directly transferred to all other axes.

4.4(i)(c): Objective measurement (II): Circular aperture

The signal was also recorded as a function of the diameter of a circular aperture as, in general, the camera will be imaging laser irradiated tissue which will also have a circular area. The results are shown in Fig. 4.14 with the average of the results of Figs. 4.10 and 4.11 also shown as a comparison.

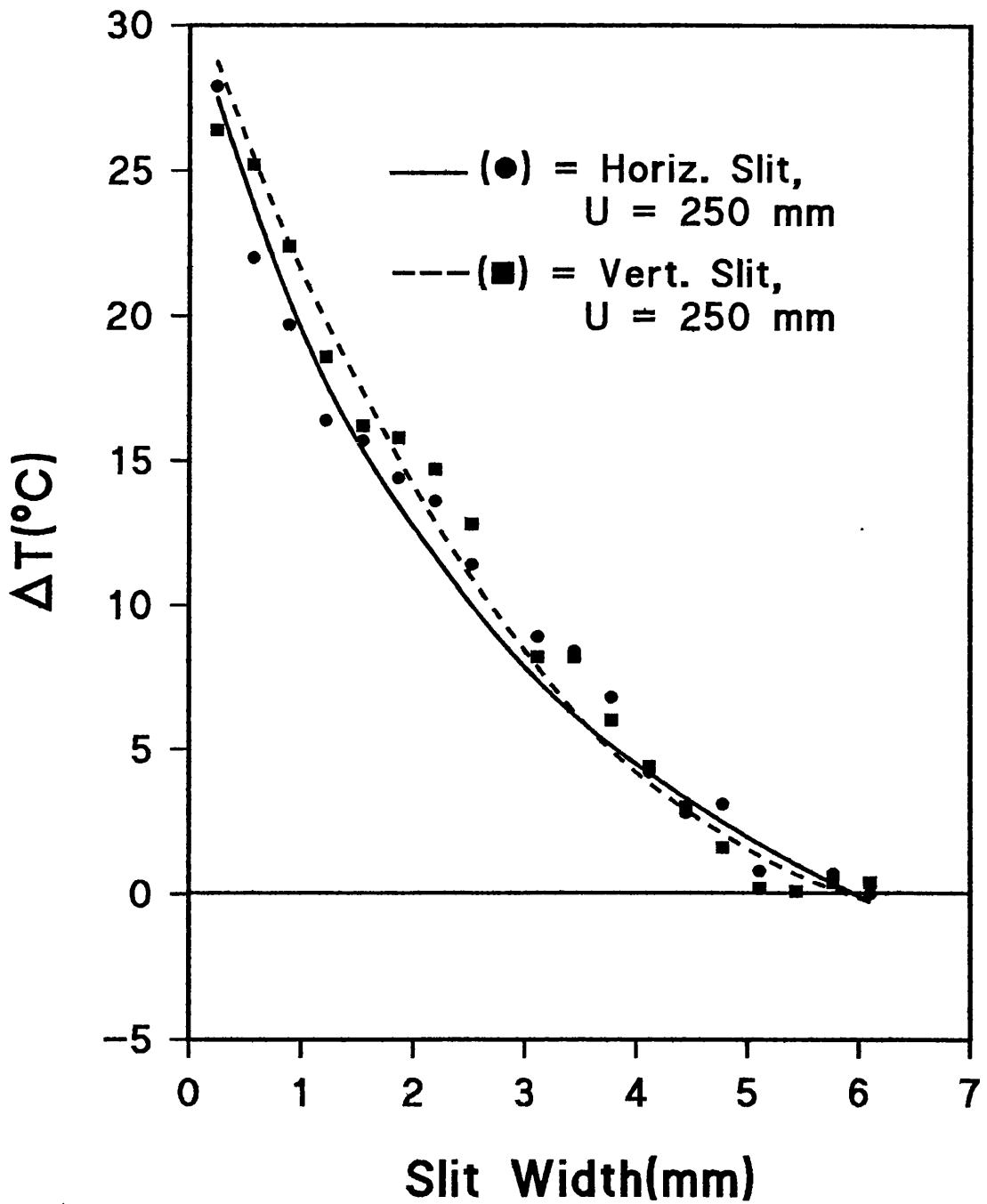


Fig. 4.12: Spatial Resolution (III)

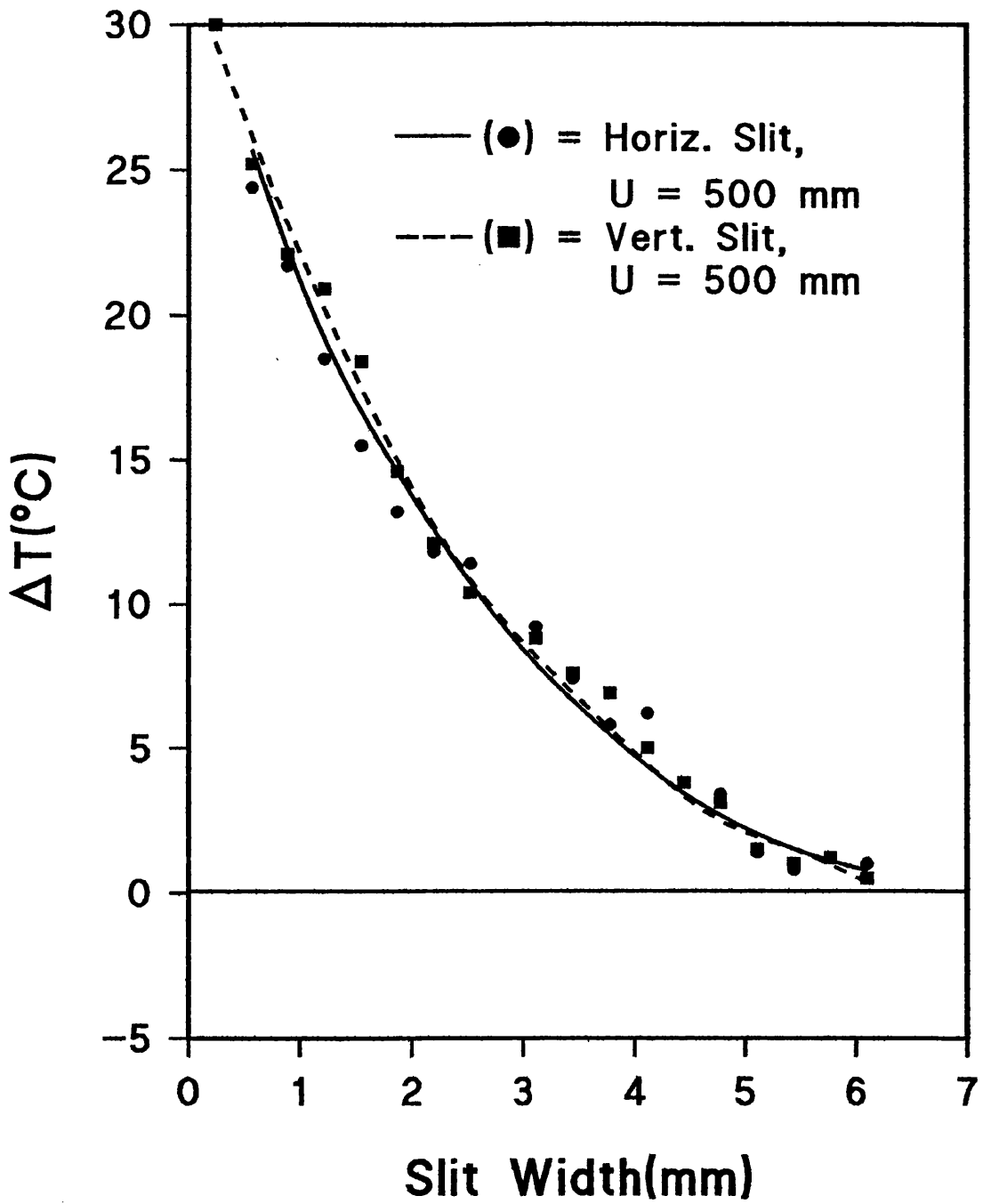


Fig. 4.13: Spatial Resolution (IV)

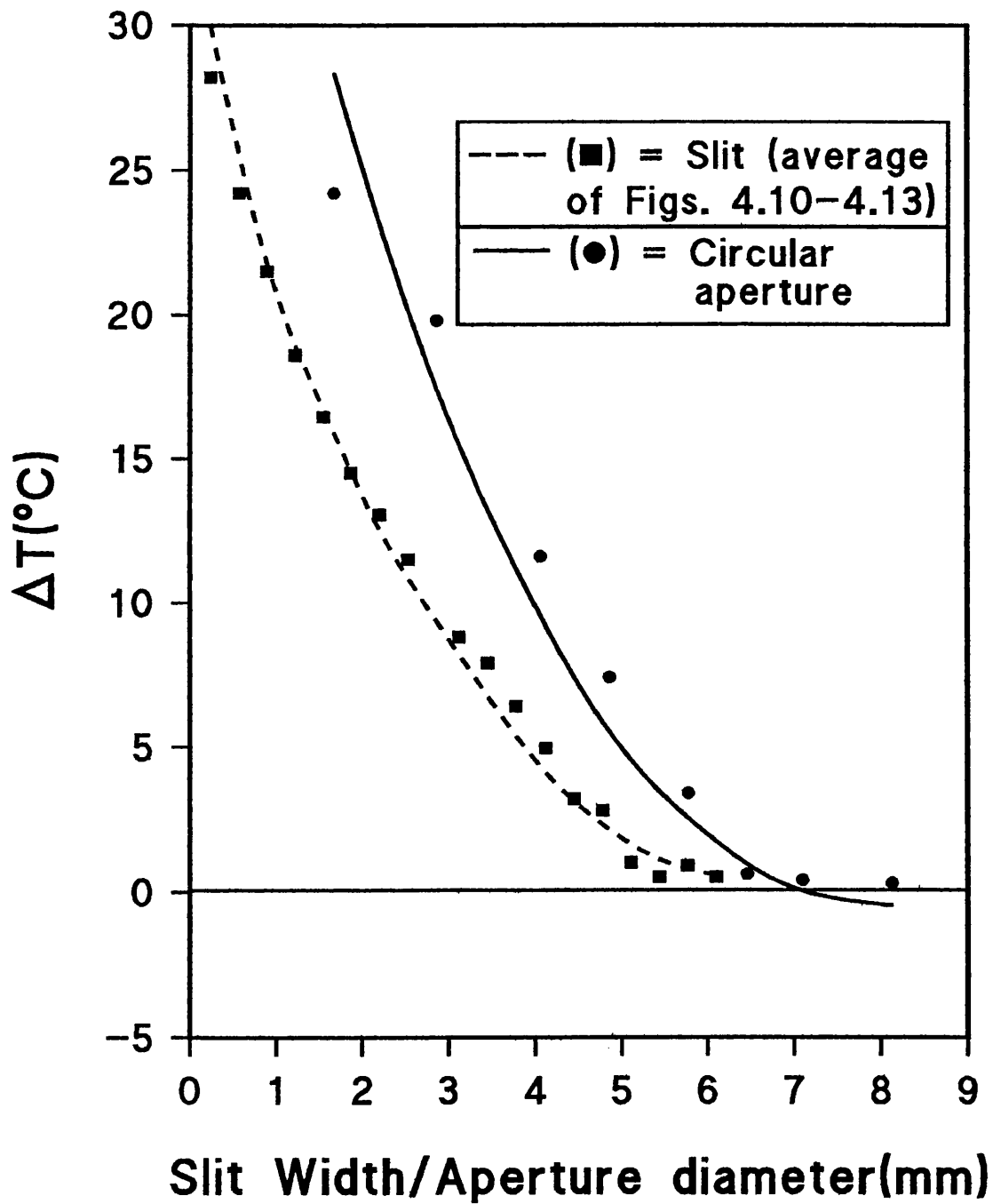


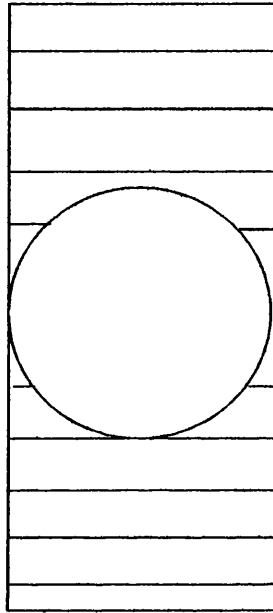
Fig. 4.14: Spatial resolution (V)

As expected (see Fig. 4.15), the circular apertures give a smaller signal for diameters below the resolution limit of the imager. However, the resolution limit appears to have increase to approximately 7 mm, which is interpreted as being due to the difficulty in aligning the heat source behind the aperture. Another possibility could be that, although the resolution limit was 6 mm in the horizontal and vertical planes of the detector it varies when the slit is oriented at angles between 0 and 90°. This was measured for a slit orientation of 45° and the resulting curve was found to be indistinguishable from the curves of Figs. 4.10 - 4.13.

4.4(i)(d): Correction factors

Figs. 4.10 - 4.14 give approximate correction factors, applicable when the source width is known. However, there are two problems with this. During laser irradiation the tissue sample, will have an approximately Gaussian temperature distribution as opposed to the uniform distribution of the black body source. For a Gaussian distribution, the peak temperature will be underestimated to a greater degree because the point on the detector corresponding to the peak temperature receives radiation, not only from the central point on the source, but from the adjacent area.

For a Gaussian source, the temperature of the adjacent area is lower than it is for a constant temperature source, leading to a correspondingly lower temperature estimation.



Shaded area represents additional source of radiation for the slit.

Fig 4.15: Circular aperture compared with slit

Secondly, Figs. 4.10 - 4.14 relate to a heat source whose temperature does not vary with time. This gives no indication as to how different temperatures affect the temperature error.

These factors were overcome to some degree by the use of "thermostrips", which allow the measurement of approximate correction factors without the aforementioned problems. A thermostrip is shown in Fig. 4.16. It consists of a strip of 8 capsules, each of which contain a dye which blackens at a well-defined temperature. Each capsule was irradiated by the laser until a small spot of diameter 0.5 - 0.6 mm appeared and the known temperature at which the dye darkened was compared with the temperature as measured by the camera. This was repeated for spots of diameter 2.6 - 2.8 mm. The use of the laser on the thermostrips will yield temperature distributions which are very similar to those achieved on laser-irradiated tissue. Fig. 4.17 shows the results, where the temperature as measured by the thermostrips is taken to be the true temperature. For small spots (0.5 - 0.6 mm), the temperature error ranged from 13 - 22 °C depending on the temperature and for larger spots (2.6 - 2.8 mm), the range was 6 - 13 °C.

The emissivity of the thermostrips was compared with that of the IR source. Any discrepancy between the two would result in an under / overestimation of the correction factor. This was done by simply placing the

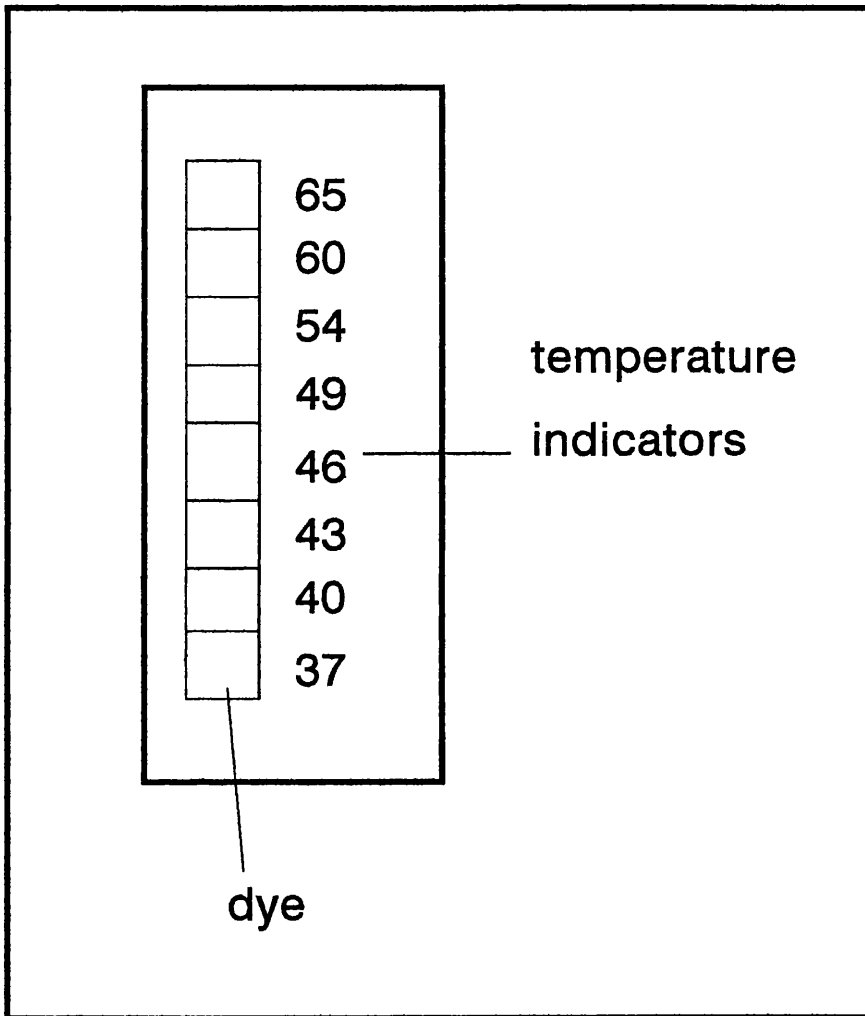


Fig. 4.16: Thermostrips

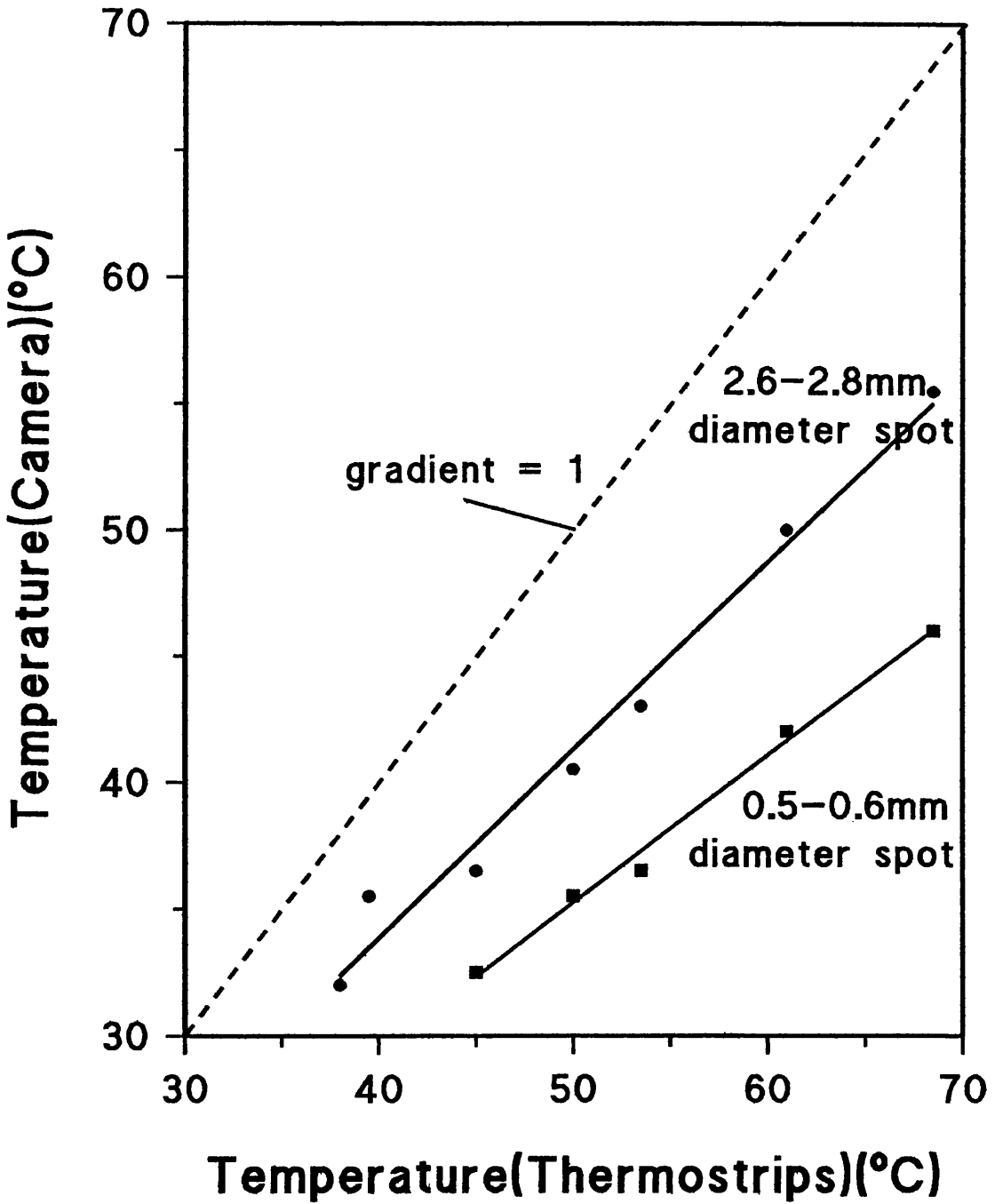


Fig. 4.17: Correction factors from thermostrips

thermostrip on the IR source and comparing the temperature at which the dyes change colour as given by the camera and as given by the thermostrip. These two temperatures are compared in Fig. 4.18 and the fact that they are equal at low temperatures suggests that their emissivities are approximately equal. The gradient of 1.07 was interpreted as being due to the thermal gradient across the thermostrip which would increase as the heat sources temperature was raised beyond room temperature.

This thermal gradient will not exist when the thermostrip is heated directly by the laser. However, another potential source of error will cause an overestimation of the temperature as measured by the camera. As noted before, the laser profile is approximately Gaussian, so when the outer edges of the capsule blacken, it is most likely that the centre of the capsule has reached a higher temperature.

This was overcome to some extent by maintaining a relatively large distance between the laser and the thermostrip which leads to a relatively flat thermal profile. Fig. 4.17 was, however, only used as a rough guide to the temperature errors involved. For a more reliable estimation of temperature, the computer model, developed in Chapters 6 and 7 is required.

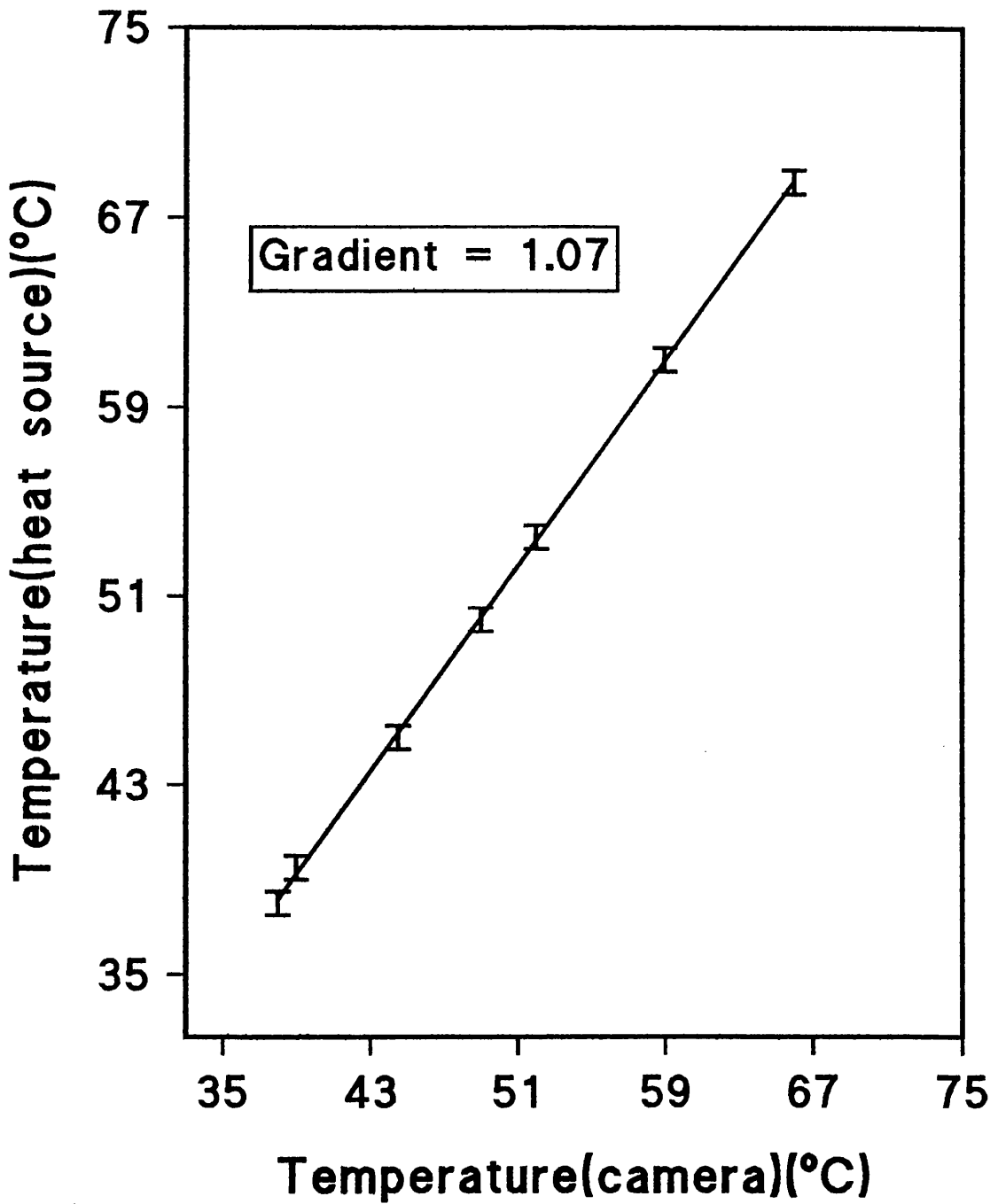


Fig. 4.18: Thermostrip emissivity

4.4(i)(e): 12.5 mm heat source

Another potential problem which required investigation concerned the fact that the results of Figs. 4.10 - 4.14 were obtained with the use of a heat source of 6 mm diameter. This heat source was used as the resolution limit was not expected to be as large as this, though using a heat source of 6 mm diameter will inevitably lead to a measured resolution limit of 6 mm or less. So, at this point the possibility remained that the resolution limit was beyond 6 mm.

A 12.5 mm diameter heat source was then obtained and the experiment repeated for slit widths equal to 5.1 - 9.7 mm. The results are shown in Fig. 4.19 and again give a resolution limit of 6 mm.

4.4(i)(f): Angular resolution

From the definition in section 4.2(i)(c), the angular resolution could be measured by one of two methods. The angle subtended could be changed by closing the slit until the video signal had dropped to 50 % of the maximum value. However this would result in an angular resolution which was a function of object distance and so this is obviously not the method to be used when comparing the results with other published work.

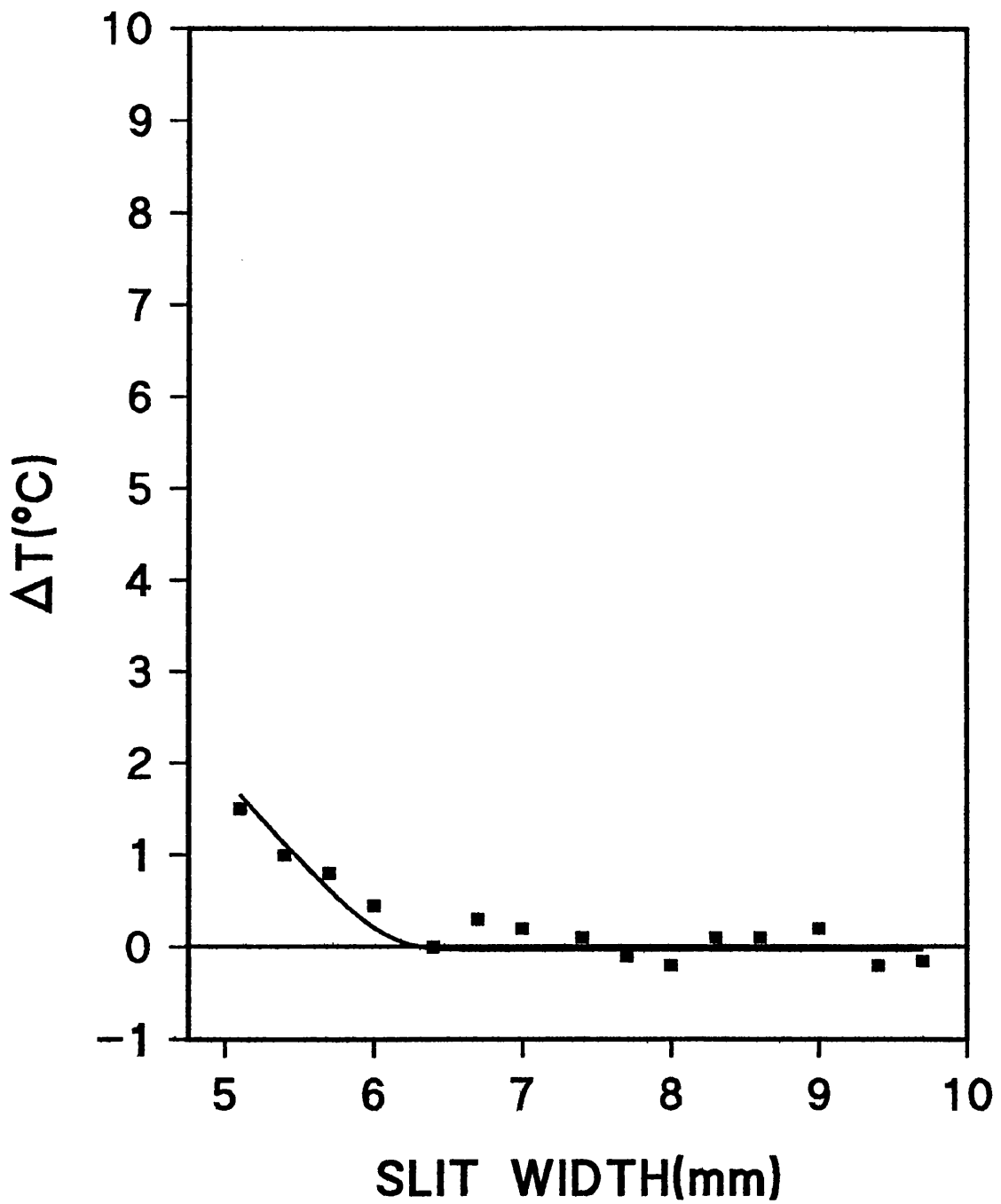


Fig. 4.19: 12.5 mm heat source

The angular resolution, then, was measured by the second method referred to above. The maximum signal was noted for a heat source focused at a typical working distance, i.e. at about 300 mm. The source was moved further away and refocussed until the signal dropped by 50%. This distance was measured as approximately 3 m for a 6mm source, giving an angular resolution of approximately 2 mrad.

In general, thermographic systems have an angular resolution which varies from 0.5 - 3 mrad [56] with the photon detectors again providing the best resolution.

4.4(ii): Temperature resolution

This parameter is a useful measure of the overall performance of the system, though for our purposes it is of limited use. The specification for a thermal imager will quote a value for temperature resolution (usually MRTD, see section 4.2(ii)) which is obviously the best that can be achieved with the system. However, throughout this project, a typical temperature range of 30 °C (30 - 60 °C) was set on the imager by adjusting the gain and black level. This compares with a minimum achievable temperature range of 4 °C, which represents an improvement by a factor of 7.5 (working temperature range / minimum temperature range = $30 / 4 = 7.5$) over the typical working range.

MRTD is usually quoted as a function of spatial frequency, which again gives a useful measure of the performance of the system but, again, this was of little use for our purposes as there was no intention of measuring temperature profiles which fluctuate rapidly in space. It was, however, relatively simple to measure at low spatial frequency as this is essentially the accuracy with which a temperature measurement can be made. With reference to Fig. 4.5, the error is ± 0.5 °C. This relates to a temperature range of 30 °C, so that at the minimum achievable temperature range, the error would be $\pm (0.5 / 7.5) = \pm 0.07$ °C, which is very close to the quoted value of 0.1 °C.

4.4 (iii) Linearity of response

As noted in section 3.2, the radiant emittance of a heat source is proportional to the temperature raised to its fourth power. It is necessary, *if this temperature dependence is significant* therefore, for the processing electronics to linearise this so that equal temperature rises produce equal changes in output signal. This was confirmed and the results shown in Fig. 4.20.

4.4(iv): Depth of field

This parameter was measured in order to ascertain how critical the focusing of the source was. The experimental set-up was the same as for most of the measurements made in this chapter and is sketched in Fig. 4.9.

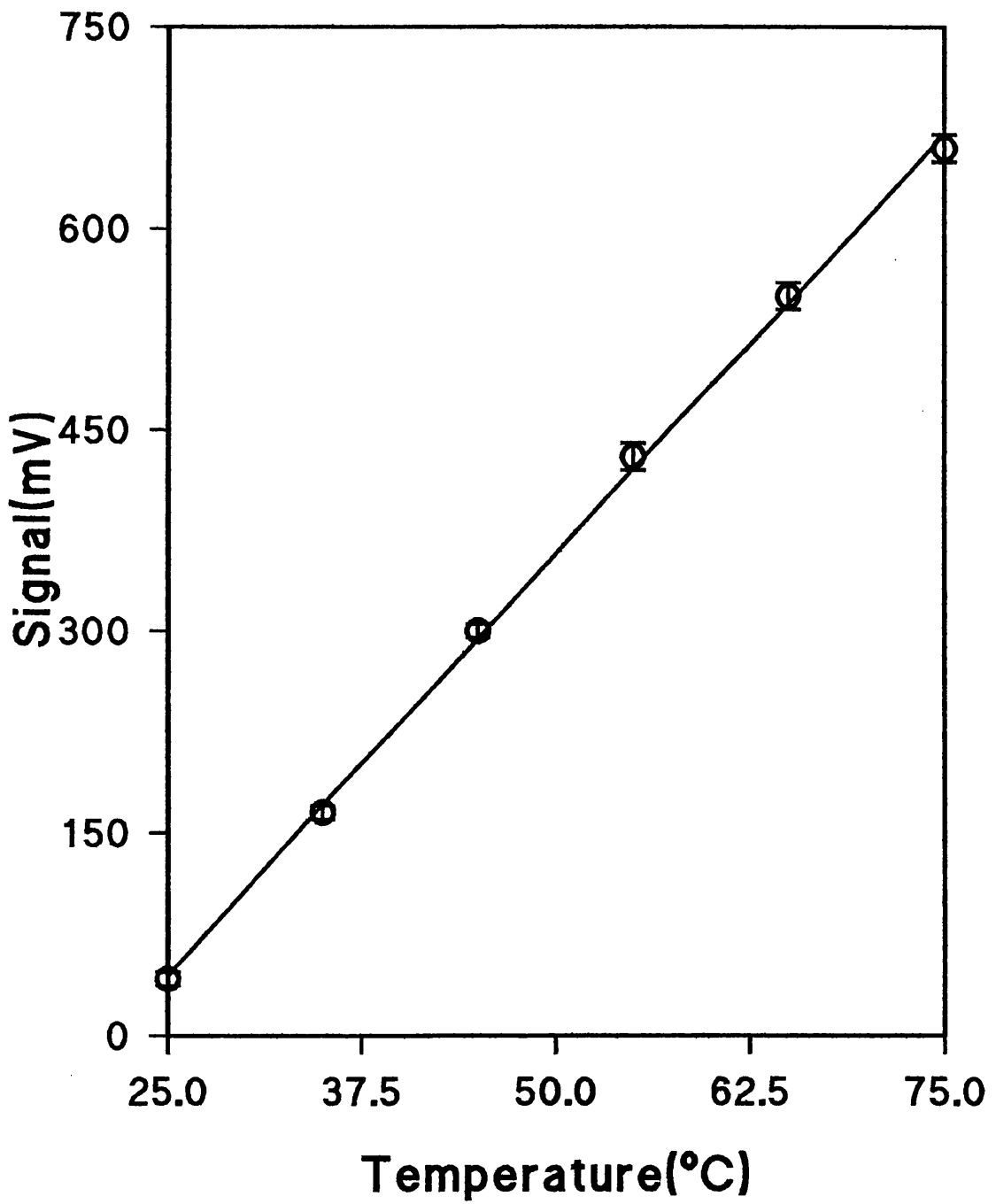


Fig. 4.20: Linearity of response

Normally, the focal plane was found by moving the slit through the focal plane and noting the signal. The focal plane was taken to be the position of maximum signal.

This position was noted to begin with and then the signal was measured at various positions around the focal plane : at 5 mm intervals at $U = 133$ mm and at 10 mm intervals at $U = 560$ mm. This was repeated for different slit widths and the results are shown in Figs. 4.21 and 4.22. Both graphs have the same scale so that they can be compared directly and two features are worth noting about them.

Firstly, the depth of field is highly dependent on the object distance. This is to be expected from the thin-lens equation

$$\frac{1}{u} + \frac{1}{v} = \frac{1}{f} = \text{const} \text{ -----(4.2)}$$

The criticality of focusing can be measured by the rate of change of the curve and by differentiating Eq. 4.2 the following table can be computed:

Table 4.2: Criticality of focusing

U (mm)	dv/du
50	∞
100	-1
200	-1/9
500	-1/81

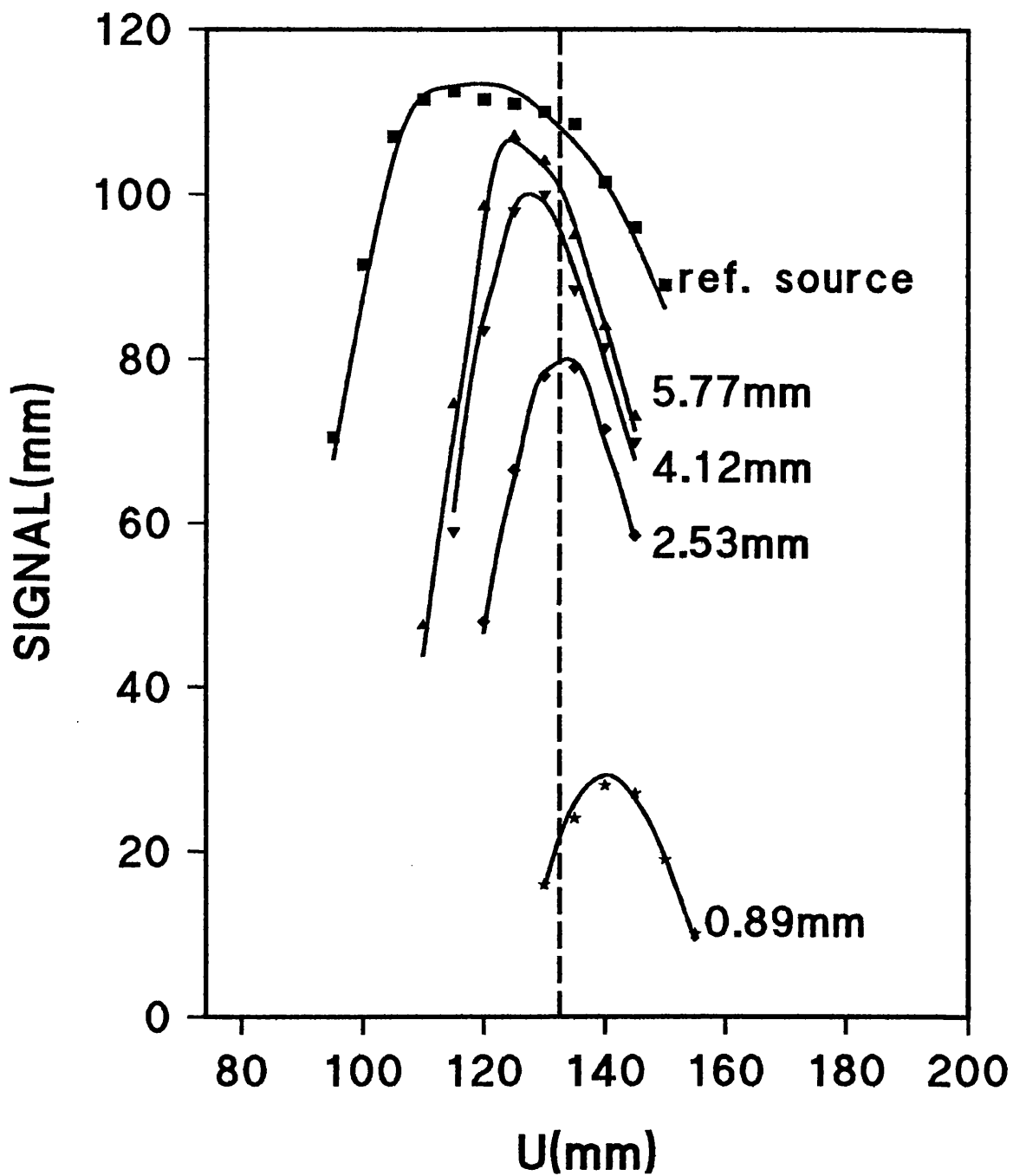


Fig. 4.21: Depth of field (I)

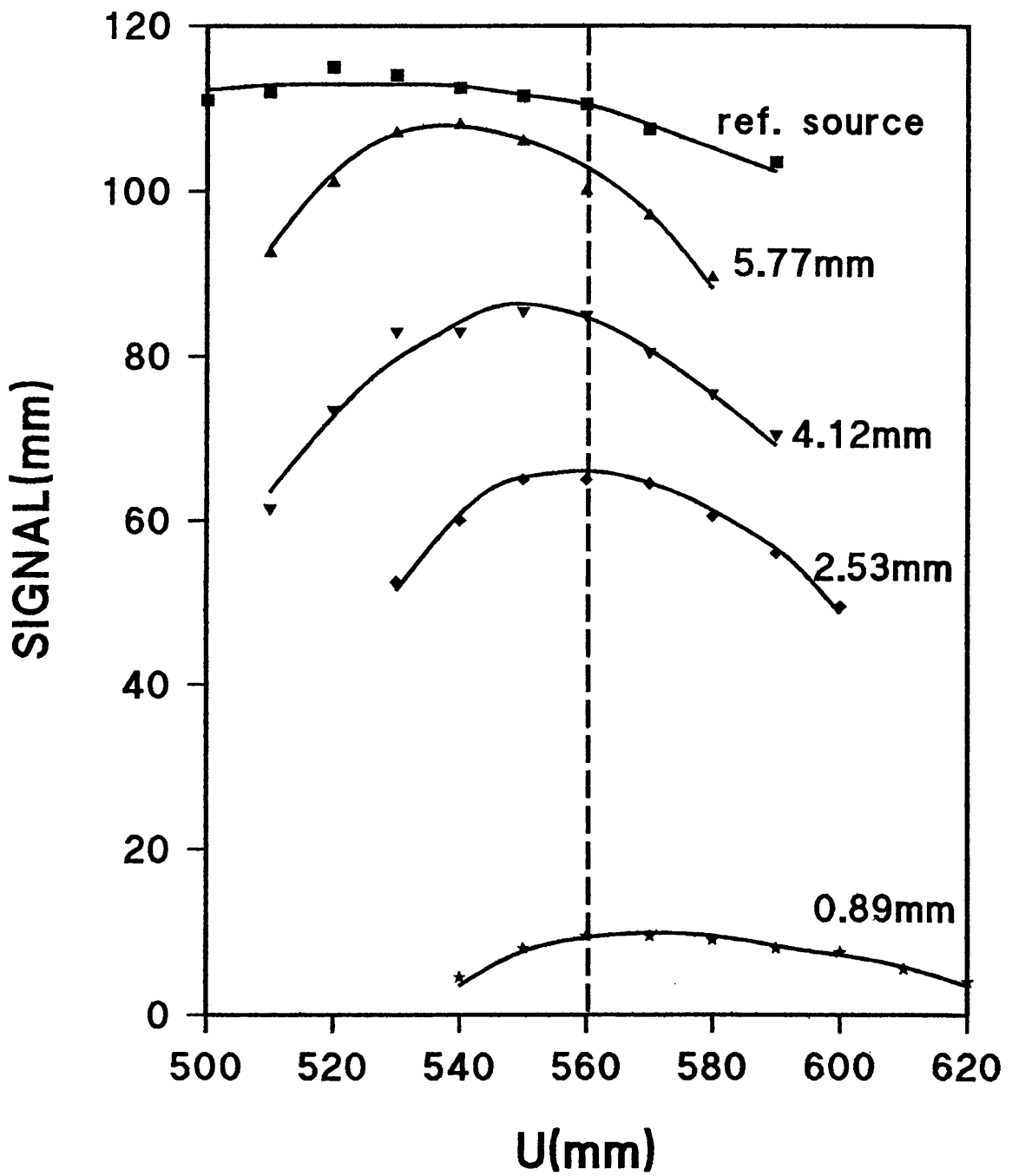


Fig. 4.22: Depth of field(II)

As U increases further, dv/du approaches 0 but even at 500 mm the gradient is virtually negligible. It is a straight forward matter now to compute a minimum object distance if the required rate of change of image distance with respect to object distance is known.

The second feature worth noting in Figs. 4.21 and 4.22 is that the object distance giving rise to the maximum output signal is a function of source width for relatively small object distances. This may be a consequence of the fact that Eq. 4.2 was derived for paraxial rays and at an object distance of 133 mm the paraxial approximation is no longer valid. It would be expected, then, that this could introduce greater errors at 133 mm compared with the errors introduced at 560 mm.

This is not apparent from Figs. 4.10 - 4.13 and to within experimental accuracy it can be assumed that the measured temperature is independent of object distance. However, it should be noted that if a large depth of field is required then an object distance of the order of 500 mm would be required.

4.4(v): Curvature

Although it has been concluded in section 3.5 (ii) that the emissivity of tissue is close enough to unity to allow accurate temperature measurements to be made, this relates only to tissue whose surface is viewed at normal incidence. However, Watmough et al. [70] have shown theoretically that the

emissivity falls as a function of viewing angle. This was measured experimentally using the set-up shown in Fig. 4.3.

The tissue was held with a fixed clamp at one end and a free clamp at the other. The weight of this free clamp created a small amount of tension in the tissue which would be expected in vivo. The laser was set at a fixed power level and a shutter was opened for a fixed time interval. For each measurement the laser was held at the same distance from the tissue and so, in theory, these identical conditions should lead to an identical temperature rise in the tissue. This was found to be true to an accuracy of ± 1 °C by observing the temperature rise in tissue under identical conditions.

The imager was then set up to measure the temperature of the tissue for various angles to the normal. The results are shown in Fig. 4.23. Also shown are Watmoughs theoretical results for a material with emissivity of 0.98 and the results obtained by applying Lamberts cosine law to the measurement at normal incidence. It must be noted, however, that Watmoughs results are not directly comparable to the other two sets of results and are presented on the same graph merely to show its general shape. The reason for this is that Watmoughs results are presented as absolute values of ΔT , whereas the other two sets of results depend on the temperature range set on the imager. By setting a smaller temperature range by means of adjustment of the gain and black level, the other two curves approach Watmoughs.

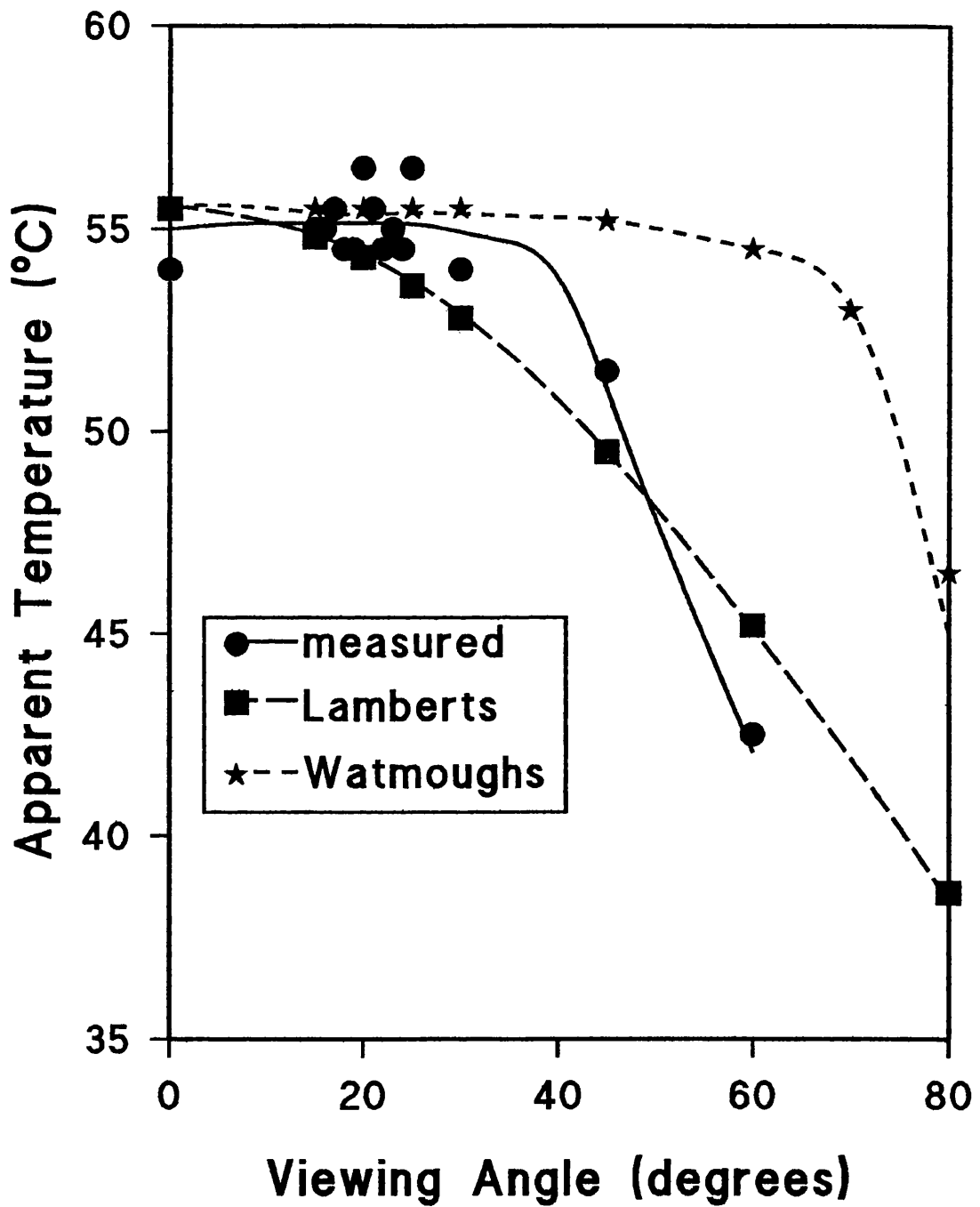


Fig. 4.23: Effect of Curvature on measured temperatures

Watmoughs results were based on consideration of the variation in reflection co-efficient at an air-to-dielectric interface whereas Lamberts cosine law is a consequence of the fact that the projected area normal to the direction of emission has a cosine dependence. The latter is in approximate agreement with the experimental results up to an angle of 60° .

The important point to note, however, is not how closely the theoretical results agree with the experimental results but at what angle does the fall in emissivity become significant.

Fig. 4.23 shows that viewing tissue at angles of greater than 30° results in a progressively greater underestimation of temperature. All measurements taken throughout this project were taken at normal incidence. However, the LAVA experiments described in Chapters 1 and 2 will be subject to errors from this source in addition to the errors introduced by the spatial resolution problem. It is clear, then, that if precise temperature estimates are required then for arteries with diameters comparable to or smaller than the laser spot size, an additional correction would be required in the computer model that is developed in Chapters 6 and 7

Fig. 4.24 illustrates this effect and although the sketch is not quantitative, it is clear that the effect is minimal in comparison with the spatial resolution problem. For this reason correction for curvature was not introduced into the model.

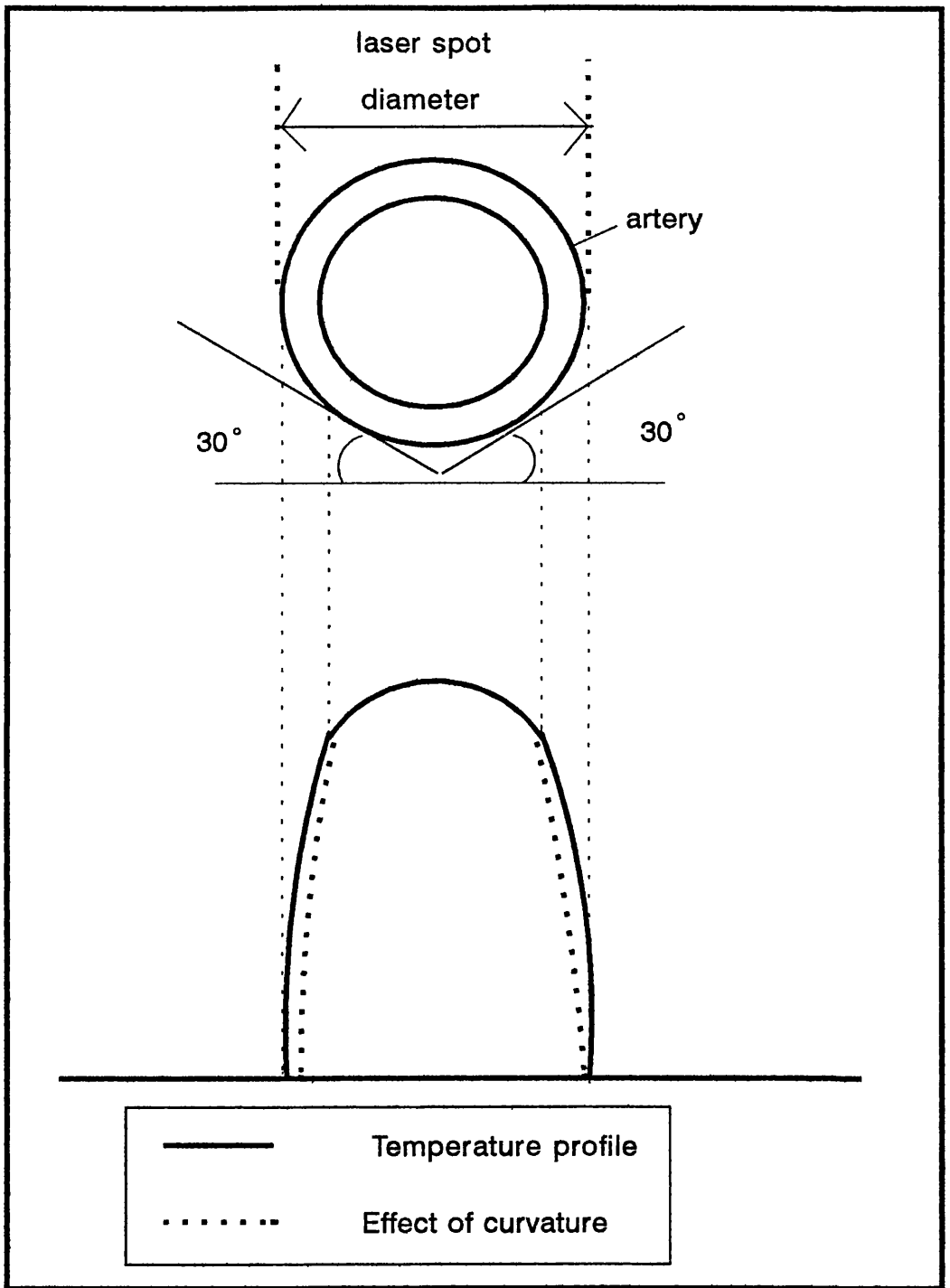


Fig. 4.24: Effect of curvature on measured temperatures (II)

CHAPTER 5:

TEMPERATURE MEASURING TECHNIQUES FOR THE CORROBORATION OF THE COMPUTER MODEL

5.1: INTRODUCTION

In Chapters 6 and 7 a computational model will be devised which, using a combination of theory and experimental results, will estimate the actual temperatures reached by biological tissue when irradiated with laser energy. In this context, true temperatures signify temperatures which have been predicted once the effect of the point spread function (PSF) have been taken into account. As will be shown in these Chapters, "true" by no means implies absolute accuracy and various correction factors, based on experimental results, are required to take into account the difficulties encountered in attempting to set up a working computer model. The

correction factors themselves are subject to experimental inaccuracies but these and other contributions to measurement errors will be considered in more detail in the following chapters.

Noting that the computer predictions are based to some extent on uncertain information and assumptions, it was therefore necessary to find another means of temperature measurement in order to corroborate the temperatures predicted by the model. A non-tactile method was sought in order to avoid interfering with the absorption of the laser energy and the emission of infrared radiation. However, a number of authors [72, 76] have employed micro-thermocouples to measure the temperature of tissue irradiated by lasers, having assumed that the thermocouple has a negligible effect on the process. In section 5.2 this assumption is investigated.

Two other methods were also investigated. The first, utilising differential scanning calorimetry (dsc), is described in detail in section 5.3. The second method involves staining the irradiated sample with picosirius red dye and then viewing it under a microscope with polarised light. This gives information on the temperature reached by the tissue and it will be described fully in section 5.4.

Both of these methods rely on knowledge of the denaturation temperature of the tissue under investigation and although this has been

estimated by other workers, it was determined independently due to its importance.

5.2: MICRO-THERMOCOUPLES

Micro-thermocouples have used to measure the temperature of tissue irradiated with laser energy [72, 76]. This should provide reliable measurements of temperature assuming good thermal contact is made and that the thermocouple is allowed to come into thermal equilibrium with the material. Even if this was the case for biological tissue, the thermocouples, or a series of thermocouples, would be inadequate to map tissue temperatures to the degree which was required for this project.

However, it was considered to be worthwhile to investigate the possibility of using it as a comparison to the thermal imager and, if successful, to use it as a guide to the accuracy of the computer model.

The micro-thermocouples were embedded in a biological phantom consisting of an Agar solution mixed with the dye, Fuchsin, which acted as a chromophore. The phantom was lased at different power levels and the apparent temperature (T_{app}) was compared with the temperature as measured by the thermocouple.

Before this comparison, a few preliminary experiments were carried out to assess the effect of the thermocouple on the repeatability of the results. Firstly, for identical experimental conditions, T_{app} was measured with and

without the thermocouple embedded in the phantom. It was found that, on average, T_{app} without the thermocouple was 2 °C greater than T_{app} with the thermocouple. This could be due to differences in absorption and/or conduction characteristics due to the presence of the thermocouple. This is not a problem as the changes introduced by the thermocouple would affect the measurement of temperature by thermocouple and thermal imager equally.

Another possibility was that the thermocouple was affecting the radiating properties of the material by disrupting the radiating surface layer. This proved to be the greatest problem involved because (as shown in section 3.5(ii)) the majority of the emitted energy originates in a 10 μ m thick surface layer. The aim would be to position the thermocouple as close to this layer as possible without disrupting the surface. It is obvious that this degree of precision would not be attainable on a regular basis. However, heat conduction will lessen the thermal gradient at the surface and may allow meaningful measurements to be made just below the surface. Table 5.1 shows the repeatability of this procedure.

Table 5.1: Repeatability of micro-thermocouple measurements

GROUP A (°C)	GROUP B (°C)
45.2	66.9
48.7	62.9
45.5	48.3
51.8	53.5
46.5	72.4

Group A gives the results for the Agar solution lased for a period of 20 s. The mean and standard deviation are 47.5 (± 2.7) °C. The Agar solution was lased for 30 s in Group B, giving 60.8 (± 10) °C. It is apparent that the positioning of the thermocouple is crucial to achieving a satisfactory degree of precision although, by repeating the measurements, the accuracy can be improved.

The temperatures as measured by the imager are compared with those measured by the thermocouple in Fig. 5.1. The solid line indicates agreement between the two and the dashed line is the line of best fit. The graphs suggest agreement between the two, but as we know that the imager is underestimating the temperature then the same conclusion must be drawn about the thermocouple.

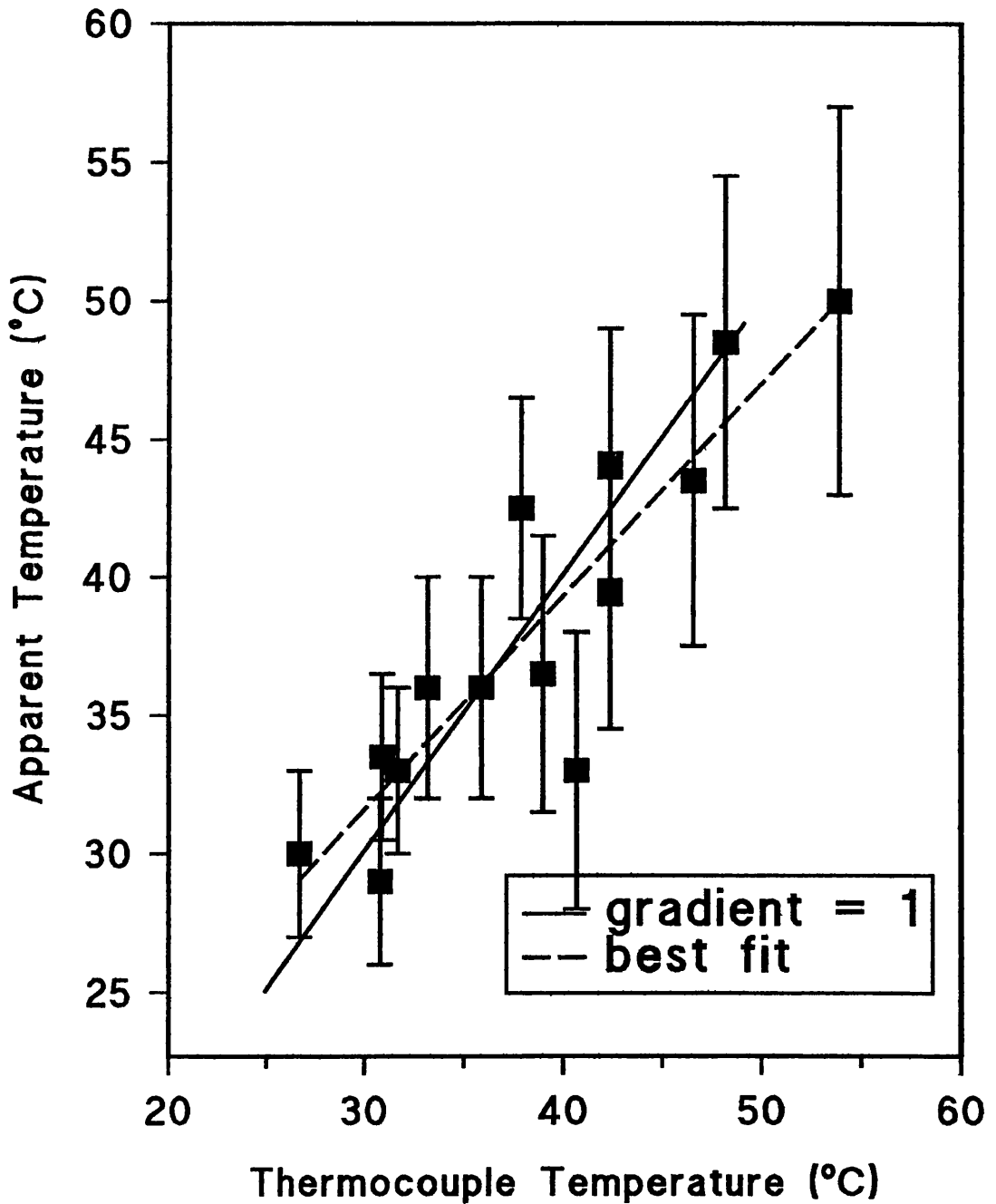


Fig. 5.1:Temperature measurements thermocouple compared with thermal imager

This does not rule out the use of thermocouples as tissue temperature measuring devices but it does show their limitations.

Firstly, they only record the temperature over a very small volume, which will not necessarily be the maximum temperature over the region of interest and, secondly, good thermal contact and thermal equilibrium must be achieved. This would be possible only in a relatively stable environment and this condition does not necessarily apply at the surface of a phantom irradiated by laser energy.

5.3: DIFFERENTIAL SCANNING CALORIMETRY (DSC)

5.3(i): Principles of the technique

DSC is a technique for measuring transition temperatures in materials, in this case using a 910 Differential Scanning Calorimeter and a 990 Thermal Analyzer (DuPont Instruments). A biological sample and a reference material are placed in separate, hermetically sealed, aluminium pans which are maintained at the same temperature. The temperature is uniformly increased and the differential heat flow between the two samples is measured by thermocouples. This heat flow will, of course, be zero for identical substances but for dissimilar substances, any exothermic or endothermic reaction will cause the sample under analyses to lead or lag the reference temperature. When the transition temperature is reached, the heat energy

applied to the sample is used in denaturing the tissue and hence, the reference temperature increases as the sample temperature remains fixed. The heat flow between the two samples is monitored by the thermal analyzer and an example of the graph obtained by this method is shown in Fig. 5.2.

It has been shown [77] that the area under this curve is proportional to the sample weight which is to be expected as heavier samples have more material to denature and there is a correspondingly greater heat flow between the two materials. However, if the material was partially denatured then it is to be expected that the area under the peak would be correspondingly smaller and similarly if the material was fully denatured then the peak would not appear at all. This principle was used to determine whether or not the denaturation temperature had been reached and the decrease in area used as an approximate guide as to how far above this temperature the sample had been heated. This could then be compared with the apparent temperatures as measured by the imager.

5.3(ii): Experimental set-up and results

The set-up is shown in Fig. 4.22 in the previous chapter, where the effect of the imagers viewing angle was considered. In this case, however, the angle was not varied and was set at approximately 20° . The results of section 4.4(vi) show that this angle makes a negligible difference to the

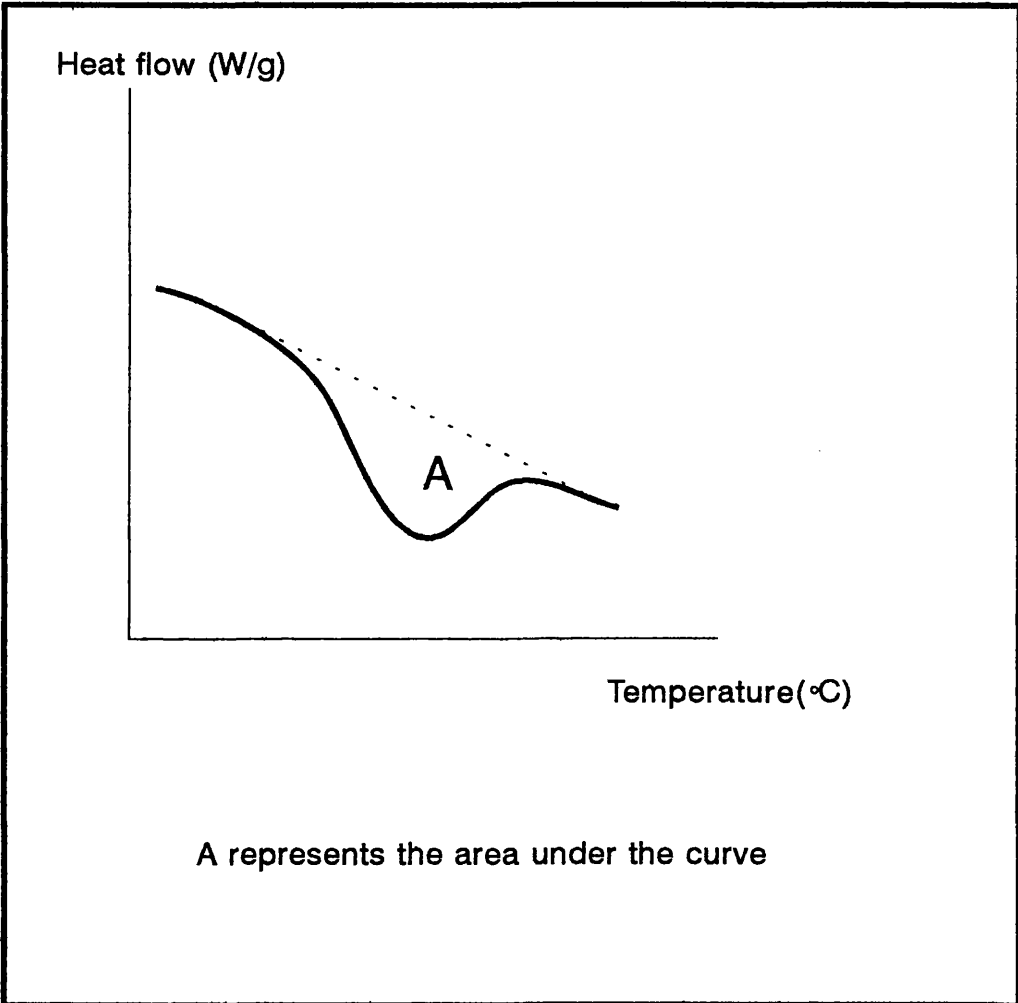


Fig. 5.2:Example of DSC analysis

measured temperature. The material chosen for the experiment was bovine pericardium because it was readily available from the local abattoir and its denaturation temperature had been ascertained [78, 79]. The results of our own investigations into the denaturation temperature are given in section 5.4.

Firstly, the experiment of McClain [77] was repeated in order to confirm that the relationship between the area under the curve and tissue weight applies to our experimental set-up and equipment. In this case, the tissue thickness was measured instead of the tissue weight and as equal diameter samples are cut to fit into the d.s.c. pan, this should be proportional to tissue weight. This does introduce more errors into the experiment but it was considered to be good enough to at least show whether or not this approach was worth pursuing. Fig. 5.3 shows the results.

The error bars were obtained by successively measuring the area under the curve obtained from different samples of the same thickness. The bars represent the standard deviation and the mean of these values are shown at 400 μm . It is clear that although the linear relationship holds (at least approximately), a great deal more accuracy would be required if this method was to be used in the corroboration of the computer model.

The second part of the experiment used the set-up shown in Fig. 4.3. It involved lasing a series of equal thickness tissue samples to a pre-defined apparent temperature. They were then analysed using the d.s.c. technique

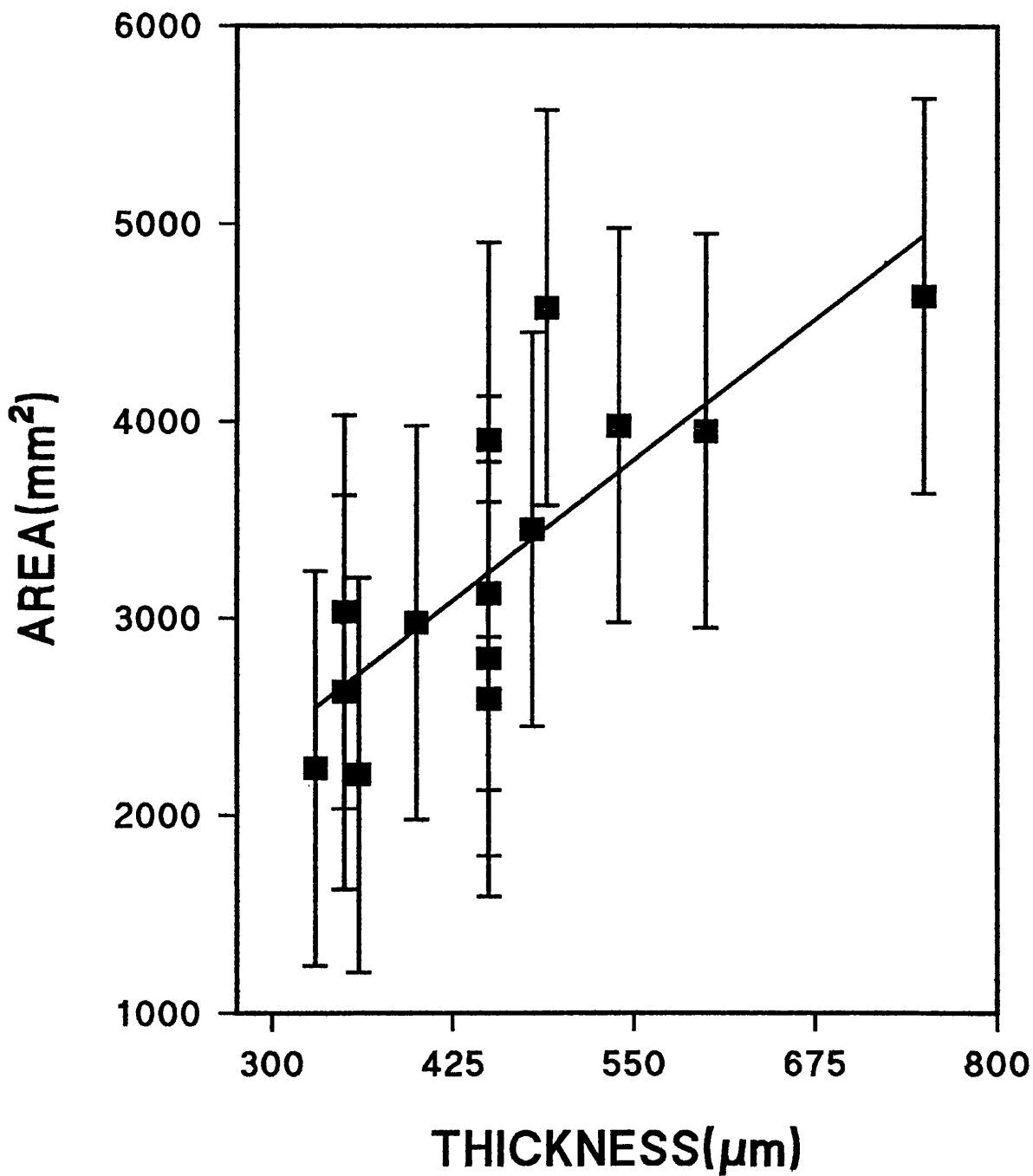


Fig. 5.3: D.S.C.:— Area under curve versus sample thickness

and a graph of area under the curve against apparent temperature is shown in shown in Fig. 5.4. It indicates that denaturation begins at the apparent temperature of 49 - 50 °C as opposed to the measured value of 62 °C. However, the curve drawn through the points merely reflects our preconceived idea of how it should look. The error bars are so large that a straight line can be made to pass through the majority of points.

In principle, then, this method could be used to assess the accuracy of the computer model. However, major efforts would be required in order to reduce the errors involved. Therefore, another method which allows the direct visualisation and quantification of the denatured volume was pursued. This technique is described in the following section.

5.4: TISSUE STAINING WITH PICROSIRIUS RED

5.4 (i): Principles of the technique

The dye, picosirius red, was first proposed to demonstrate the existence of the collagen protein in tissue by L. C. U. Junqueira et al. [80]. The picosirius molecules attach themselves to the collagen fibres in such a way that their axes are parallel. This results in an enhanced birefringency and the collagen appears with a characteristic red colour when viewed under a microscope with polarised light. However, denatured collagen does not exhibit birefringence and appears as a blackened area (see Fig. 5.5, for

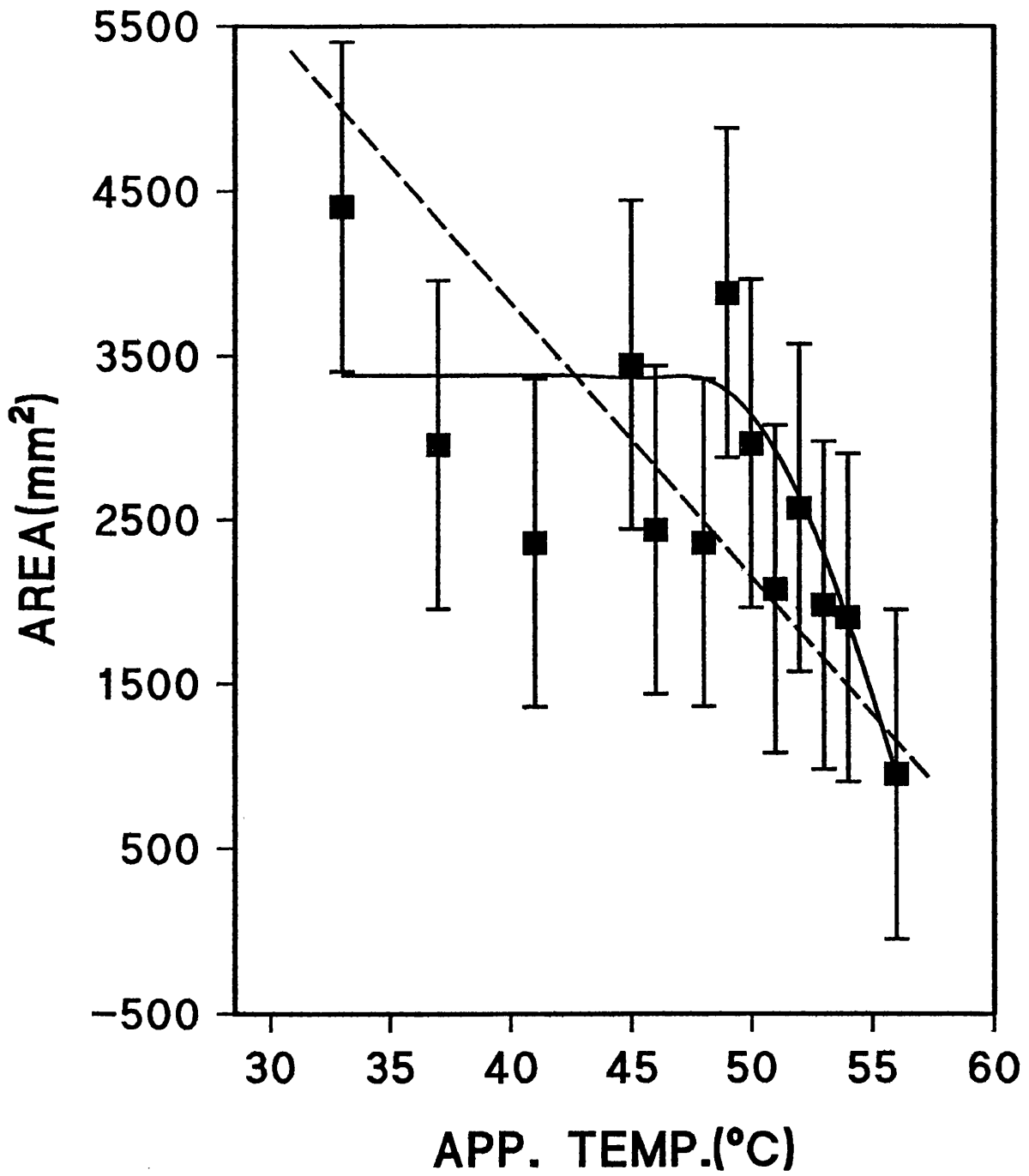


Fig. 5.4: D.S.C. results

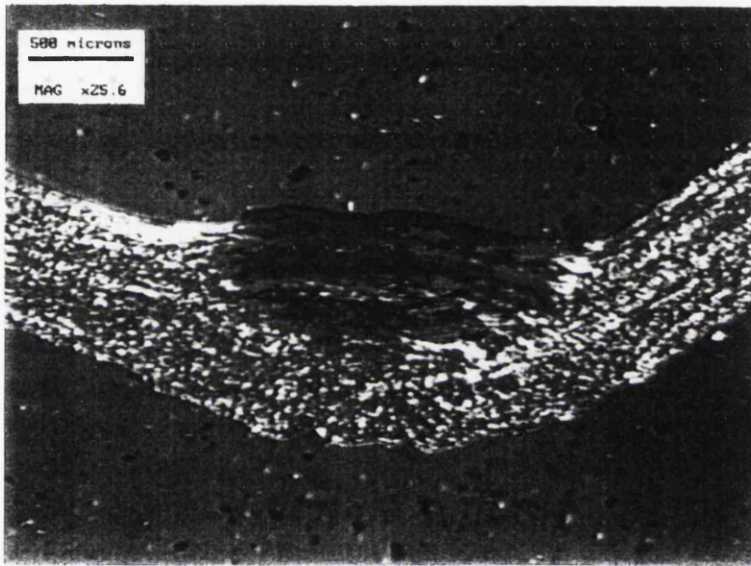


Fig. 5.5: Example of picrosirius red staining technique

example). This area is clearly demarcated and has been used as a marker for thermal damage in tissue [81].

It can, therefore, be used to demonstrate that the tissue under analysis has or has not reached the denaturation temperature. This temperature has been found to be $63 (\pm 0.5) ^\circ\text{C}$ (see previous section), although the approach taken here does not depend on the accuracy of this result.

The approach adopted here was to find the temperature at which the tissue becomes optically inactive, i.e. when the tissue appears blackened when viewed with polarised light. This temperature was found by immersing the tissue in a water bath with saline solution at a well defined temperature. This process was repeated for a range of temperatures around the denaturation temperature.

The time taken for the tissue to reach equilibrium was found

$$t = \frac{\rho \cdot c \cdot x^2}{k} \text{ ---- (5.1)}$$

where t is the time taken, ρ is the density, c the specific heat, k the thermal conductivity and x the thickness of the tissue sample. This can be applied approximately though it will overestimate the time required as it assumes heat flow from one direction only, whereas in the experiment described, the tissue is heated from all directions. The equation is derived in the appendix.

For biological tissue, $\rho \approx 1000 \text{ kg m}^{-3}$, $c \approx 3000 \text{ J kg}^{-1} \text{ K}^{-1}$ and $k \approx 0.4 \text{ W m}^{-1} \text{ K}^{-1}$ [82]. The tissue thickness is approximately 1 mm, hence $t \approx 7.5 \text{ s}$. So the tissue sections were submerged for 10 s to ensure that thermal equilibrium had been reached.

The specimen was then fixed in formalin, sliced into 10 μm sections and stained with picosirius red. It was then ready to be viewed under the microscope, where the known temperature reached by the tissue was compared with its appearance, i.e. black or red.

5.4 (ii): Results

Fig. 5.6 shows some examples of the stained tissue after being heated to temperatures from 64 - 67 $^{\circ}\text{C}$. There is a clear transition between 65 and 66 $^{\circ}\text{C}$ showing that the tissue becomes optically inactive at 65.5 (± 0.5 $^{\circ}\text{C}$). The experiment was repeated and the second set of experiments were found to be consistent with the first.

The transition temperature measured here is approximately 3 $^{\circ}\text{C}$ higher than other studies which used different methodologies, though it must be stressed that it is irrelevant to the work carried out here, whether or not this corresponds to the denaturation temperature. All that need concern us is that the tissue becomes optically inactive at this temperature. It can now be used as a direct comparison for the computational model.

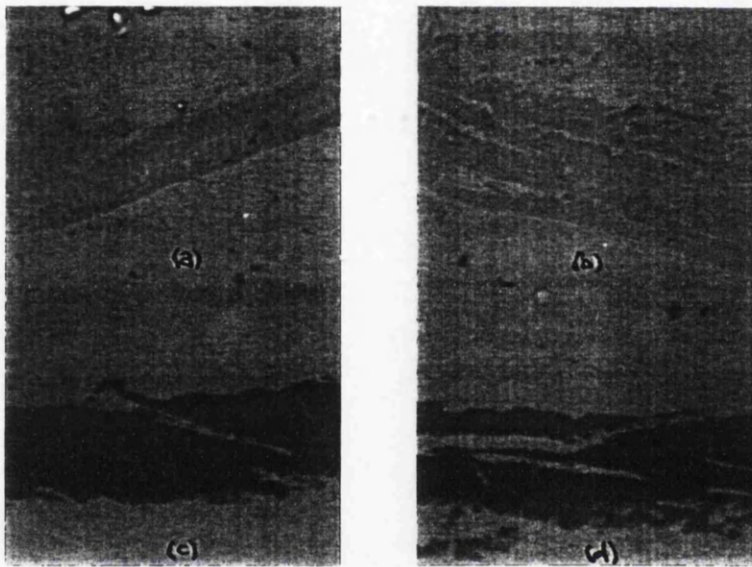


Fig. 5.6: Stained tissue samples
heated to (a) 64°C; (b) 65 °C;
(c) 66 °C; (d) 67 °C as viewed with
polarised light

5.5: CONCLUSION

Of the three techniques investigated here, two were found to be inadequate for our purposes.

Micro-thermocouples are too disruptive and radically change the environment of the material under investigation. As a consequence, the estimated temperatures are approximately equal to those measured by the thermal imager. As this is known to be an underestimation, it must also apply to the micro-thermocouple.

In principle, the DSC technique should allow us to determine whether or not the denaturation temperature has been reached. However, analysis of the results shows it to be a very inaccurate method and, hence, unsuitable for our purposes.

Finally, the picrosirius red staining technique allows us to state precisely, whether or not the transition temperature has been reached. This will allow a comparison of the model at this temperature.

CHAPTER 6:

COMPUTER MODELLING (I): CONVOLUTION AND THE POINT SPREAD FUNCTION

6.1: INTRODUCTION

The point spread function (PSF; also called the point source response function) has been referred to in a rather general, unquantitative manner in previous Chapters (see 3.5(iii) and 4.4(i)). The aim of this Chapter is to define the term precisely and show how it relates to the problem of accurately measuring the temperatures of small heat sources (sections 6.2 and 6.3).

The PSF of the PEV is then found by two independent experiments in section 6.4 and the factors which may affect it are investigated in 6.5. These investigations determine what approximations can be justified in order to simplify the mathematical analysis.

6.2: MATHEMATICAL DESCRIPTION

The equations derived in this section are of the most general nature. That is, they can be applied to any system that images electromagnetic radiation, e.g. the gamma camera which images a radionuclide distribution or an ordinary camera which images a light intensity distribution. These modalities require additional care as the 3-dimensional radionuclide / light intensity distribution as imaged as a 2-dimensional distribution. However, this problem does not arise when imaging the thermal radiation emitted by biological tissue as approximately 2/3 of the radiation is emitted in the first 10 μm of tissue. It can, therefore, be taken to be a 2-dimensional infrared source to a high degree of accuracy.

Conventionally, the object distribution is denoted by $f(\alpha, \beta)$ and the image distribution by $g(x, y)$ and in general there is no 1:1 relationship between a point in object space (α_i, β_i) and a point in image space (x_i, y_i) . Fortunately, however, the greatest part of the radiation absorbed at (x_i, y_i) will have been emitted from some corresponding point (α_i, β_i) , with the contribution at (x_i, y_i) becoming smaller as we move further away from (α_i, β_i) .

If this spatial dependence of the relative contribution can be described by a function, say $h(\alpha, \beta, x, y)$, then for a particular image distribution, $g_1(x, y)$ in which the object is non-zero only at (α_1, β_1) ,

$$g_1(x, y) = h(x, y, \alpha_1, \beta_1, f_1(\alpha_1, \beta_1)) \text{ ---- (6.1)}$$

$h(x, y, \alpha_1, \beta_1, f_1(\alpha_1, \beta_1))$ is the generalised PSF and the equation can be visualised with the aid of Fig. 6.1. Fig. 6.1(a) represents an infrared distribution in object space (effectively a point source) and Fig. 6.1(b) represents the corresponding distribution in image space. Equation 6.1 is not very helpful as it stands and some simplifications are required.

Firstly, it describes a non-linear system. That is, if another signal, say f_2 , arising from the same position (α_1, β_1) were added to f_1 , it would not be equal to the simple addition of separate images, $g_1 + g_2$. Mathematically, g_1 is described by equation 6.1. Similarly, g_2 can be described by

$$g_2(x, y) = h(x, y, \alpha_1, \beta_1, f_2(\alpha_1, \beta_1)) \text{ ----(6.2)}$$

Then, by combining Equations 6.1 and 6.2

$$g_1(x, y) + g_2(x, y) = h(x, y, \alpha_1, \beta_1, f_1(\alpha_1, \beta_1)) + h(x, y, \alpha_1, \beta_1, f_2(\alpha_1, \beta_1)) \text{ ---- (6.3)}$$

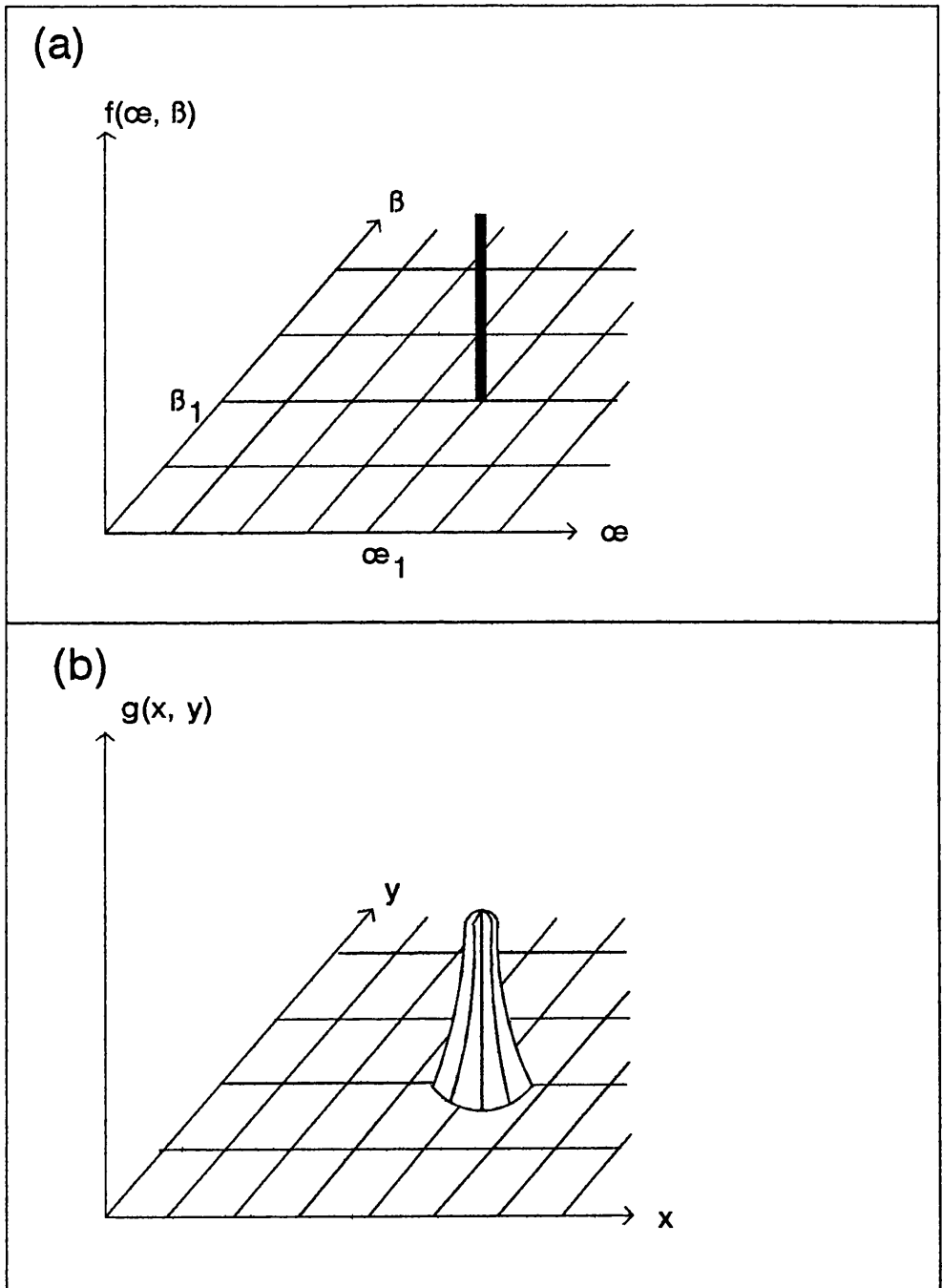


Fig. 6.1: Visualisation of the generalised convolution equation

This is a non-linear superposition and leads to virtually intractable calculations. If, however, the system is linear, then Equation 6.1 becomes

$$g_1(x, y) = h(x, y, \alpha_1, \beta_1) f_1(\alpha_1, \beta_1) \text{ ---- (6.4)}$$

and Equation 6.3 becomes

$$g_1(x, y) + g_2(x, y) = h(x, y, \alpha_1, \beta_1) [f_1(\alpha_1, \beta_1) + f_2(\alpha_2, \beta_2)] \text{ ----}$$

(6.5)

Eq. 6.4 assumes that the function, h , is not dependent on the magnitude of the signal and its validity will be investigated in section 6.5.

The less general forms of Eq.'s 6.1 and 6.2, described in Eq. 6.4, takes account of the fact that the response over the target may not be uniform, by the explicit dependence of h on α_1 and β_1 .

However, attempting to take these variations into account would provide needless difficulties and all measurements were confined to the central portion of the imager. As we are attempting to measure the temperature of very small heat sources, this restriction does not present a problem.

In this case h is dependent only on the difference on the corresponding points on the object and image plane, $(x - \alpha_1, y - \beta_1)$. This can be visualised more readily by considering the object and image planes to be coincident or the object distribution to be equivalent to the ideal image distribution. The

image dimensions then have to be normalised such that the magnification is unity. The justification for this is presented in section 6.5 where the effect of magnification is investigated.

Eq. 6.4 can now be written as

$$g_i(x, y) = h(x - \alpha_1, y - \beta_1) f_i(\alpha_1, \beta_1) \text{ ---- (6.6)}$$

Now, the object can be considered to be composed of an array of these sources at (α_1, β_1) , (α_2, β_1) , -----, (α_1, β_2) , (α_2, β_2) , -----, (α_m, β_n) , each with its own intensity, f_i , but subject to the same effect by the PSF, h . Now, assuming h to be an integrable function any image distribution can be described by integrating the weighted PSF over the whole of object space or, in other words, by convolving the object distribution with the PSF.

Mathematically, this procedure is described thus

$$g(x, y) = \iint h(x - \alpha, y - \beta) f(\alpha, \beta) d\alpha d\beta \text{ ---- (6.7)}$$

This, then, describes how an object distribution is degraded in transmitting its information to the image plane. The problem taken up in Chapter 7 considers the inverse problem or deconvolution. That is, how to retrieve the undegraded or "true" object distribution from the degraded image. Firstly, though, we require a precise description of the PSF, $h(x - \alpha, y - \beta)$ relating specifically to the PEV.

6.3: APPLICATION TO THE MODEL

Before the determination of the PSF is described (see next section), a brief overview of the computational model will be given. It is based on the principal result of the previous section, Eq. 6.7, with two further modifications.

Firstly, section 4.4(i)(b) showed that spatial resolution was independent of detector orientation which justifies the rotational symmetry implicitly assumed in Fig. 6.1(b). Then, as the x and y axes are identical, Eq. 6.7 can be reduced to 1 dimension, with the results obtained for one axis being immediately applicable to the other axis. Eq. 6.7 now becomes

$$g(x) = \int h(x - \alpha) f(\alpha) d\alpha \text{ ---- (6.8)}$$

The second modification involves replacing integration with summation. The two processes are identical if the curves are divided into a sufficient number of elements. In our case, this is limited by the number of pixels in the horizontal direction on the computer monitor, but it will be shown that this is entirely adequate. So, now, Eq. 6.8 becomes

$$g(x) = \sum_{\alpha=1}^n h(x - \alpha) f(\alpha) \text{ ---- (6.9)}$$

Let us now consider a simple example to illustrate how the model works. Fig. 6.2 should be helpful in visualising this where $g(x)$ and $f(\alpha)$ are

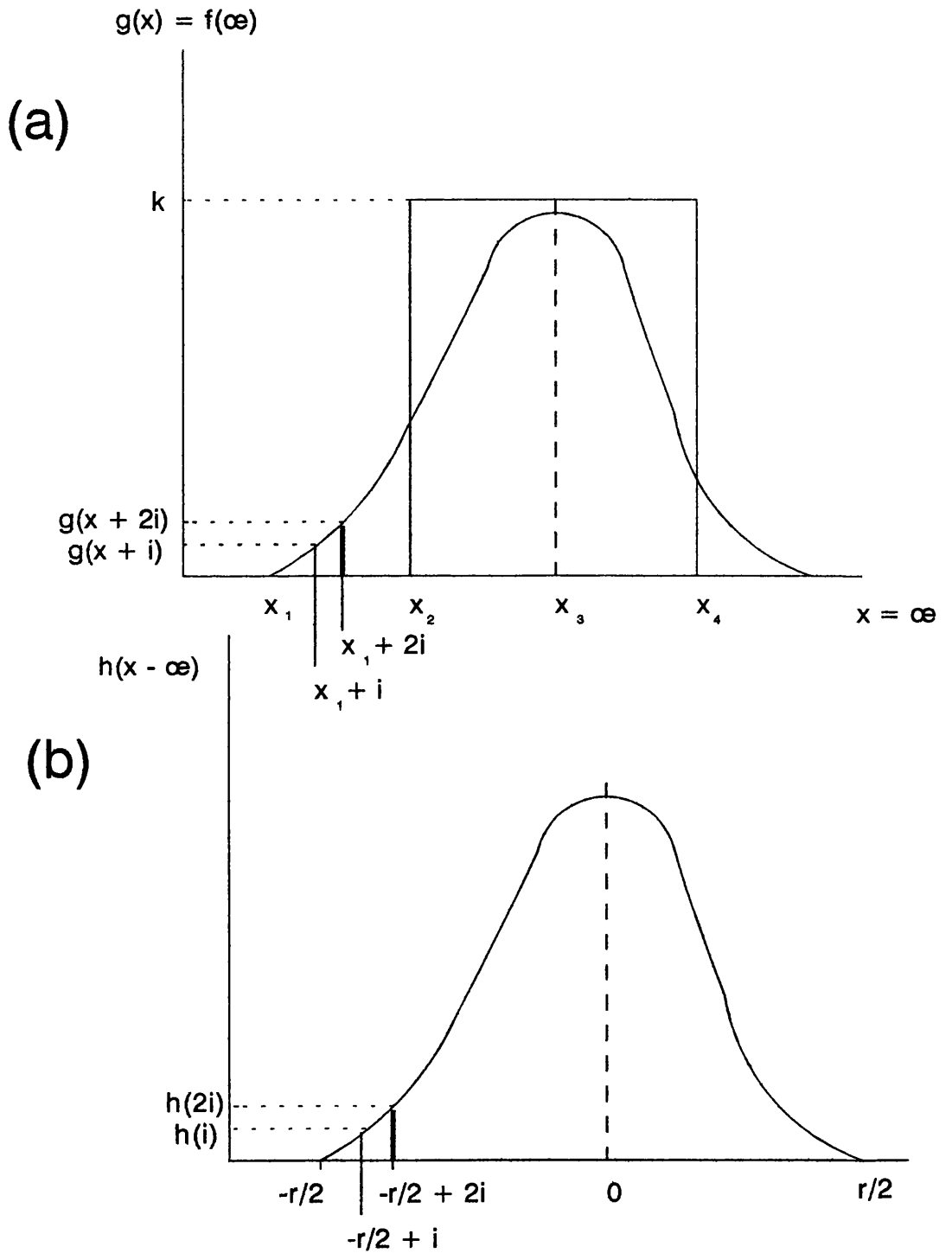


Fig 6.2: Visualisation of the Computational Model

considered to occupy the same space. $f(\alpha)$ is the object distribution that would be expected from the variable slit experiments, ie. $f(\alpha) = \text{constant} = k$ for $x_2 \leq \alpha \leq x_4$ and $f(\alpha) = 0$ for $\alpha < x_2$ or $\alpha > x_4$. The symbol, i , represents the increments of the summation of Eq. 6.9 and its magnitude is greatly exaggerated here in the interests of clarity. Eq. 6.9 now becomes

$$g(x) = k \sum_{\alpha=x_2}^{x_4} h(x - \alpha) \text{ ----- (6.10)}$$

Let us now assume that the PSF is known and is sketched in Fig. 6.2(b). Its range is from $-r/2$ to $r/2$, where r is the resolution of the imager. This is a consequence of the definition of r . If we want to know the value of $g(x)$ at an arbitrary point, say, $x = x_1 + 2i$, then

$$g(x_1 + 2i) = k [h(i) + h(2i)] \text{ ----- (6.11)}$$

where all the other terms in the summation are zero. For any point, x_1 , the summation runs from x_1 to $x_1 + r/2$ and the weighting factor is determined by the relative position on the curve $h(x - \alpha)$.

This approach will now be taken to determine the PSF in the next section.

6.4: DETERMINATION OF THE PSF

6.4(i): Computational model approach

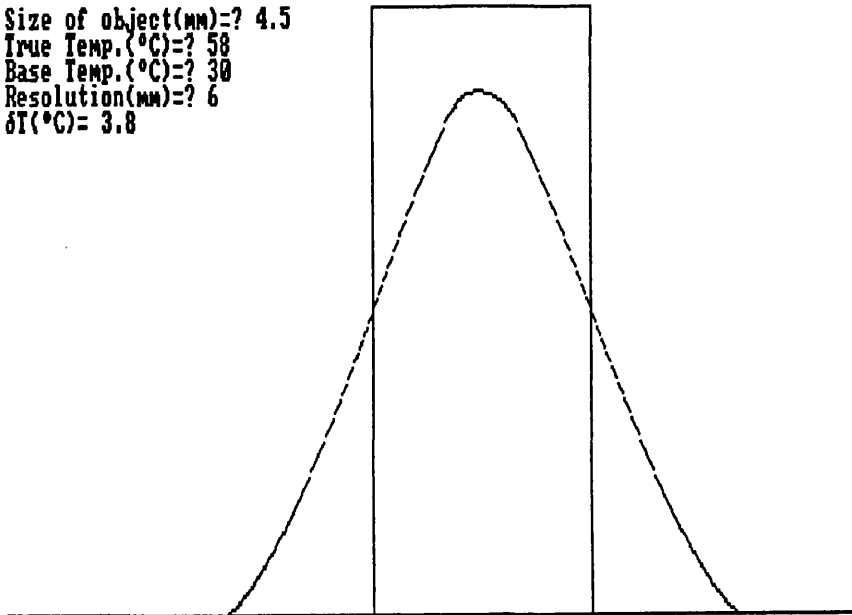
The computational work in this and the following chapter was carried out on a personal computer, using programs written specifically for this purpose in the Quick Basic language. Fig. 6.3 shows an example of the output for the prediction of the image distribution from knowledge of the object distribution. Each pixel (representing an image point) requires the summation of 200 numbers, which themselves are weighted according to their distance from the central point. This process, involving approximately 200 000 computations, takes approximately 10 seconds to carry out on a 486D/33 computer.

In this approach, we utilise the results of Figs. 4.10 - 4.13. For each point, $f(\alpha)$ and $g(x)$ are known precisely (not entirely true for $g(x)$; see section 6.5 (iii)) and the PSF or $h(x - \alpha)$, is the only unknown of Eq. 6.9 or 6.10. It can now be found by a process of trial and error.

Eq. 6.10 refers to one particular slit with a width of $x_1 - x_2$ but it can readily be applied to any slit width by altering the limits of the summation. So the program was extended to carry out the analysis for each slit width and ΔT was plotted for each as a function of slit width. This was then compared with the experimental curve.

BFIG63.BMP

Size of object(mm)=? 4.5
True Temp.(°C)=? 58
Base Temp.(°C)=? 30
Resolution(mm)=? 6
 $\delta T(^{\circ}\text{C})= 3.8$



Press any key to continue

Fig. 6.3: Computer output for the prediction of image distribution

To test the program, a simple triangular function was used for the PSF.

That is Eq. 6.10 became

$$g(x_3) = k \sum_{\alpha=x_3}^x C \left(1 - \left| \frac{x_3 - \alpha}{3} \right| \right) \text{---- (6.12)}$$

The denominator of the last term represents the resolution limit, that is, if $x - \alpha = 3$, then the contribution from that term will be zero.

It was not expected that the PSF would be triangular. However, the curve generated from this PSF is shown in Fig. 6.4 and it is quite a good approximation to the experimental curve.

A more realistic PSF would have a Gaussian shape. Eq. 6.10 would then be

$$g(x_3) = k \sum_{\alpha=x_3}^x C \exp \left(- \left| \frac{x_3 - \alpha}{A} \right|^2 \right) \text{---- (6.13)}$$

There are now two constants to be found, but a process of iteration brings about the rapid convergence of the theoretical curve with the experimental curve. They are shown in Fig. 6.5. Although this Gaussian curve gives good agreement with the experimental curve and is therefore a close approximation to the true PSF, it does not look realistic because of the discontinuity where the "tails" have been cut off (see Fig. 6.10). However,

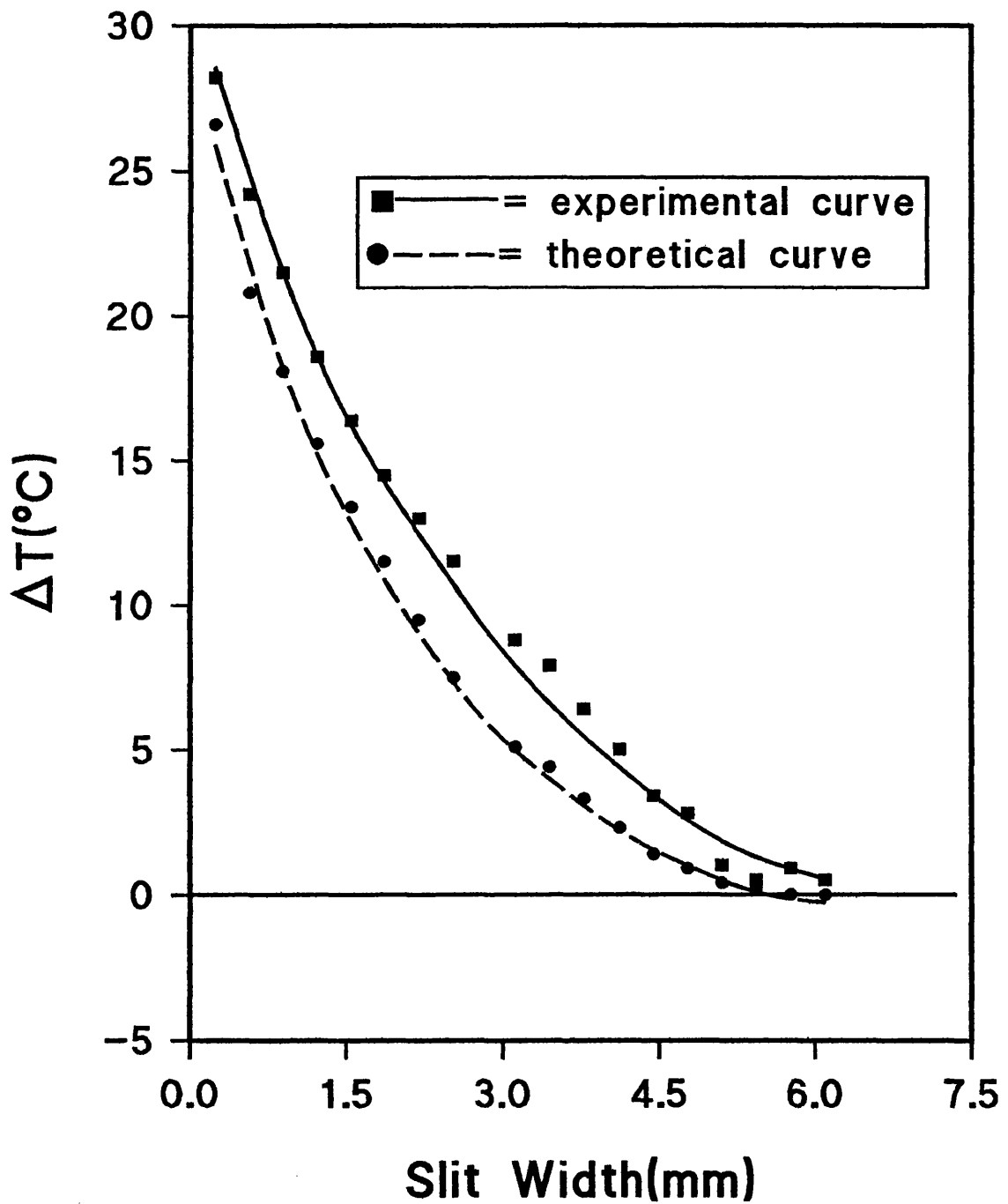
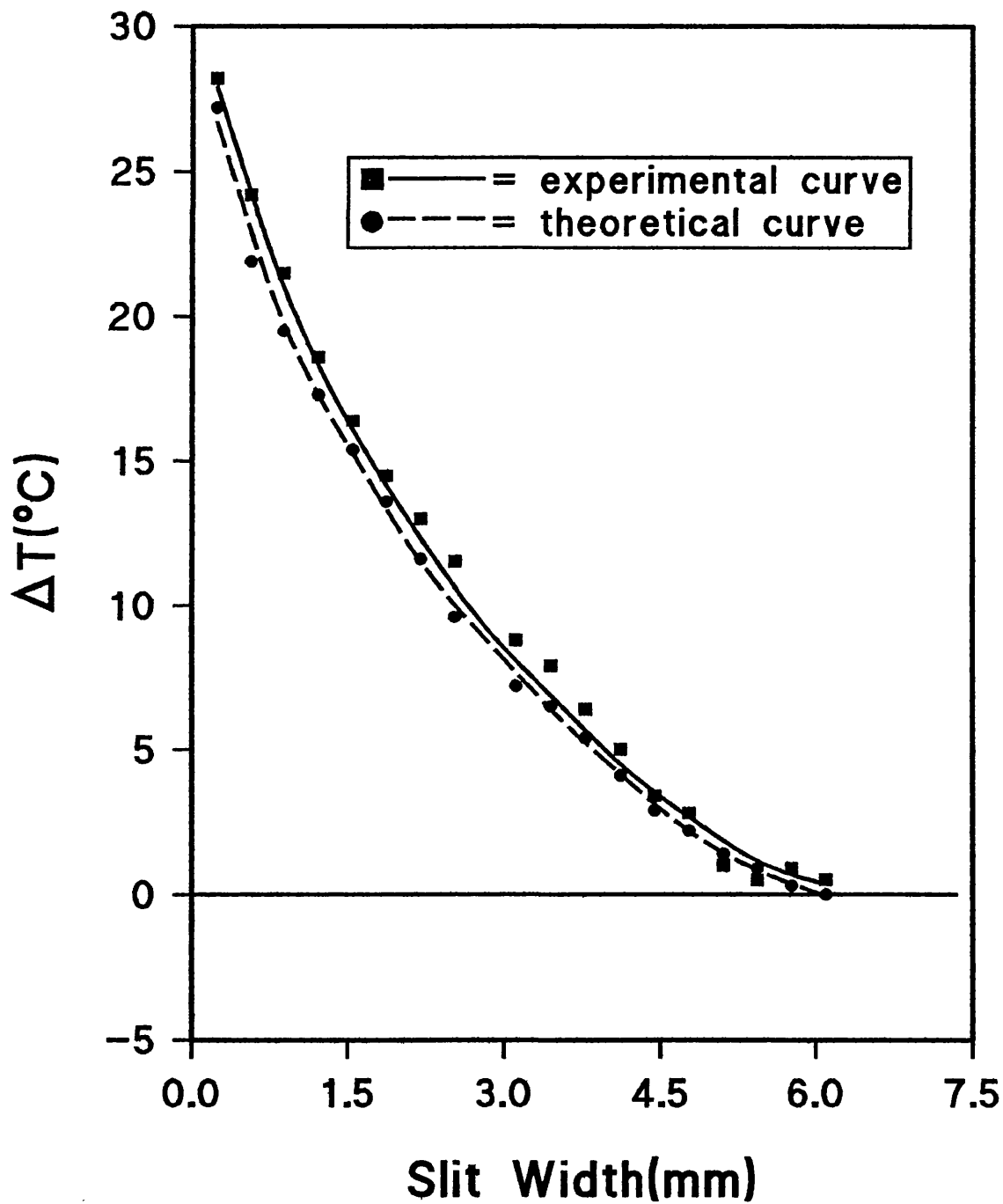


Fig 6.4: Computational model prediction of effect of triangular PSF



**Fig. 6.5: Computational model prediction
of effect of Gaussian PSF**

another approach can be taken which does not assume that the function is Gaussian and this method is described in the following section.

6.4 (ii): Edge spread function approach

The PSF can also be found by differentiating the image of a step function. This follows from the result

$$h_1(x) = \frac{\partial h_e(x)}{\partial x} \text{ ----- (6.14)}$$

where $h_1(x)$ is the line spread function (LSF) and $h_e(x)$ is the edge spread function (ESF). (For a rigorous derivation of this result, see ref. [83]).

Fig. 6.6 illustrates the relationship between the PSF and the LSF, that is, if we take a slice through the LSF in a direction perpendicular to the line, we obtain the 1-dimensional projection of the PSF. It should be noted, however, that the magnitudes will be different, though fortunately we only require to know the general shape of the function. Assuming circular symmetry, the PSF can now be found by rotation of the 1-dimensional projection through 360° . This assumption was justified earlier in section 4.4(i)(b), although it will not be necessary to perform this rotation as 1 dimension is sufficient for our purposes. Hence, if we differentiate the image on an edge in a direction perpendicular to the edge, we obtain a 1-dimensional representation of the PSF.

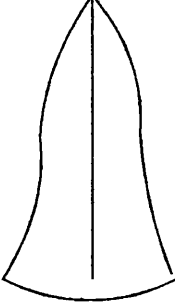
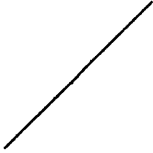
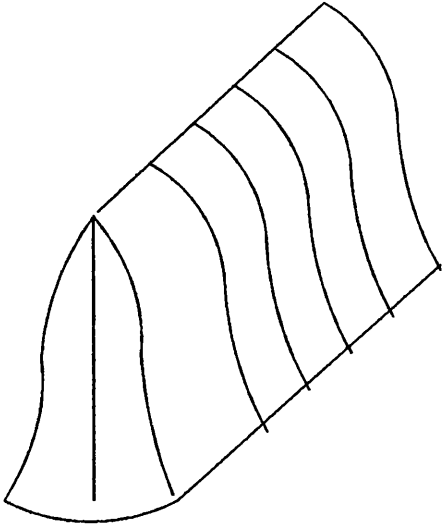
	source	image
PSF		
LSF		

Fig 6.6: Comparison of PSF and LSF

A qualitative justification for Eq. 6.14 can be given if we consider the ideal case. That is, in an ideal imager, a step function would be imaged as a step function, which when differentiated yields a δ function, which the PSF must be in an ideal imager.

It was a straightforward matter to find the ESF. The heat source was brought into focus and one of the plates used to form the slits was used to shield half of the source and provide a sharp temperature step to be imaged. The time base of the oscilloscope was adjusted so that the output signal across this edge could be recorded.

Now, we have already shown that the PSF is symmetrical, so to improve the accuracy of the measurement, one half of the PSF was rotated by 180° around the midpoint and the two half's were averaged. The results for a magnification, $M = 0.1$ and 0.2 are shown in Figs. 6.7 and 6.8, respectively and both curves are compared directly in Fig. 6.9. The results of a curve-fit are also shown. It was then a simple matter to differentiate this curve to find the PSF.

We now have two representations of the PSF and Fig. 6.10 compares them. There is very good agreement between the two curves and the theoretical curve of ΔT against source width for the PSF derived from the ESF is indistinguishable from the theoretical curve derived from the Gaussian shown in Fig. 6.5. However, as noted earlier, the discontinuity in the

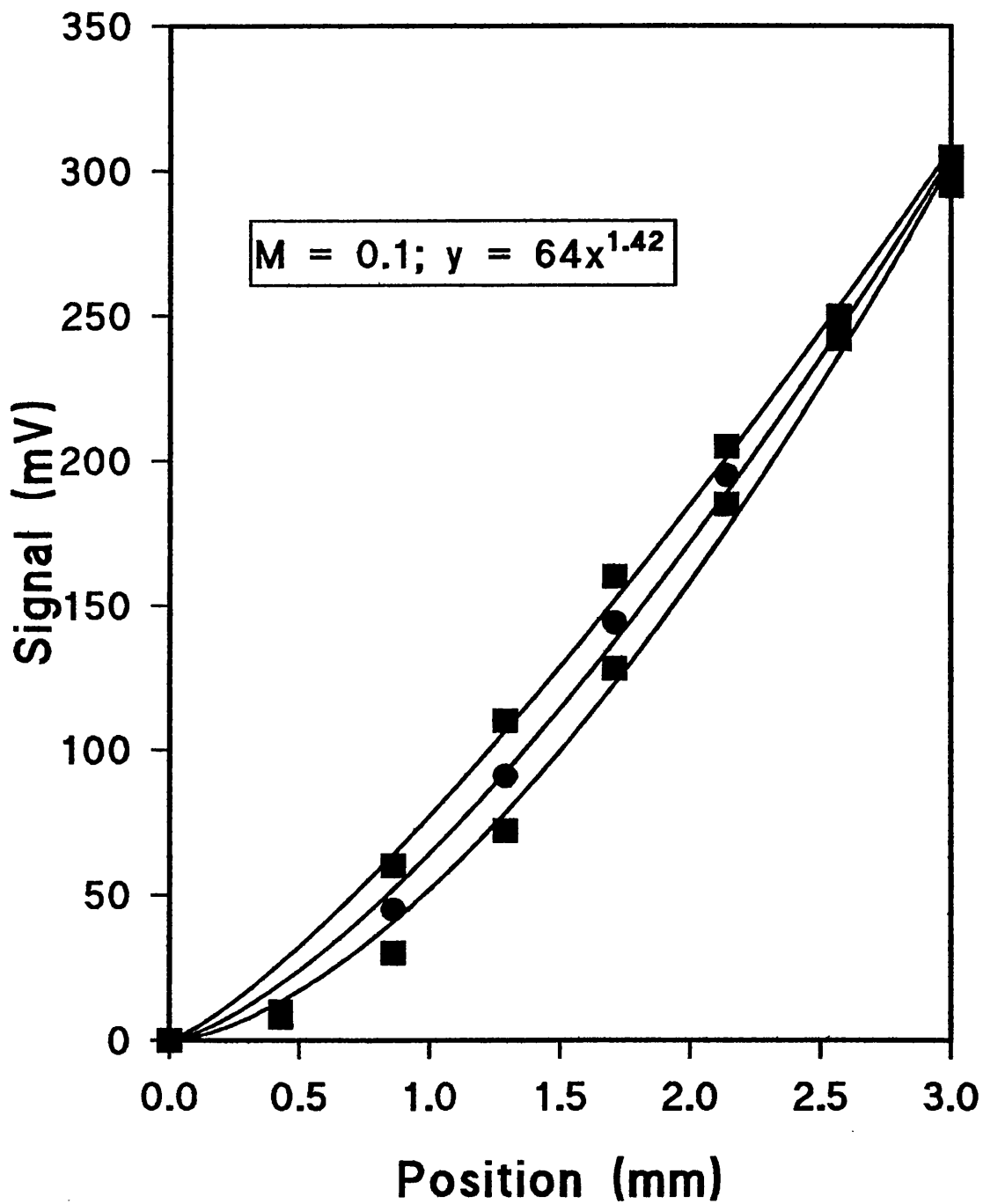


Fig. 6.7: ESF for Magnification = 0.1

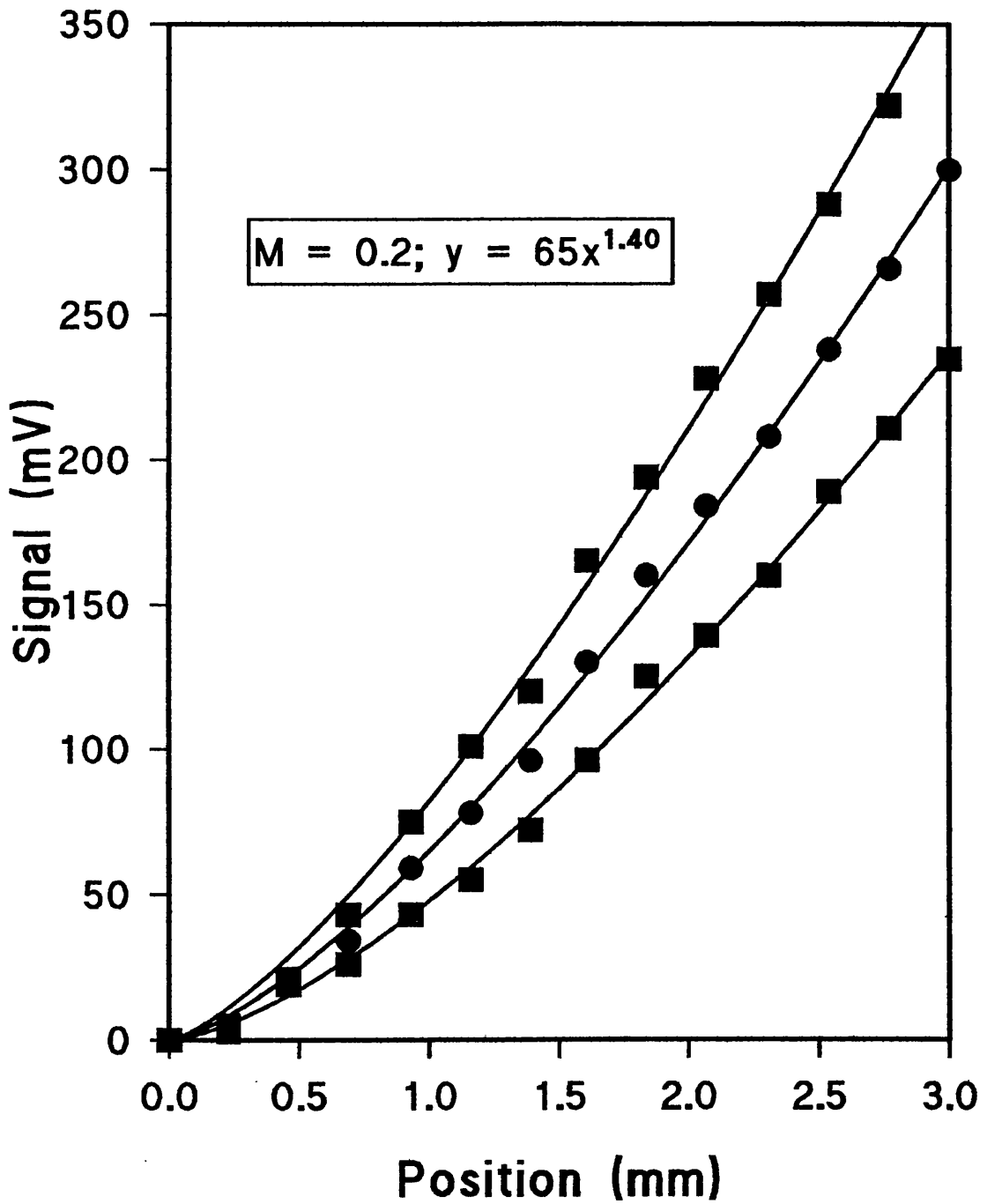


Fig. 6.8: ESF for Magnification = 0.2

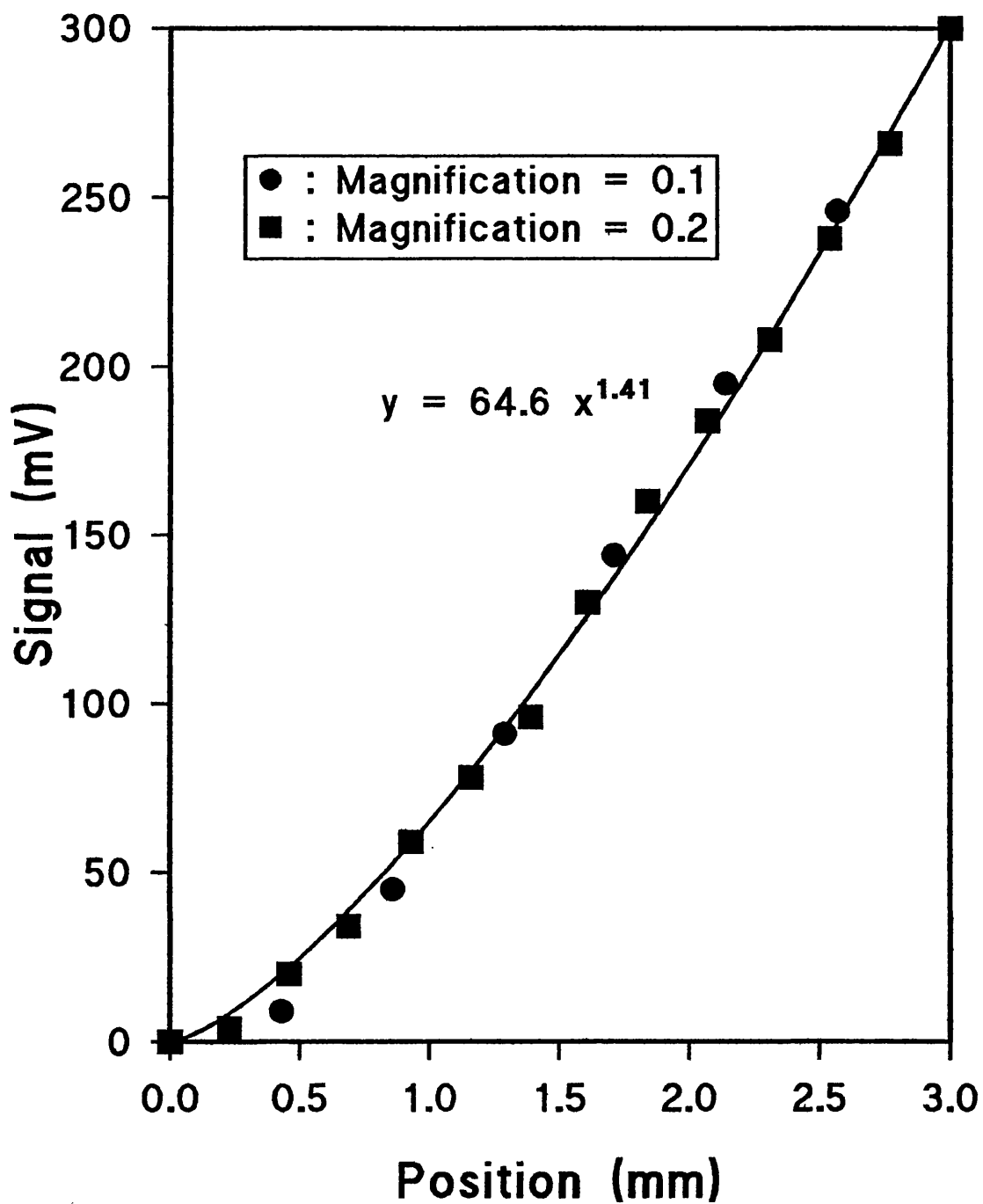


Fig. 6.9: Normalised ESF's for different Magnifications

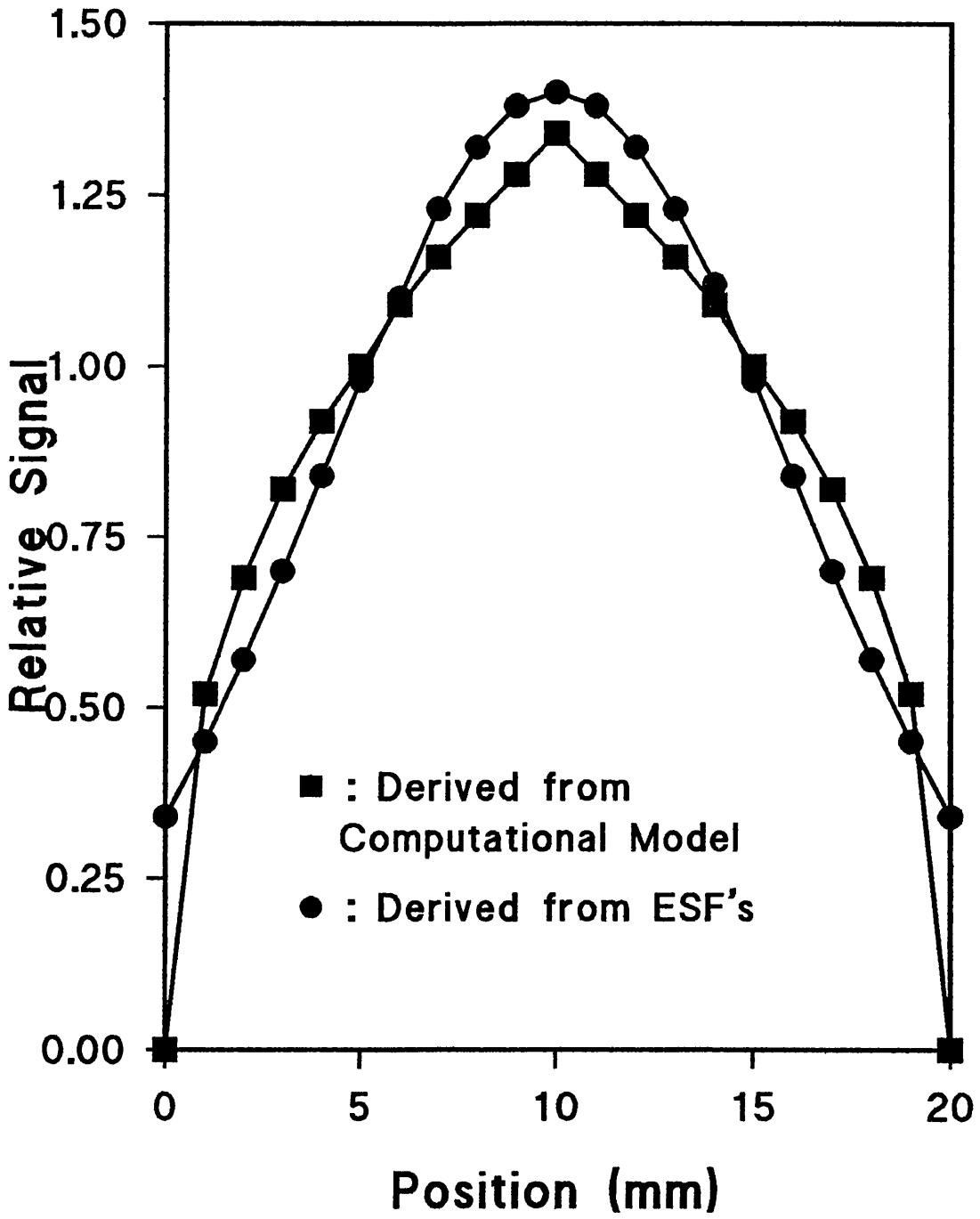


Fig. 6.10: Comparison of PSF's

Gaussian makes it an unrealistic PSF and for this reason the PSF found in this section will be used for future modelling. A possible explanation of the shape of the PSF will be given in section 6.5(iii).

6.5: EFFECT OF THE EXPERIMENTAL SET-UP ON THE PSF

The principal parameters that vary throughout this project are: (i) the magnification, M and (ii) the source temperature, T . A brief outline of the effect of varying some other parameters is also given. They are (iii) the temperature range set on the imager and (iv) the aperture setting. The difference between a hot to cold temperature step and a cold to hot temperature step is investigated in (v).

6.5(i): PSF as a function of magnification, M

It is widely recognised that the spatial resolution is largely limited by the lateral heat spread across the detector surface during one frame period. Watton [55] showed this effect by reticulating the target in order to thermally insulate each element from its surroundings and he achieved a factor of 3 improvement in the spatial resolution.

This fact implied that the resolution should improve as the magnification increased. This follows because:

(a) The temperature gradient across the image will increase as the object distance increases (and hence the magnification will decrease) because the

image will occupy a smaller area, although this will be offset to some degree by the decrease in intensity transmitted through the imagers' aperture by virtue of the objects greater distance from the aperture.

(b) If we ignore the effect of lens aberrations then the image will be a perfect copy of the object until the heat begins to dissipate. This process should be independent of magnification (except for the factor outlined in (a)) and therefore, in comparison with the size of the image, the heat spread will be greater for smaller magnifications.

These ideas underpinned the experiments of section 4.4(i)(a) and (b) and it was therefore rather surprising to find (see Figs. 4.10 and 4.11) that the temperature underestimation was independent of object distance. This factor implies that the spatial extent of the PSF increases linearly with magnification and the aim of the following experiment is to test that theory.

As in section 6.4(ii), the ESF was measured by shielding half of the heat source and measuring the signal across the temperature step with the oscilloscope. The PSF could then be found by differentiation and the results are shown in Fig. 6.11.

The results were measured as signal (mV) as a function of position measured on the oscilloscope (μs). This was then converted to the equivalent position in space to yield the figure. This shows unequivocally that the spatial

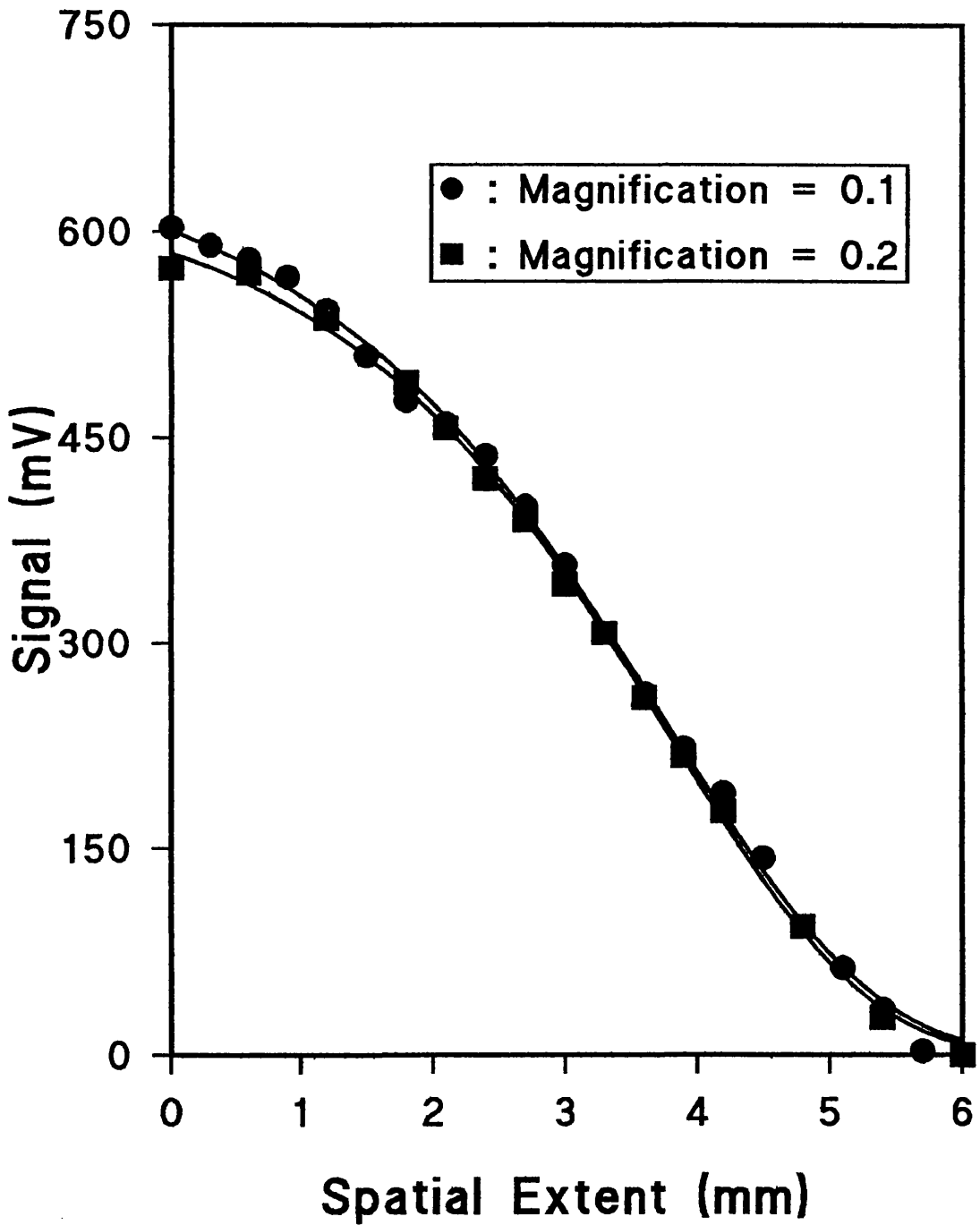


Fig. 6.11: Comparison of Normalised PSF's

extent of the PSF is inversely proportional to the magnification, as the magnifications are normalised to unity.

This then confirms that the PSF is dependent on magnification contrary to the theory expressed in (a) and (b) above. This suggests that heat dissipation is not the greatest factor in the loss of spatial resolution. The loss due to optical aberrations and the finite electronic bandwidth (reduced to improve the signal to noise ratio) may have a greater contribution. It is also possible that the idea postulated in (a) has an offset so great that the temperature gradient is larger for relatively small object distances. However, the experiments summarised in Figs. 4.10, 4.11 and 6.11 carry far more weight than any speculations and it can be concluded that the width of the PSF is linearly proportional to the magnification.

This makes the computational model simpler, as results can be predicted for any object distance simply by normalising the magnification to, for example, unity.

6.5(ii): PSF as a function of source temperature, T

In order to keep the computational model as simple as possible it is necessary for the PSF to behave in a predictable way for different source temperatures over the temperature range set on the imager. To investigate this relationship, the ESF was measured for various source temperatures, a curve-fit was applied and the curve was differentiated to produce the PSF. As in

section 6.4(ii), it was assumed that the PSF was symmetrical and so the equation derived described only one half of it. The equation for the PSF was of the form

$$y = A x^B \text{----- (6.15)}$$

and the results for various source temperatures are given in Table 6.1 below

Importantly, B can be seen to be constant to within experimental accuracy. The general shape, therefore, does not vary with temperature. However, A varies in proportion to $\Delta T^{1/2}$. This can be seen in Fig. 6.12 where ΔT represents the temperature above minimum detectable temperature.

The model developed so far in this chapter did not take this temperature dependence into account. Instead, it assumed a linear relationship. Fortunately, this is not likely to lead to major errors but the result will be borne in mind when we come to consider the problem of deconvolution in the next chapter.

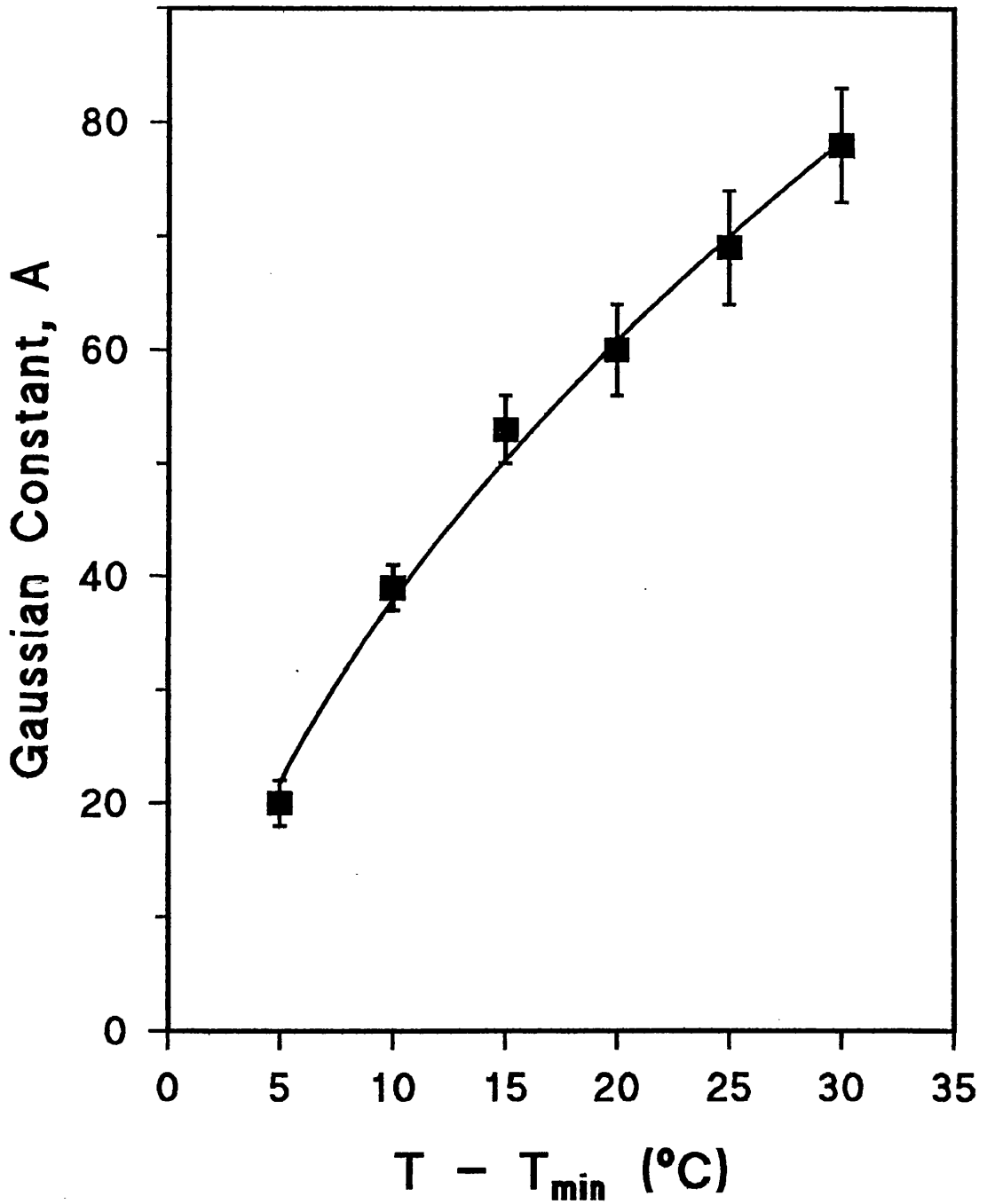


Fig. 6.12: Gaussian Constant, A , as a function of source temperature

Table 6.1: PSF as a function of source temperature

SOURCE TEMPERATURE (°C)	A	B
35	20 (± 2)	0.75 (±0.1)
40	39 (± 2)	0.7 (±0.06)
45	53 (± 3)	0.7 (±0.06)
50	60 (± 4)	0.8 (±0.06)
55	69 (± 5)	0.7 (±0.06)
60	78 (± 5)	0.8 (±0.06)

6.5(iii): Effect of temperature range

It has been assumed thus far that the temperature range set on the imager has no effect on the PSF. This could be assumed because all of the significant experiments throughout this project have been undertaken with the temperature range on the imager set at 30 - 60 °C. However, the temperature range was set at 40 - 50 °C and the results are compared with the ESF measured at the standard temperature range of 30 - 60 °C in Fig. 6.13.

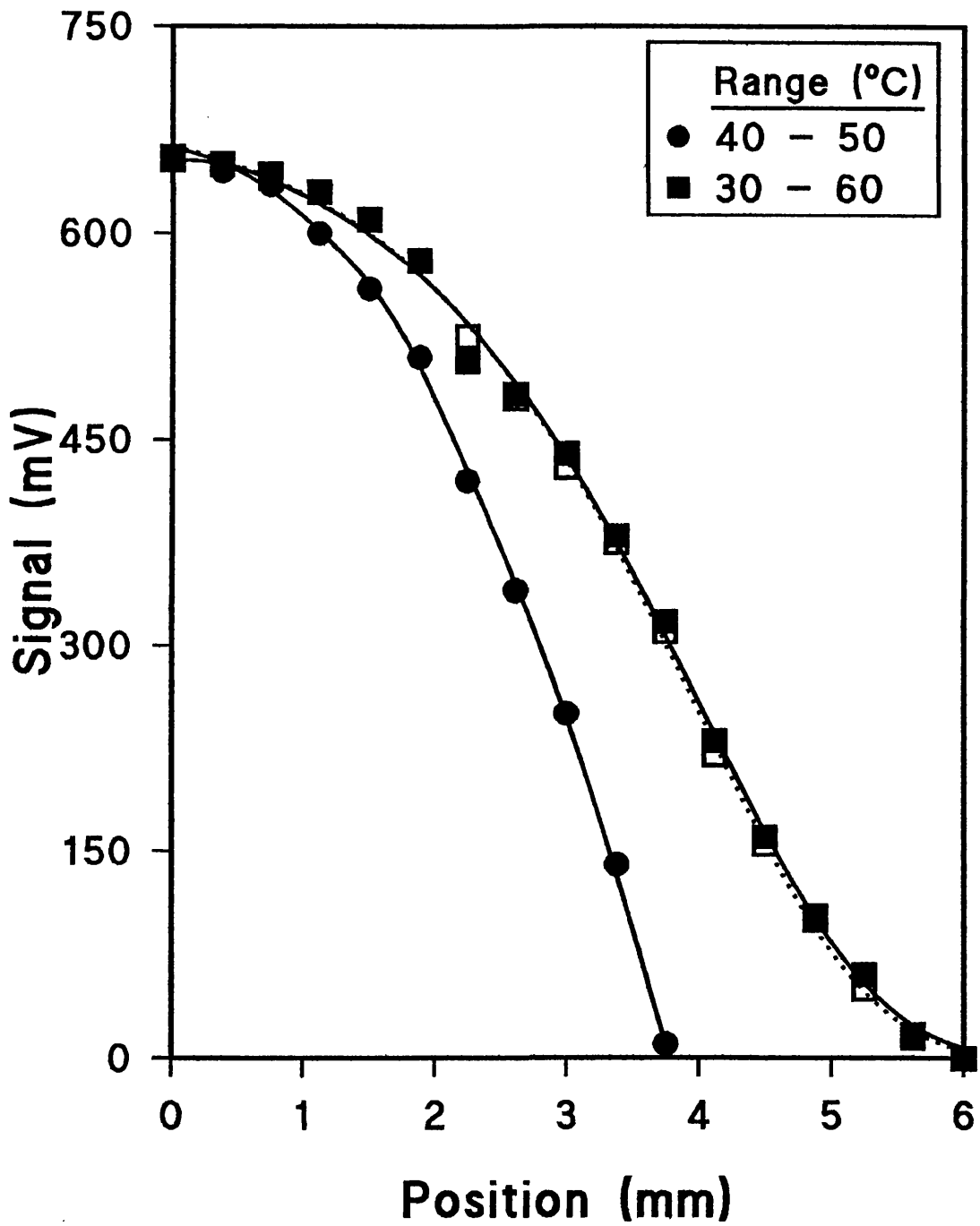


Fig . 6.13: Effect on ESF of varying temperature range

The difference between the two curves can be explained as follows. Fig. 6.14 is a representation of both sources, (i) at $T = 48\text{ }^{\circ}\text{C}$ and (ii) at $T = 54\text{ }^{\circ}\text{C}$, i.e. both at $T_{\min} + 4/5 (T_{\max} - T_{\min})$. The temperature distribution at the detector surface is represented by the dotted lines.

However, the gain and black level are different so the processing electronics ignore all signals corresponding to $T \leq 40\text{ }^{\circ}\text{C}$ in case (i) and all signals corresponding to $T \leq 30\text{ }^{\circ}\text{C}$ in case (ii). There is therefore a larger apparent PSF in case (ii) as illustrated in Fig. 6.13.

This effect is relatively trivial for results derived in this section. However, this is not the case in the next Chapter when we come to consider deconvolution. Here, not only do we have to apply the correct PSF, but we also have to extrapolate the apparent temperature distribution down to room temperature. This process should produce a relatively small contribution towards the overall errors.

It was not considered worthwhile to set the minimum temperature of the imager at room temperature in order to overcome this problem, as this quantity can vary throughout the day and from day to day. In addition to this, it is too restrictive to constrain all measurements to a minimum temperature of approximately $20\text{ }^{\circ}\text{C}$. For example, if the maximum temperature resolution is desired (temperature range = $4\text{ }^{\circ}\text{C}$) around, say, $40\text{ }^{\circ}\text{C}$, then the minimum temperature would have to be set at $38\text{ }^{\circ}\text{C}$. For these reasons a minimum

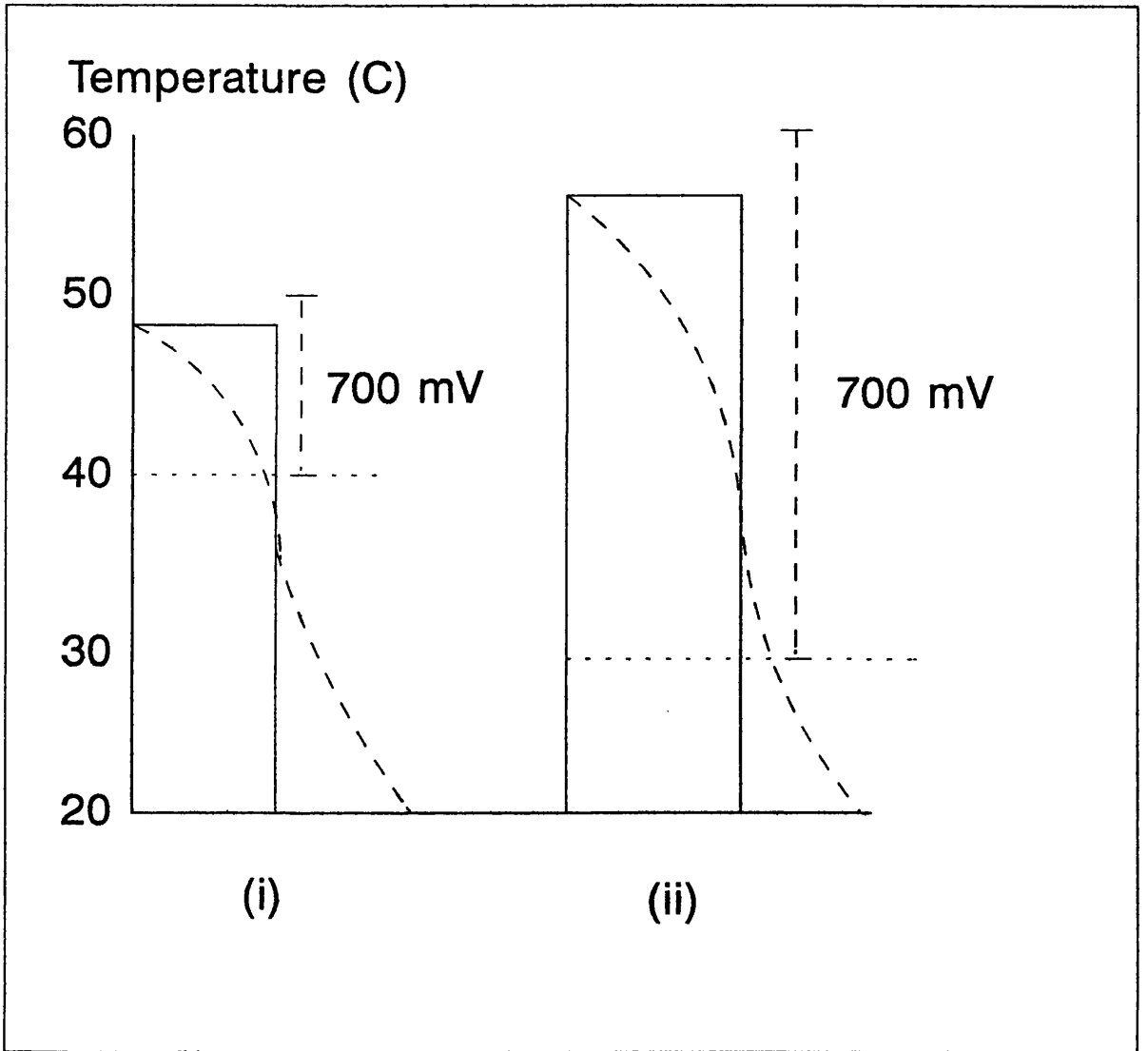


Fig. 6.14: Why the ESF's of
Fig. 6.13 are different

temperature of 30 °C was set throughout the experiments in order to see if accurate temperature measurements could be obtained when applying this extrapolation.

6.5(iv): Effect of orientation of temperature step

The dotted line in Fig. 6.13 shows the PSF that was measured for a cold - hot temperature step, as opposed to the hot - cold transition in the other curve. As can be seen from the fig. there is no discernible difference between them, which allows us to avoid the complications that a difference would have entailed.

6.5 (v): Effect of aperture size

A parameter often associated with the spatial resolution and hence the PSF of imaging devices is the "f-number", which is defined as the ratio of the focal length of the lens to the diameter of the aperture. This is certainly an important factor if optical aberrations have a significant role in degrading the image and it also helps in eliminating non-paraxial effects.

However, it was of little use for our purposes as the infrared intensities involved were so small. In normal operation, the imager was operated at maximum aperture which is $f/0.7$ or $50/0.7 \approx 70$ mm. Moving to the next aperture setting of $f/1.0$ brought about a reduction in intensity of a factor of 2 as the intensity is proportional to the area, i.e. reduction in intensity =

$(1/0.7)^2 \approx 2$. Although the gain and black level can be adjusted to accommodate this change of intensity, the noise was correspondingly greater leading to great uncertainties in the measurement of the signal. For this reason, the maximum aperture setting was retained.

6.6: CONCLUSION

We have now developed a computer model which can accurately predict image distributions from a knowledge of the object distributions and an accurate representation of the PSF. It has been studied under a wide range of operating conditions and the knowledge gathered can be carried forward when addressing the inverse problem, viz. predicting the object distribution from knowledge of the image distribution and the PSF. This problem forms the subject of the following Chapter.

CHAPTER 7:

COMPUTATIONAL MODEL(II): DECONVOLUTION

In this chapter, we consider the inverse problem to that addressed in the previous chapter. There we used our knowledge of the PSF and the known temperature distribution of the source to predict the image distribution. Here, we will infer the object distribution from a knowledge of the PSF and the image distribution.

These predictions were then compared with some irradiated samples which were analysed using the picrosirius red staining technique described in Chapter 5.

7.1: DECONVOLVING CONSTANT TEMPERATURE SOURCES

Before attempting to predict the temperature reached in an irradiated biological sample, the deconvolution model was applied to the rectangular sources used in the previous chapter. These have the advantage of being simpler to work with and the temperature distribution is precisely known. It is

to be expected, however, that any errors involved in this analysis will be greatly increased in the final analysis involving irradiated samples.

The analysis involved was very similar to that carried out in Chapter 6. That is, the image (this chapter) / object (previous chapter) is scanned pixel by pixel and the PSF is used as a weighting function to redistribute the image / object intensity distribution.

In addition to this deconvolution model, another relatively simplistic model, which did not require knowledge of the PSF, was developed and it is described in section 7.1(i). The reason for taking this approach was that it was much simpler to develop and it took much less computing time to calculate. If its results were comparable with the more elaborate model, then it would be the preferable option.

The redistribution was a relatively straightforward matter when applied to the object, as each element in the object distribution gets redistributed in a well defined manner given by the PSF. However, when we consider an element in the image distribution, there are two additional problems that must be addressed.

Firstly, the origins of the signal that we are attempting to retrieve from the convolved image are constrained to lie within the boundaries defined by the source width. As we will have no a priori knowledge of the dimensions of

the source, it will have to be inferred indirectly. This is considered in section 7.1(ii).

Secondly, as explained in section 6.5(iii), we must take into account that part of the image which is ignored by the processing electronics. That is we have to estimate the contribution that comes from those parts of the image which have a temperature less than the minimum detectable temperature set on the imager. We look at this problem in section 7.1(iii) and finally, the results are presented in section 7.1(iv).

7.1 (i): Description of the computational models

7.1 (i)(a): The PSF model

Fig. 7.1 shows a typical image distribution. Firstly, the model estimates the source width, in this case, the distance AB. Then the image is extrapolated down to room temperature.

The screen is composed of a grid of pixels and the screen mode chosen for this work was 640 x 200, so the image could be split up into a maximum of 640 elements and each element was considered in turn.

If we consider element, i , for example, the dashed curve surrounding it represents the PSF. The magnitude of the PSF at a particular position is interpreted as the probability that the radiation was emitted from a corresponding element in the object distribution. However, in this case, we

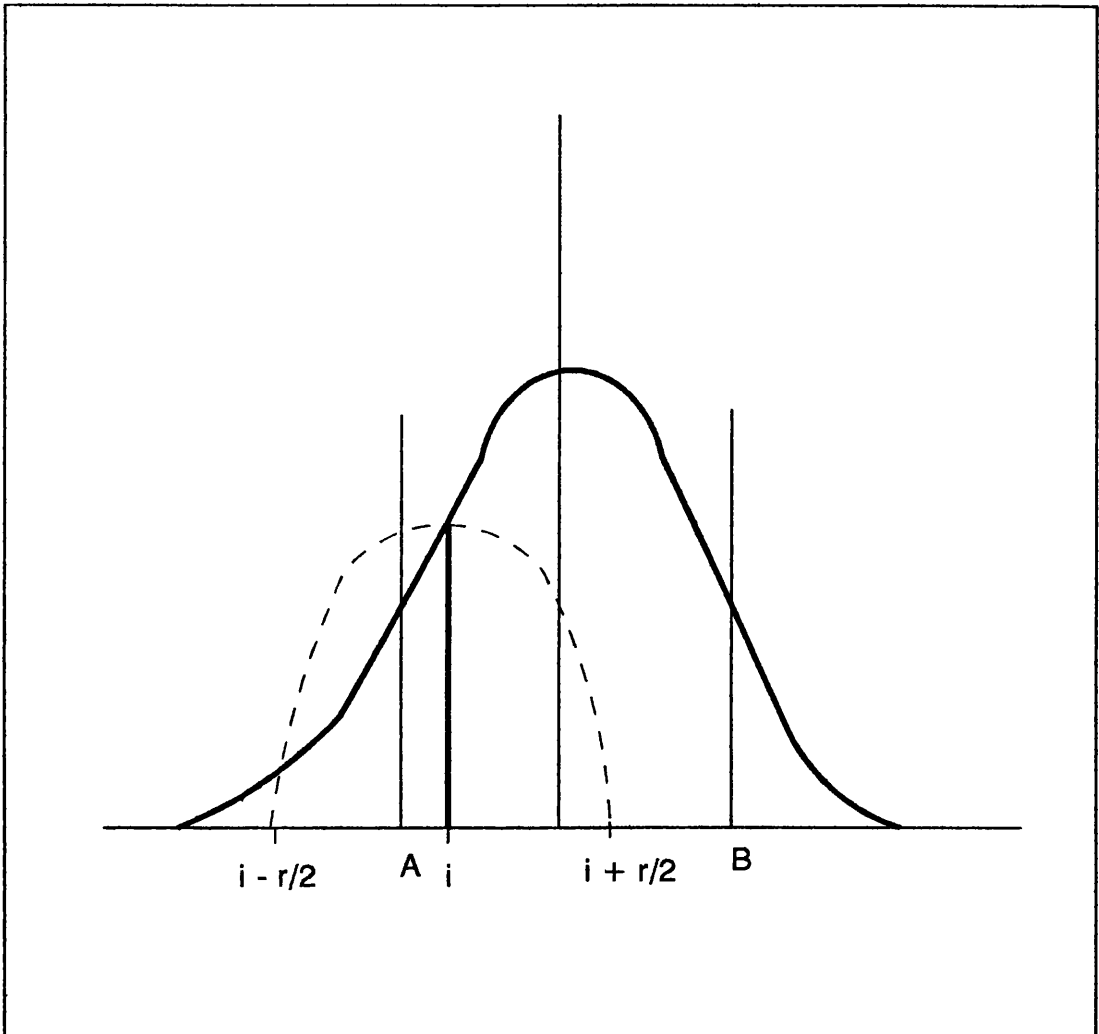


Fig. 7.1:Image distribution for analysis by computational model

have the additional constraint that it must have originated from a position within AB. Therefore, the image at element i is redistributed between A and $i + r/2$.

It is, of course, only necessary to carry out this process up to pixel 320 as the object and image are assumed to be symmetrical. This applied to all objects studied here but the program could easily be extended to 640 pixels if required.

7.1 (i)(b): The equal area model

This is a very simple model used for comparison with the PSF model. It works by predicting the width and extrapolating the image down to room temperature, as above, and then calculating the area of the image by summing all of the values of the elements. It then redistributes the area within the boundaries AB, assuming a constant temperature source. This may be expected to work well for constant temperature sources but it is less likely to do so for sources irradiated by laser energy, as the true distribution will not be rectangular.

7.1 (ii): Estimation of source width

This estimation is possible only if an image distribution corresponds uniquely to a given object size and temperature. That is, for a source of lateral dimension, X , and a temperature, T , there must not exist a source of lateral

dimension, $X - \Delta X$, and a temperature $T + \Delta T$ whose image corresponds to the former's image. Obviously, if ΔX and ΔT are small enough, then it will be impossible to differentiate between them, but for our purposes it was considered to be acceptable if two sources with lateral dimension differing by 1mm could be clearly resolved at all temperatures.

To investigate this, the output signal for a 4 and 5 mm source width was recorded for various temperatures. The results are shown in Fig. 7.2 and two points are worth noting about the graph.

(i) There is clearly no correspondence between the 5 mm source at 50 °C and any of the 4 mm sources. This means that, for constant temperature sources, the source width can be inferred unambiguously.

(ii) It is clear from Table 7.1 that two parameters are required to infer the width unambiguously. This table shows the position of the half-maxima for source widths of 3, 4 and 5 mm for different source temperatures. If this was the only parameter used to specify the width, then the measurements marked by an asterisk for the 3 different widths could not be clearly differentiated.

However, consideration of the signal amplitude will surmount this problem. Fig 7.3 shows the graphs obtained experimentally for 3 different source widths and the equations derived from the graphs must be written into the computational model in order to obtain an estimate of the source width.

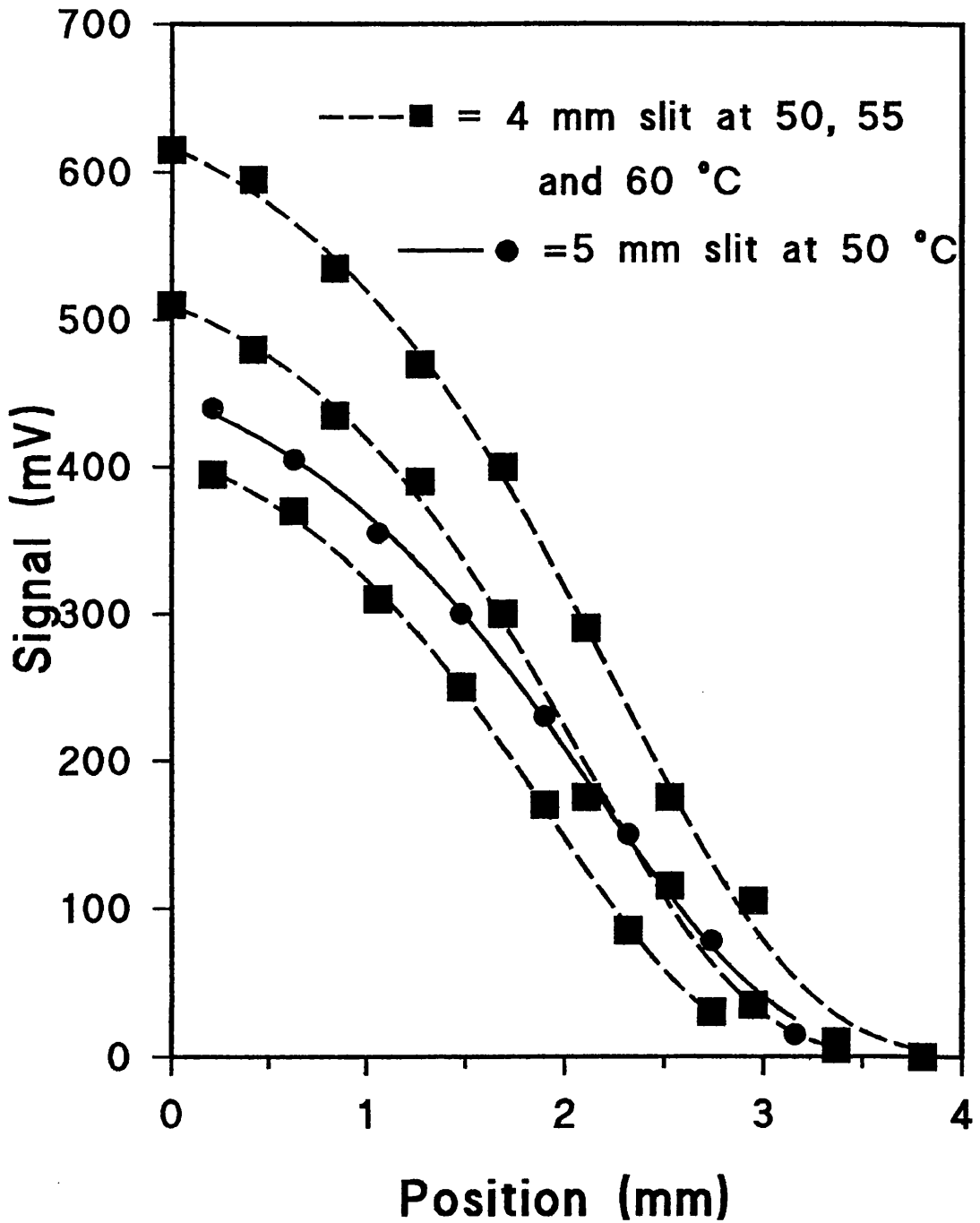


Fig. 7.2: Comparison of PSF for 4 and 5 mm slit widths for different temperatures

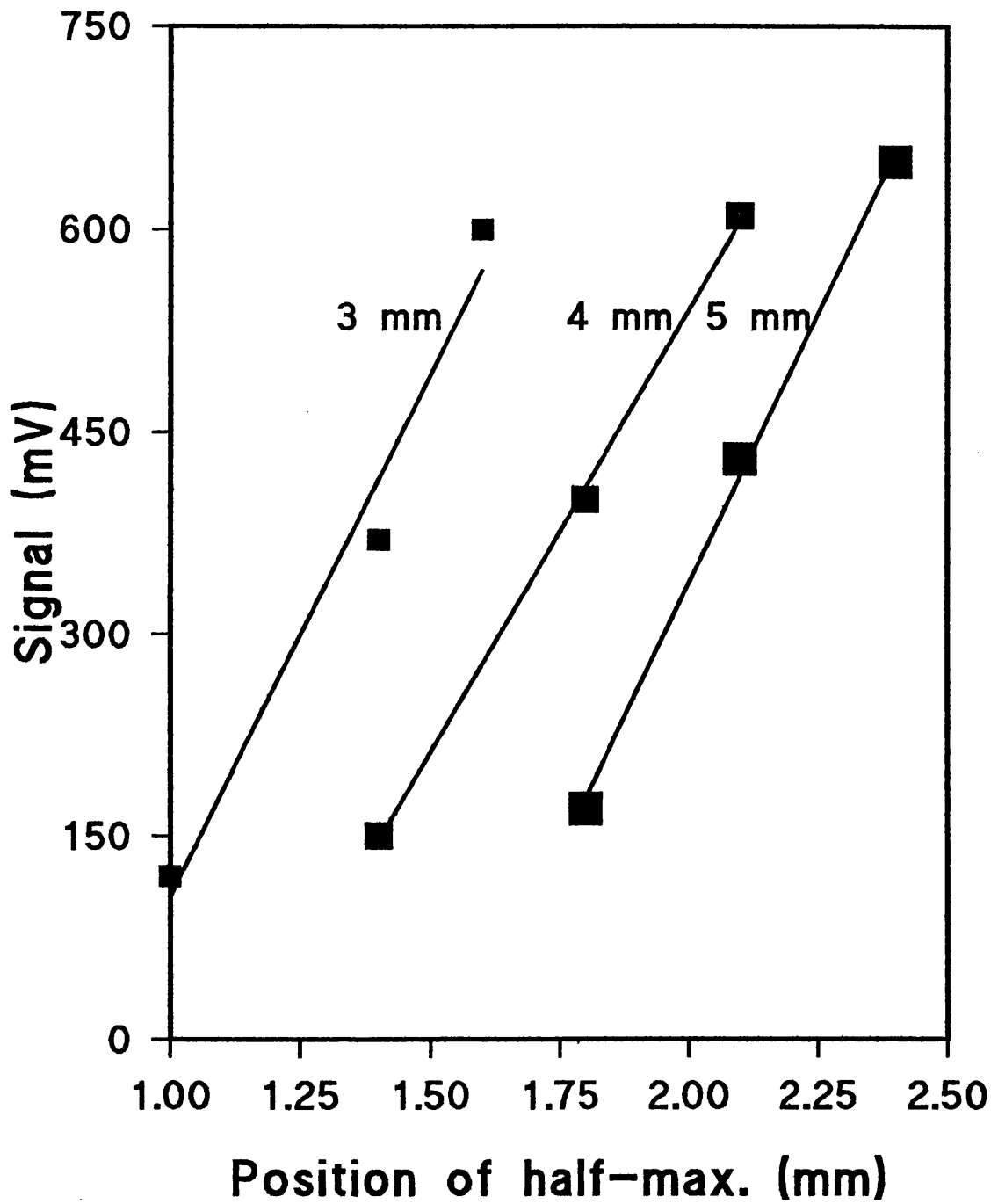


Fig. 7.3: Experimental data used to determine source width

Table 7.1: Position corresponding to half maximum signal

source width	T(°C)	half max. signal
3	40	1.1
	50	1.5
	60	1.7 *
4	40	1.5
	50	1.75 *
	55	2.0
	60	2.2
5	40	1.8 *
	50	2.1
	60	2.3

Table 7.2: Computational model estimates of source widths

Actual source width (mm)	Estimated source width (mm)	error (mm)
1	0.9	0.1
2	1.9	0.1
3	2.9	0.1
4	4.1	0.1
5	5.0	0
6	5.9	0.1

To test the accuracy of this method, signals were recorded for source widths of 1-6 mm and the equations of Fig. 7.3 used to predict the source width. The results are shown in Table 7.2 giving an average error of ± 0.1 mm.

7.1(iii): Extrapolating the image down to room temperature

In estimating the temperature distribution below the threshold temperature, two principle factors govern the outcome.

Obviously, the shape of the distribution is important, but to avoid being over-elaborate, a straight line was chosen as the true distribution does not vary far from this shape. By viewing the distribution with the imager set for a temperature range of 22.5 °C (room temperature) and 60 °C, it was decided that a realistic extrapolation could be obtained by calculating the gradient between the central point of maximum temperature and the point where the image falls to the threshold temperature of 30 °C. Fig. 7.4 shows an example of this for an image of a 4 mm source. The vertical lines represent the estimation of source width and the horizontal lines represent 22.5 °C (room temperature) and 30 °C (threshold temperature set on the imager).

Another factor which has an important bearing on the outcome is the measurement of room temperature, which was measured using a mercury-in-glass thermometer. Its importance is shown in the next section.

BFIG74 .BMP

WIDTH= 4.002353

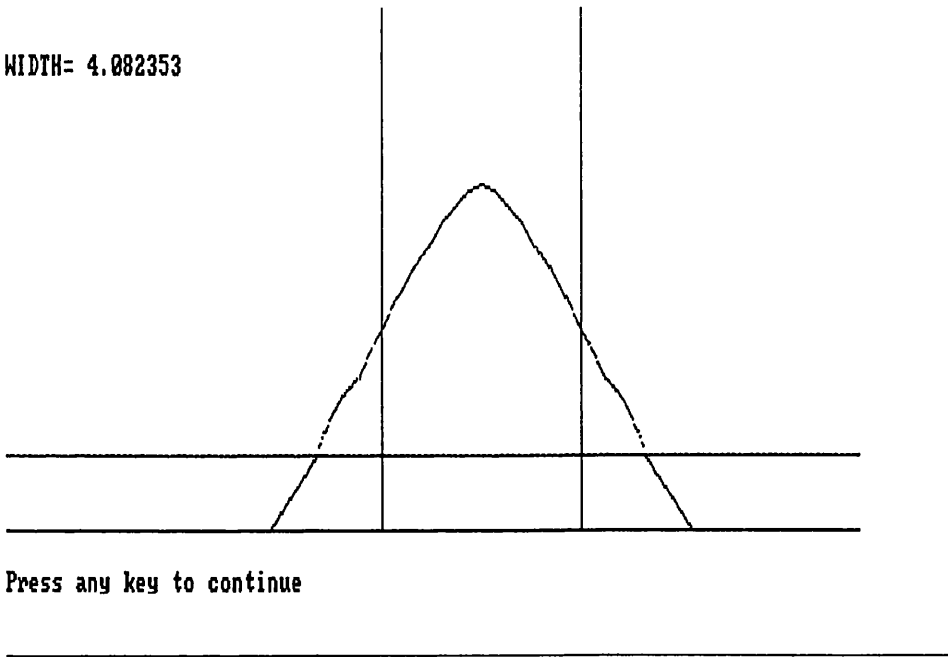


Fig. 7.4: Example of extrapolation of image distribution below threshold temperature

7.1(iv): Results

7.1(iv)(a): The Equal Area Model

The results for the Equal Area Model are shown in Table 7.3.

**Table 7.3: Temperature Estimates of Constant Temperature
Sources by Equal Area Model**

Width (mm)	Estimated Width (°C)	Actual Temperature(°C)	Estimated Temperature(°C)
1	0.91	58	61.1
2	2.11	58	57.1
3	2.95	58	57.0
4	4.08	58	57.3
5	5.0	58	59.2
6	5.99	58	58.2

Average Temperature Estimate = 58.3 °C.

The results suggest that the principles behind the method are valid and the greatest contribution to the errors come from an inaccurate reading of the image signal and the room temperature.

7.1(iv)(b): the PSF Model

The results for the PSF model are shown in Table 7.4. A comparison with temperature measurements without the models corrections is also given.

**Table 7.4: Temperature Estimates of Constant Temperature
Sources using the PSF Model**

Width (mm)	Actual Temperature(°C)	Estimated Temperature(°C) (PSF model)	Estimated Temperature(°C) (no correction)
1	58	60.8	40
2	58	56.9	46.5
3	58	57.0	50
4	58	57.3	53
5	58	59.2	56
6	58	58.4	58

Average Temperature Estimate (PSF model) = 58.3 °C.

Figs. 7.5, 7.6 and 7.7 show the PSF computational models output for source widths of 2, 4, and 6 mm respectively. As expected the results for the average temperature estimation agree closely with the results of Table 7.3. However, in this case, the average temperature estimation is superimposed on the estimate of the temperature distribution which is seen to vary over the source width. As indicated in the previous section, the source of the errors which contribute to this variation are the inaccuracies in the measurement of

BFIG75.BMP

WIDTH= 2.105883
AVE. TEMP. = 56.92234

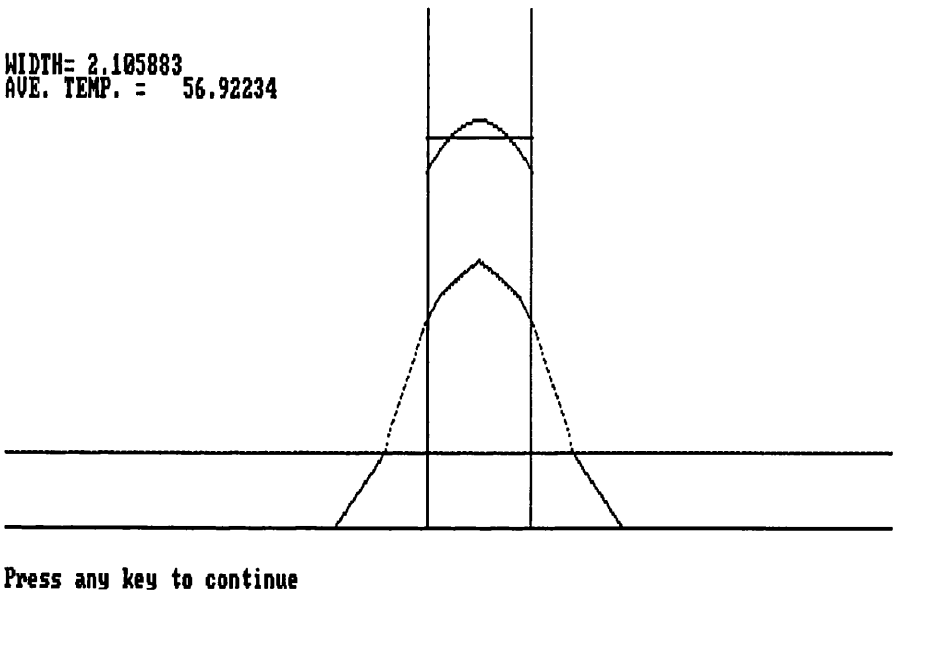


Fig. 7.5: PSF Computational model
output for 2 mm source

BFIG76.BMP

WIDTH= 4.082353
AVE. TEMP. = 57.27681

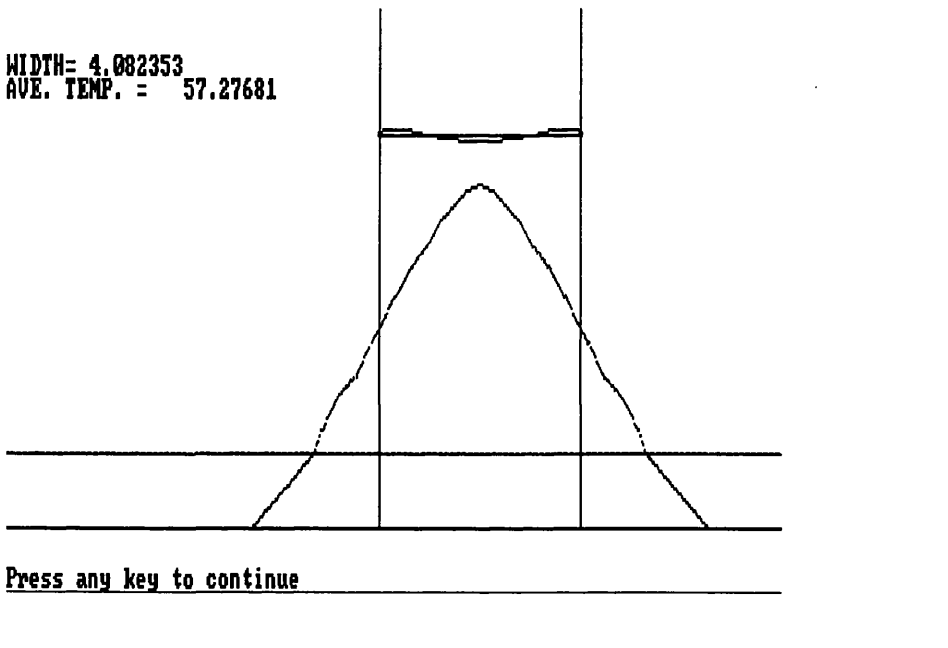


Fig. 7.6: PSF Computational model
output for 4 mm source

BFIG77.BMP

WIDTH= 5.988235
AVE. TEMP. = 58.42781

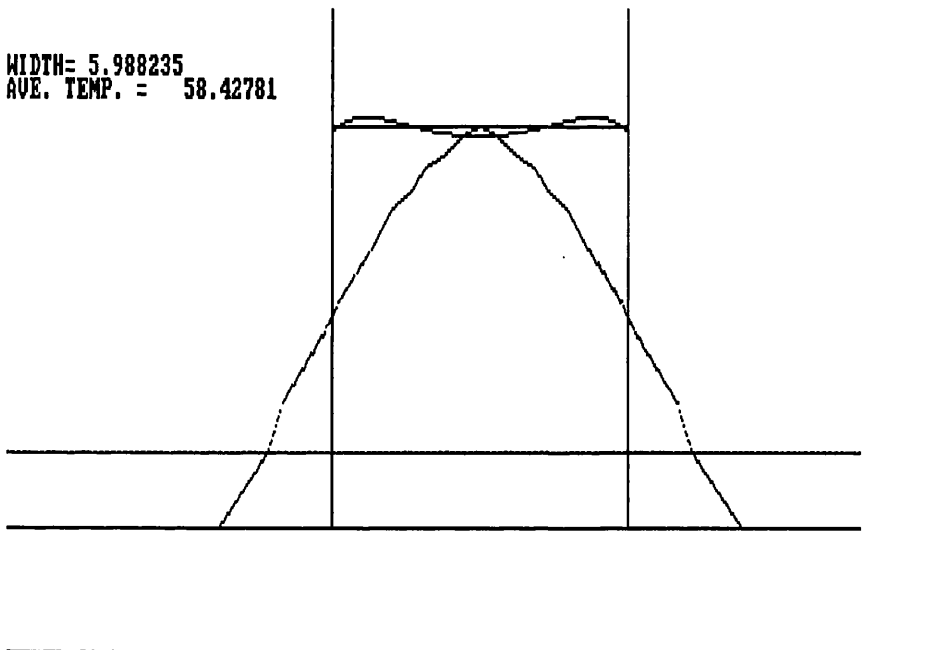


Fig. 7.7: PSF Computational model
output for 6 mm source

the image distribution and in the extrapolation of the image down to room temperature. The actual measurement of room temperature and the PSF will also be subject to inaccuracies.

However, it is clear that the application of the computational model now allows us to make realistic estimates of the temperature of small heat sources. This can be seen clearly in Table 7.4, where the greatest error is 2.8 °C for the 1 mm source compared with 20 °C for the uncorrected measurement.

In conclusion, this model gives an accurate estimation of temperature for constant temperature heat sources. Unfortunately, however, laser irradiated tissue is more likely to be Gaussian in profile. We look at Gaussian distributions in the next section.

7.2: DECONVOLVING A GAUSSIAN TEMPERATURE

PROFILE

To discover the effect of estimating the temperature profile of a Gaussian source, we firstly go back to the computational model developed in Chapter 6 to find out, at least approximately, what the image profile of a Gaussian source would look like. Secondly, the values of the convolved image are transferred to the model developed in the previous section to give an estimate of the temperature distribution of the original Gaussian source.

For the first part, the model is changed in such a way that the object temperature distribution no longer has a discontinuous change from room temperature to source temperature. Instead, it changes continuously in a Gaussian manner. A typical output is shown in Fig. 7.8, where the broader curve represents the degraded image. The parameters a and b at the top left of the figure define the shape of the Gaussian, i.e. ae^{-bx^2} . The values, $a = 138$ and $b = 0.00015$ relate to the output screen configuration: $640 * 200$ pixels. a corresponds to the peak temperature of $58\text{ }^{\circ}\text{C}$ and $b = 0.00015$ defines the width at half-maximum, in this case 4.08 mm . For different values of b we obtained different half-maximum widths ($\frac{1}{2}\text{ max.}$) and different temperature errors (δT). These are plotted in Fig. 7.9 along with the average of the curves of Figs. 4.10-4.13, which related to the temperature step.

For small slit widths, the experimentally determined temperature errors are very close to the errors estimated by the model for Gaussian curves of a particular width at $\frac{1}{2}\text{ max.}$ However, the curves diverge progressively as the slit width / $\frac{1}{2}\text{ max.}$ increases. This is to be expected as, for example, at a slit width of 6 mm , the central image point is receiving radiation from a constant temperature source of radius 3 mm , whereas if the source was Gaussian, then the source temperature would fall off from the central maximum.

The estimated distribution of the image produced by the Gaussian sources were then transferred to the deconvolution model which will then

BFIG78.BMP

a=? 138
b=? .00015
1/2 max(mm) = 4.08
Max. Temp.(°C)=? 58
Min. Temp.(°C)=? 23.5
Resolution(mm)=? 6
 $\delta T(^{\circ}C) = 6.5$

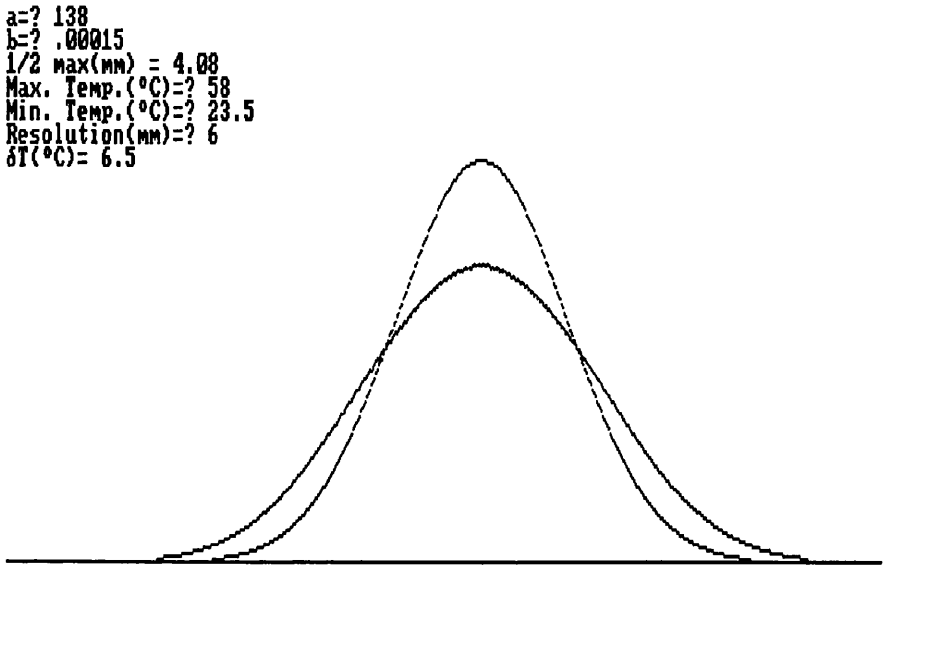


Fig. 7.8: Example of convolved
Gaussian source

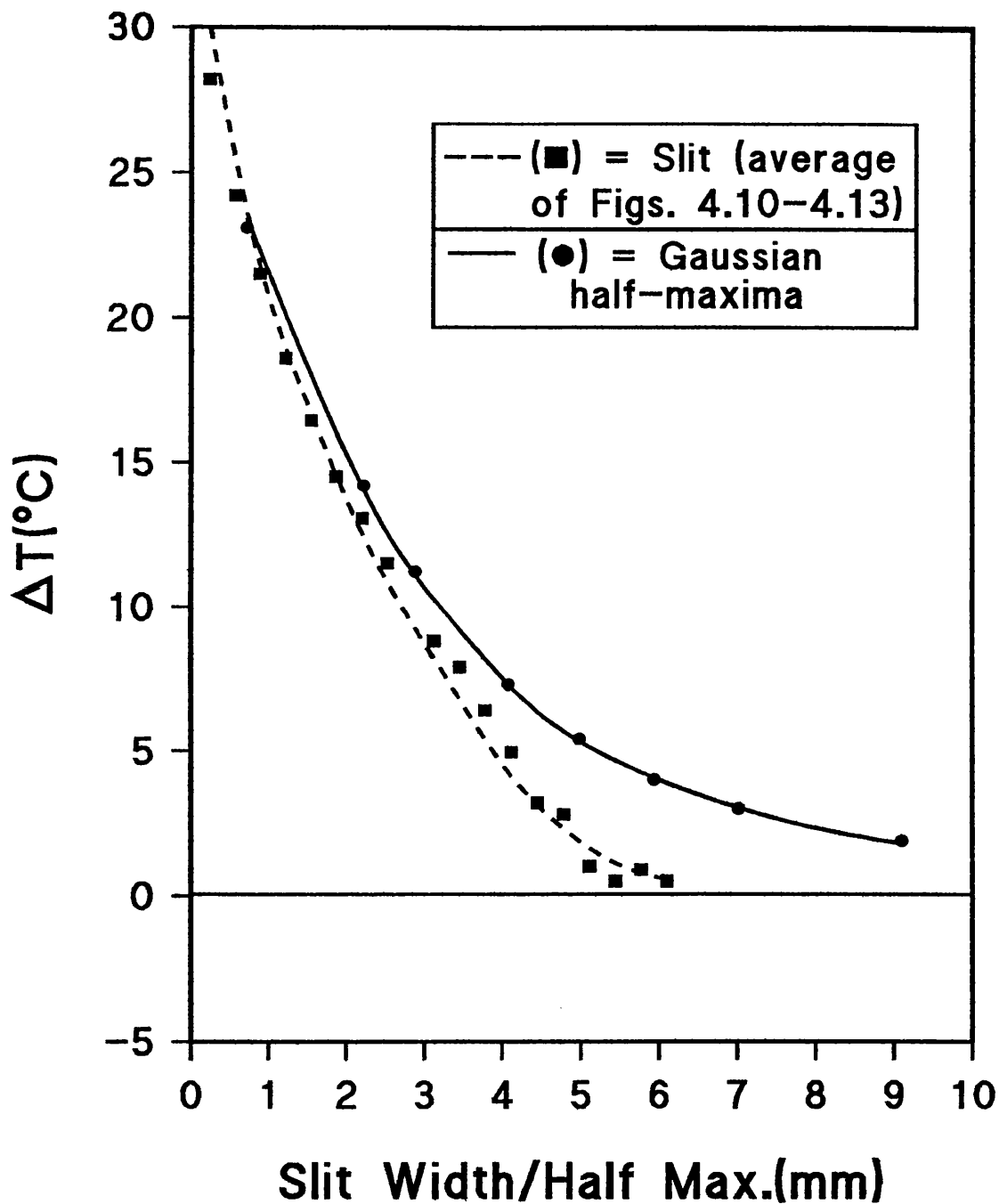


Fig. 7.9: Comparison of errors for Gaussian and rectangular temperature profiles

estimate the original temperature distribution. The obvious problem with this approach is that the model confines the object distribution between limits previously defined by the estimation of the source width.

Fig. 7.10 shows a typical output from this approach. The source width could be chosen to give an accurate average temperature estimate but the shape has been grossly distorted. For this reason a different model was developed that would allow a realistic estimate of the shape of the temperature distribution.

This involved scanning the distribution pixel by pixel and subtracting the PSF whenever it fitted under the convolved curve. The deconvolved curve was built up by adding a value of 1 to the position of the PSF centre each time a PSF representation was subtracted. This continued until no more subtractions were possible. This model will be referred to as the PSF subtraction model.

Fig. 7.11 shows a typical output for this approach. The deconvolved image is represented by the ^{dark}white, shaded area and only half has been shown for ease of comparison with the original source distribution. The actual temperature estimate is very accurate and the shape is reproduced to an acceptable degree. There is, however, an edge effect which requires some explanation.

BFIG710.BMP

a=? 138
b=? .0002
1/2 max(mm) = 3.54
dT = 12.15084
AVERAGE = 56.33928

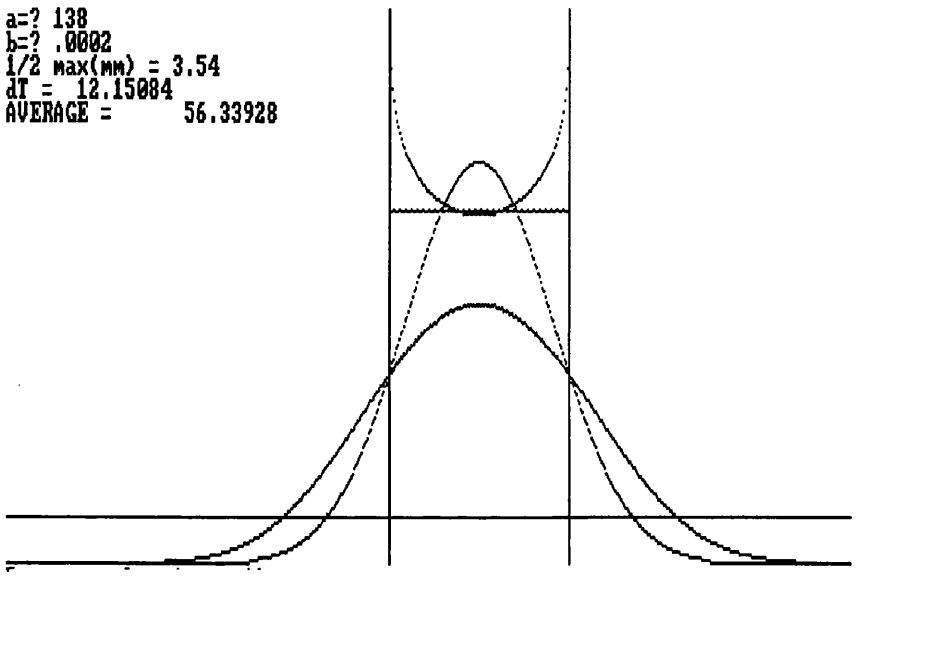


Fig. 7.10: Computer output for estimation of temperature of Gaussian source using PSF computational model

BFIG711.BMP

a=? 138
b=? .0002
Temp. = 58 °C
1/2 max = 3.54 mm
dT = 12.15084 °C
Estimated Temp. = 57.25 °C

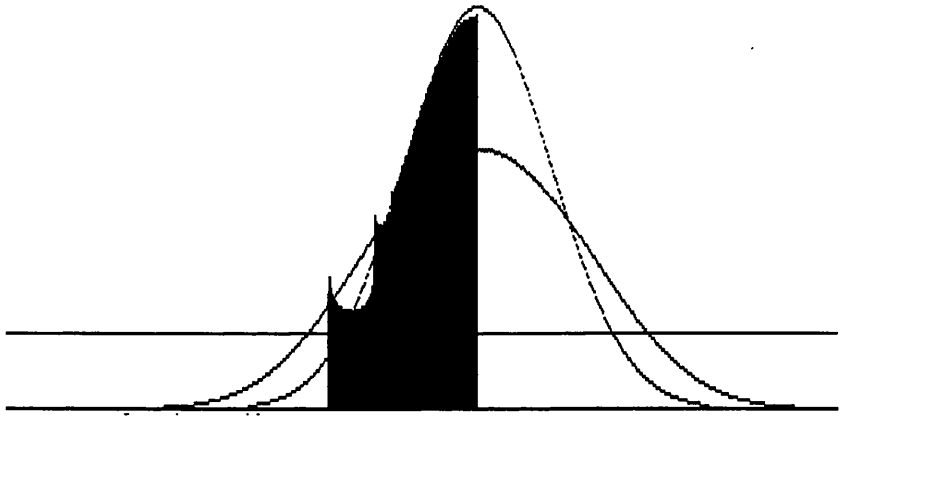


Fig. 7.10: Computer output for estimation of temperature of Gaussian source using PSF computational model subtraction

Each element of the object distribution is redistributed over 3 mm on each side, weighted according to the PSF. However, at the outer edges of the object distribution, where the temperature is close to room temperature, the contribution to the convolved image becomes negligible and this contribution is not registered.

Now, the deconvolution program scans the elements until a value of 1 has been detected. It then moves along the array for the equivalent of 3 mm (in this case, 100 pixels), before it starts to rebuild the object distribution. As can be seen in Fig. 7.11, this rebuilding begins further along the array than it should and so this element, and to a lesser degree, elements immediately to the right of it, receive a far greater contribution than they should. However, this is considered to be of minor importance as, even for smaller Gaussian curves, it has no effect in the overall result. Fig. 7.12 shows a deconvolved Gaussian distribution with a width at $\frac{1}{2}$ max. of 1.72 mm and the temperature estimate (58.75 °C) is very accurate.

Table 7.5 gives the results for a range of $\frac{1}{2}$ max. widths.

It would, of course, be possible to determine correction factors to deal with the edge effect. However, they would apply only to pure Gaussian curves and this will not be the case for sources which are irradiated by laser energy. This point is emphasised by applying the PSF subtraction model to constant

BFIG712.BMP

a=? 138
b=? .0008
Temp. = 58 °C
1/2 Max = 1.74 mm
dT = 21.376 °C
Estimated Temp. = 58.75 °C

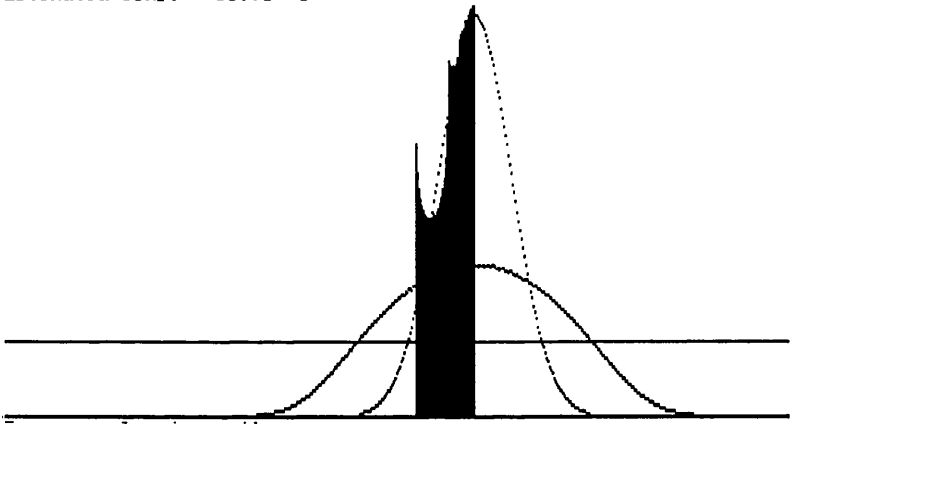


Fig. 7.12: Computer output for estimation of temperature of Gaussian source using PSF subtraction model (II)

**Table 7.5: Temperature estimates of Gaussian sources using the
PSF subtraction model**

Temperature	
$\frac{1}{2}$ max. (mm)	Estimate ($^{\circ}$C)
0.72	59.25
1.14	60.5
1.72	58.75
2.22	58.75
3.54	57.25
5.01	57.0

temperature sources. Fig. 7.13 gives an example of the computer output for a source of width 3 mm and Table 7.6 gives the temperature estimations for a range of source widths. It is apparent from Fig.7.13 that the edge effect becomes less important as the source approaches a temperature step. It is expected that the laser-irradiated sources will fall somewhere between these two extremes. In view of this and the fact that the temperature estimates were very accurate it was decided that correction factors here were of little value.

BFIG713.BMP

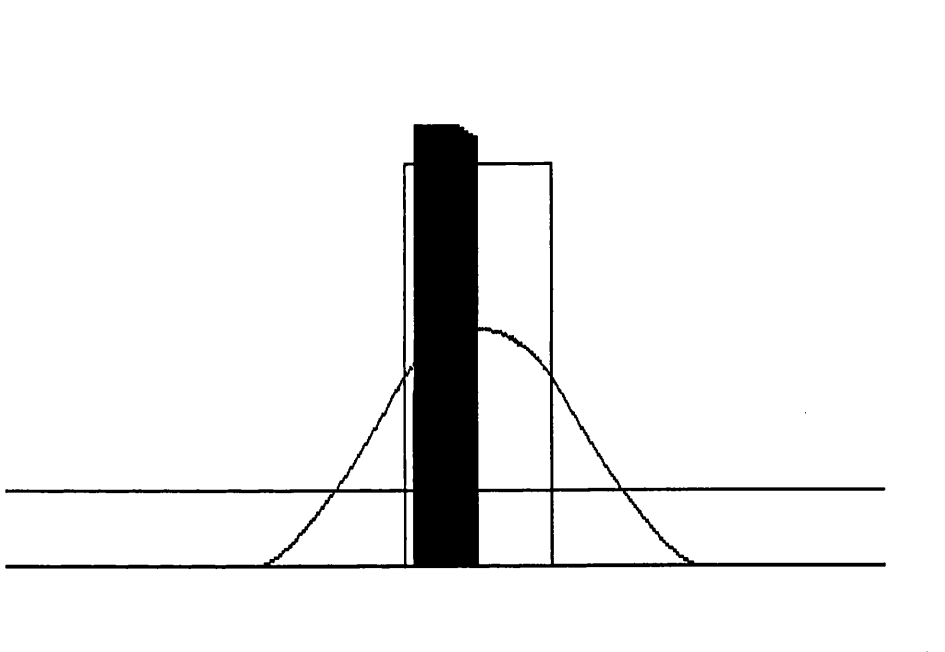


Fig. 7.13: Computer output for estimation of temperature of constant temp. source using PSF subtraction model

Table 7.6: Temperature Estimates of Constant Temperature

Sources Using the PSF Subtraction Model

Source Width (mm)	Temperature Estimates (°C)
1	61.5
2	60.8
3	60.2
4	59.8
5	59.3
6	58.8

7.3: ESTIMATING THE TEMPERATURE OF LASER-

IRRADIATED TISSUE

7.3(i): Description of the Experiment

For these experiments, bovine pericardium was irradiated with laser energy and the apparent temperature was monitored with the thermal imager connected to the oscilloscope, which allowed the apparent peak temperature to be measured to ± 0.5 °C. The pericardium was heated to various apparent temperatures and the samples were analysed with the picrosirius red staining technique.

The video signal from the thermal imager was recorded on video tape for subsequent analysis. This involved freezing the video recording at the frame corresponding to the maximum temperature and reading off the temperature distribution across the image. These values were then transferred to the PSF subtraction model for an estimation of the true temperature distribution.

It has been shown to be very accurate when tested in the controlled situations described in the previous sections. However, a true measure of its accuracy can only be found by considering its performance when estimating temperatures measured during laser irradiation. The errors involved when measuring the apparent temperature distribution are added to the previously existing sources of error. In particular, when freezing the video image, the noise is far greater than it is when viewing the image in real time.

The aim is to find the apparent temperature that corresponds approximately to the transition temperature of 65.5 °C. When this was done, more samples were irradiated to apparent temperatures of 1, 2, 3, 4 and 5 °C above and below this temperature. The picrosirius red staining technique will then give a clear indication of the sample which was heated to the transition temperature. The apparent temperature distribution can then be deconvolved with the model to compare the outcomes with two techniques.

7.3 (ii): Results

The apparent temperature was found to be in the region of 45 °C, so 11 samples were irradiated to apparent temperatures of 40 - 50 °C in 1 °C steps. Fig 7.14 shows examples of tissue heated to (a) 44 °C, (b) 45 °C, (c) 46 °C and (d) 47 °C. The transition appears somewhere in this region though it is not possible to be any more precise using these samples and it is unlikely that repeating the experiment would make the position any clearer. This is because a certain amount of judgement is required in determining when the predetermined temperatures have been reached. No optical inactivity was detected in samples heated to apparent temperatures of below 45 °C. Sample (b) (45 °C) shows some optical inactivity, yet sample (c) (46 °C) does not. All other samples (≥ 47 °C) exhibit optical inactivity.

However, the video signal for each of these examples was analysed using the PSF subtraction model and the results are shown in Table 7.7.

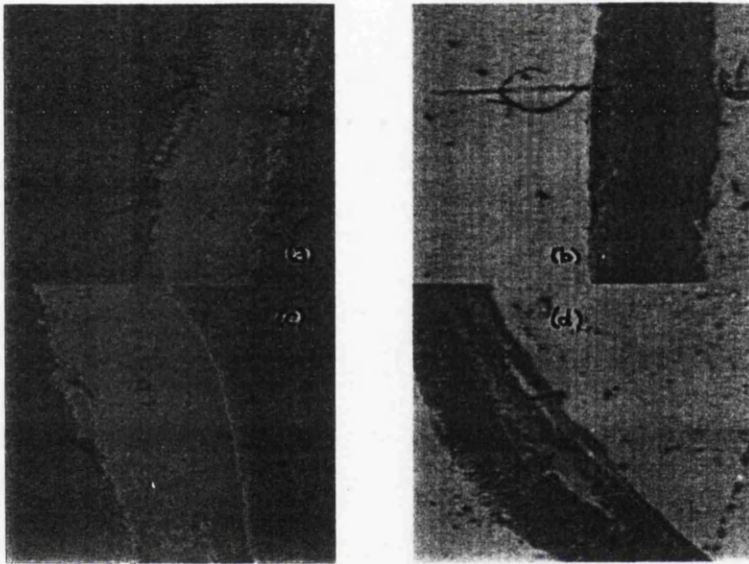


Fig. 7.14: Stained tissue samples heated with laser energy to (a) 44 °C (b) 45 °C; (c) 45 °C; (d) 47 °C

**Table 7.7: Temperature estimates of irradiated tissue samples using
the PSF subtraction Model - contrasted with the outcome of the
picosirius red staining technique**

T_{app} (°C)	optical inactivity detected	T_{model} (°C)
40	No	64.0
41	No	63.75
42	No	65.5
43	No	67.0
44	No	67.25
45	Yes	70.0
46	No	69.75
47	Yes	71.75
48	Yes	72.0
49	Yes	72.5
50	Yes	73.25

7.3: (iii): Conclusions

The temperature estimated by the model at the transition temperature is 4 - 5 °C greater than expected. By considering the other results, this is quite

clearly a systematic error. The computer output from the sample with $T_{app} = 45\text{ }^{\circ}\text{C}$ is shown in Fig. 7.15 and this gives a clue as to where the systematic error comes from.

The figure suggests that the laser energy gave rise to something approaching a constant temperature source, which is very unlikely to be the case. The most likely explanation is related to the edge effect which was discussed in the previous section. The PSF has a range of 6 mm or 200 pixels on the computer screen, so the deconvolution wont begin for 100 pixels in from the edge of the detected image. This is most likely to be too strict a restraint and although it does not give rise to the “spikes” observed in the Gaussian distributions, it does give rise to the overestimation’s which were present in the constant temperature source deconvolutions. This suggests that the temperature distribution is closer to a step function than a Gaussian function.

Varying the value of the range of the PSF has a major effect on the temperature estimate and decreasing this value leads to a reduction in the temperature estimate. For future work then, either the effect of the source width on the PSF range should be considered or, if the experimental set-up is similar for each image, correction factors should be applied. However, the error involved here is a vast improvement on the error recorded when the apparent temperature is taken at face value, that is $\approx 20\text{ }^{\circ}\text{C}$.

BFIG715.BMP

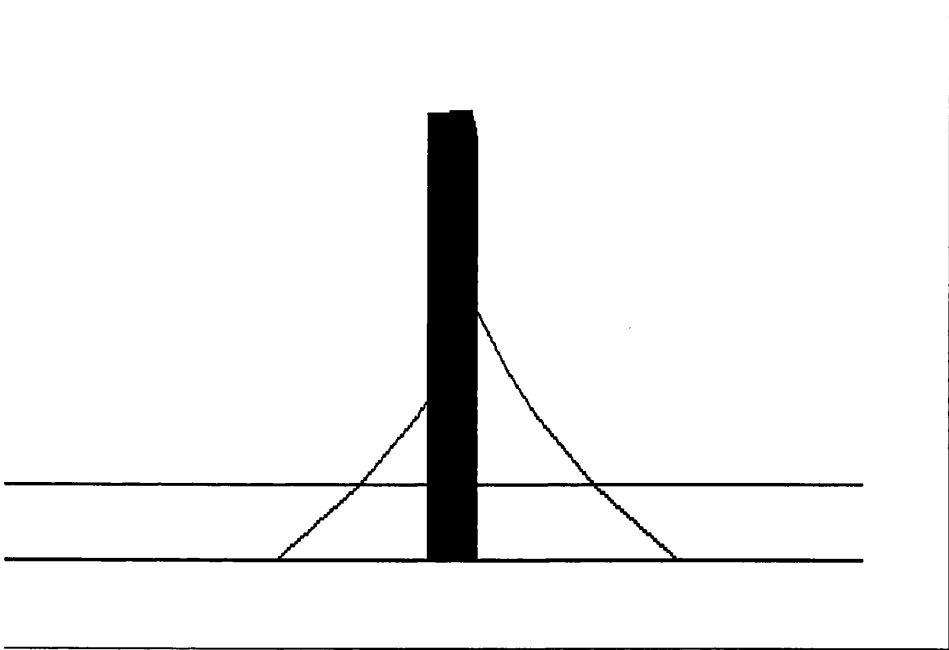


Fig. 7.15: Computer output for estimation of temperature of tissue irradiated by laser energy

CHAPTER 8:

CONCLUSIONS

The aim of this thesis has been to assess the reliability of the pyro-electric vidicon (PEV) as a remote temperature measuring device during laser assisted vascular anastomosis (LAVA), although, more generally, the principles apply to any thermal imager, used to measure temperature at the site of a laser-tissue interaction. Having ascertained the limitations of the PEV, a computational model was developed to provide a means of accurately determining the temperature at the bond site.

Table 1.3 and 2.1 summarise the results of our LAVA investigations and investigations by other authors, respectively. These findings show the technique to have potential but to suffer from inconsistency. However, it is difficult to make direct comparisons of the published work as many parameters vary between publications:

- type of laser
- type of blood vessel
- type of bond (see Fig. 2.1)

- degree of apposition of vessel walls
- applied energy density
- temperature achieved at bond site.

Thermal imagers have been applied by some authors in order to measure and control the temperatures achieved. The accurate measurement of temperature is necessary if the bonding mechanism is to be understood and if the optimal bond temperature is to be ascertained. However, this task cannot be carried out successfully if the limitations of the imager are not considered.

Thermal imagers have found widespread application in areas outwith medicine and they provide a reliable method for the detection of areas of increased temperature in fire-fighting and the defence industry. However, often in medical and industrial applications, the absolute temperature of the source is required. In particular, when measuring the temperature of industrial materials, it is of great importance to know the emissivity of the material. The temperature range of the imager will be calibrated using a black body source and, hence, materials of emissivity less than 1 will have their temperatures underestimated. This factor is of less importance in medical applications as the emissivity of tissue is very close to unity (see Table 3.1). For this reason correction factors for emissivity were not considered in the work presented here.

Of much greater importance, is the resolution limit of the imager and if no account is taken of it, Then the measured temperatures will be seriously underestimated. Figs. 4.10 - 4.13 illustrate the effect on the temperature estimation when imaging sources which are smaller than the resolution limit of the imager. As the measured resolution limit is 6 mm for the PEV and the laser spot diameter is approximately 1.5 mm, it is apparent that the tissue temperatures will be seriously underestimated. This principle also applies to photon detectors which have a greater resolving power but are correspondingly more expensive.

In order to take this effect into account a computational model was developed to estimate the "true" tissue temperature. This alone gives no idea of the accuracy of the model and a further independent technique was sought which would allow us to ascertain the accuracy of the technique. Micro-thermocouples were shown to be highly unreliable and the DSC technique to be very inaccurate. The technique of choice then was the picrosirius red staining technique. It was shown that when viewed with polarised light, the stained tissue lost its optical activity at $65.5 (\pm 0.5) ^\circ\text{C}$ and this then allowed us to say unequivocally whether or not tissue which had been subject to laser irradiation had reached this threshold temperature.

The computational model developed was dependent on the PSF being accurately known. This was found by two independent methods described in section 6.4 and the results were in very close agreement.

Two approaches to deconvolution were then taken using the PSF. In the first approach, the image was redistributed using the PSF distribution as a weighting factor. However, an estimate of the source width was required before the image could be redistributed and, not surprisingly, this worked well for constant temperature sources but not for Gaussian sources.

The second model developed (the PSF subtraction model), scanned the image distribution pixel by pixel and subtracted a PSF representation from the image each time the PSF fitted under the image curve. The inferred source distribution was then gradually built up until no more PSF representations could be subtracted. This proved to be a better model for Gaussian distributions.

When applied to laser-irradiated tissue, a systematic error of 4 - 5 °C appeared in the temperature estimates. This could not be due to the other sources of errors which arise at various stages:

(a) When setting up the imager, it is important to be as close to the focal plane as possible and the source must be central to the image such that the plane under analysis lies along the central line displayed on the monitor (Fig 4.4). The gain and black level must be set carefully so that the required

temperature is achieved. This range is set relative to a black body source, which, in reality, will have an emissivity of slightly less than 1.

The overall contribution to the error is estimated to be no more than ± 1 °C from the combined effects of the aforementioned factors

(b) The tissue emissivity relative to the black body source will have a small contribution to the error. As noted in section 4.4(v), the angle between the normal to the tissue and the line of sight of the imager must be less than 30 ° to avoid underestimation's. This is not significant for our set-up but may be significant in a clinical situation when arteries or any curved surface is being viewed. Further complications here could arise if the surfaces being bonded are not carefully apposed and they must be under sufficient tension to avoid distortion when irradiated with laser energy.

However, in our laboratory set-up, the overall contribution is estimated at ± 0.5 °C, though it must be considered in more detail for each particular clinical set-up.

(c)The actual reading of the video signal will contribute to the overall error. This is compounded by the fact that the signal must be read from a video recorder on freeze-frame mode. This adds significantly more noise to the input of the oscilloscope which is used for the final output reading.

It estimated to contribute no more than ± 1 °C to the overall error.

(d) Once the image temperature distribution is entered in to the computational model, the image must be extrapolated to room temperature. This provides another source of error as does the actual measurement of room temperature.

Again, these factors should contribute no more than ± 1 °C to the overall error.

(e) Finally, there is the error arising from the deconvolution program. This appears to be the overwhelming factor when considering the error. Combining (a) - (b) we arrive at an overall error of ± 1.8 °C which does not nearly account for the observed error, which is quite clearly a systematic error.

For future work, it would be advisable to look at this in more detail . It seems likely that, although the PSF covers an equivalent diameter of 6 mm, the contribution at the outer edges may be so small as to be negligible for low temperatures and / or small sources. This may then bring about a greater accuracy.

Another aspect to consider would be to make the process more user-friendly with a view to automating the technique. This would minimise the risk of mistakes being made and bring it closer to real time analysis.

Instead of feeding the signal into a video recorder and oscilloscope, the signal could be fed directly to an image analysis system which has the facility for grabbing images and performing the deconvolution analysis. Although this would make the whole system very bulky for an operating theatre, recent improvements in computer power would allow this to be carried out on a personal computer.

To sum up then, the error of 5 °C could still lead to confusion when attempting to understand the bonding mechanism. However, as the error is fairly well known and seems to be repeatable, it can easily be accounted for. This would lead to temperatures being estimated to an accuracy of ± 2 °C which represents a considerable improvement on the previous uncorrected estimates.

Appendix

Derivation of temperature rise, ΔT , in tissue due to energy

deposition:

For transient conditions, ignoring conduction

$$\Delta T = \Delta T_0 \exp(-a_0 z)$$

$$\begin{aligned} \text{Apparent temperature rise, } \Delta T_a &= \Delta T_0 a_i \int_0^{\infty} \exp(-a_0 z) \exp(-a_i z) dz \\ &= \Delta T_0 a_i \int_0^{\infty} \exp[-(a_0 + a_i)z] dz \\ &= \Delta T_0 \frac{a_i}{a_i + a_0} \end{aligned}$$

Approximate transit time of heat energy

Rearranging

$$H = \frac{dQ}{dt} = k A \frac{dT}{dx}$$

and

$$C = \frac{dQ}{dT}$$

where Q = heat energy, t = time, k = thermal conductivity, A = cross-sectional area, T = temperature, x = depth and C = specific heat.

$$dt = \frac{dQ}{kA \frac{dT}{dx}} = \frac{CdT}{kA \frac{dT}{dx}} = \frac{Cdx}{kA}$$

List of references

[1] A. EINSTEIN: Zur quantentheorie der strahlung. Phys. S.Z., 18, 121-128, 1917. (Reprinted in F.S BARNES: Laser theory, IEEE Press, New York, 1972).

[2] T.H. MAIMAN: Stimulated optical radiation in ruby. Nature, 187, 493-494, 1960.

[3] J.P. GORDON, H.J. ZEIGER & C.H. TOWNES: The maser - new type of microwave amplifier, frequency standard and spectrometer, Physical Review, 99(4), 1264-1274, 1955.

[4] A.H. SCHAWLOW & C.H. TOWNES: Infrared and optical masers, Physical Review, 112(2), 1940, 1958.

[5] D.C O'SHEA, W.R CALLEN & W.T. RHODES: Introduction to lasers and their applications, Addison-Wesley Publishing Company, 1978.

[6] F.A. L'ESPERANCE: Research on a new target for thermal television, Advances in electron. and electron. phys., Proc. 4th Symp. Photo-electron. image devices, 28, 256-272, 1969.

[7] T.A. FULLER: The characteristics in operation of surgical lasers, Surgical Clinics of North America, 64(5), 843-849, 1984.

[8] J.T. WALSH & T.F. DEUTSCH: Pulsed CO₂ laser ablation of tissue: Effect of mechanical properties, IEEE Transactions on biomedical engineering, 36(12), 1195-1201, 1989.

[9] T.J. DOUGHERTY, D.G. BOYLE, K.R. WEISHAUFT, et al: Photoradiation therapy-clinical and drug advances, Adv. Exp. Med. Biol, 160-163, 1983.

[10] H.D. MCINTOSH & J.A. GARCIA: The first decade of aortacoronary by-pass grafting 1967-1977: a review, Circulation, 57, 405, 1978.

[11] R.D. JENKINS, N. SINCLAIR, R. ANAND, et al, Laser balloon Angioplasty: Effect of tissue temperature on weld strength of human post-

mortem intime-media separations, *Lasers in Surgery and Medicine*, 8, 30-39, 1988.

[12] A. ROSEN, P. WALINSKY, D. SMITH, et al: Percutaneous transluminal microwave angioplasty catheter, *IEEE MTT-s Digest*, D-1, 167-169, 1989.

[13] A.J. WELSH, A.B. BRADLEY & J.H. TORRES: Laser probe ablation of normal and atherosclerotic human aorta in vitro: a first thermographic and histologic analysis, *Circulation*, 5 1353-1363, 1987.

[14] R.A. WHITE & W.S. GRUNDFEST: *Lasers in cardiovascular disease*, Year Book Medical Publishers, Inc., 1987.

[15] K.K. JAIN & W. GORISCH: Repair of small blood vessels with the Neodymium-YAG laser: A preliminary report, *Surgery*, 85(6), 684-688, 1979.

[16] to be published (D. Taggart, J.W. Fenner, B.J.Gibson, et al)

[17] J.W.E. BRYDON, A.K. LAMBIE & D.J. WHEATLEY: Thermographic visualisation of coronary artery blood flow during by-pass surgery, *Journal of Medical Engineering and Technology*, 3(2), 1979.

[18] A. SERURE, E.H. WITHERS, S. THOMSEN & J. MORRIS: Comparison of carbon dioxide laser-assisted microvascular anastomoses and conventional microvascular sutured anastomoses, *Surgical Forum*, 34, 634-636, 1984.

[19] R. SCHOBBER, F. ULRICH, T. SANDER, et al: Laser-induced alteration of collagen substructure allows microsurgical tissue welding, *Science*, 232, 1421-1422, 1986.

[20] A.F. BADEAU, C.E. LEE & J.R. MORRIS: Temperature response during microvascular anastomoses using milliwatt CO₂ lasers, *Lasers in Surgery and Medicine*, 6, 179, 1986.

[21] G. KOPCHOK, W.S. GRUNDFEST, R.A. WHITE, et al: Argon laser vascular welding: the thermal component, *Lasers in Medicine*, 712, 260-263, 1986.

[22] J. FENNER, W. MARTIN, H. MOSELEY & D.J. WHEATLEY: Shear strength of tissue bonds as a function of bonding temperature: a proposed mechanism for laser assisted tissue welding: *Lasers in Medical Science*, 7, 39-43, 1992.

[23] M. OKADA, K. SHIMIZU, H. IKUTA, et al: An alternative method of vascular anastomoses by laser: Experimental and clinical study, *Lasers in Surgery and Medicine*, 7, 240-248, 1987.

[24] R.A. WHITE, G.H. WHITE R.M. FUJITANI, et al: Initial human evaluation of argon laser-assisted vascular anastomoses, *Journal of Vascular Surgery*, 9(4), 542-547, 1989.

[25] M. GENNARO, E. ASCER, C. MOHAN & S. WANG: A comparison of CO₂ laser-assisted anastomoses and conventional suture techniques: patency, aneurysm formation and histologic differences, *Journal of Vascular Surgery*, 14, 605-613, 1991.

[26] P.F. LAWRENCE, K. LI, S.W. MERRELL & G.R. GOODMAN: A comparison of absorbable suture and argon laser welding for lateral repair of arteries, *Journal of Vascular Surgery*, 14, 184-189, 1991.

[27] J.H. FRAZIER, G.A. PAINVIN, J.R. MORRIS, et al: Laser-assisted microvascular anastomoses: angiographic and anatomopathologic studies on growing microvascular anastomoses: preliminary report, *Surgery*, 97(5), 585-589, 1984.

[28] J.V. WHITE, M.C. DALSING, S.T. JAMES, et al: Tissue fusion effects of the CO₂ laser, *Surgical Forum*, 36,455-457, 1985.

[29] S. NAKATA, C.D. CAMPBELL, R. PICK & R.L. REPLOGLE: End-to-side and end-to-end vascular anastomoses with a carbon dioxide laser, *Journal of Thoracic and Cardiovascular Surgery*, 98, 57-62, 1989.

[30] E.M. ASHWORTH, M.C. DALSING & J.F. OLSEN: Large artery welding with a milliwatt carbondioxide laser, *Archives of Surgery*, 122, 673-677, 1987.

[31] R.A. WHITE, R.P. ABERGEL, R. LYONS, et al: Biological effects of laser welding on vascular healing, *Lasers in Surgery and Medicine*, 6, 137-141, 1986.

[32] K.H. NIJIMA, Y. YONEKAWA, H. HANDA & W. TAKI: Nonsuture microvascular anastomosis using a Nd-YAG laser and a water soluble polyvinyl alcohol splint, *Journal of Neurosurgery*, 7, 240-248, 1987.

[33] Y. KUROYANAGI, M. TAGUCHI, T. YANO, et al: Argon laser-assisted anastomoses in medium size vessels: one year follow-up, *Lasers in Surgery and Medicine*, 11, 223-231, 1991.

[34] P.I. ANDROSOV: New method of surgical treatment of blood vessel lesions, *Archives of Surgery*, 73, 902-910, 1956.

[35] H.S. NATHAN, M.N. NACHLAS, R.D. SOLOMON, et al: Nonsuture closure of arterial incisions using a rapidly polymerising adhesive, *Annals of Surgery*, 152(4), 648-659, 1960.

[36] B. SIGEL & F.J. ACEVEDO: Electrocoaptive union of blood vessels, *Journal of Surgical Research*, 3(2), 90-96, 1963.

[37] S. STEEN, L. ANDERSSON, P. LOWENHEILM, et al: Comparison between absorbable and nonabsorbable, monofilament sutures for end-to-end arterial anastomoses in growing pigs, *Surgery*, 95(2), 202-207, 1983.

[38] R.M. STILLMAN & Z. SOPHIE: Repair of growing vessels: Continuous absorbable or interrupted non-absorbable suture, *Archives of Surgery*, 120, 1281-1283, 1985.

[39] I.S. CHIU, C.R. HUNG, S.F. CHAO, et al: Growth of the aortic anastomosis in pigs: Comparison of continuous absorbable suture with non-absorbable suture, *Journal of Thoracic and Cardiovascular Surgery*, 95, 112-118, 1988.

[40] R.G.F. TAYLOR & H.A.H. BOOT: Pyroelectric image tubes, *Contemporary Physics*, 14, 55-87, 1973.

[41] A.L. STANFORD Jr: Detection of electromagnetic radiation using the pyroelectric effect, *Solid State Electronics*, 8, 747-755, 1965.

[42] WOLFE & ZISSIS: *The Infrared Handbook*, The IR Information and Analysis Centre, Environmental Research Institute of Michigan, 1978.

[43] BURNAY, WILLIAMS & JONES: *Applications of Thermal Imaging*, Adam Hilger, 1988.

[44] J. COOPER: A fast response pyroelectric thermal detector, *Journal of Scientific Instrumentation*, 39, 467-472, 1962.

[45] A.G. CHYNOWETH: Dynamic method for measuring the pyroelectric effect with special reference to barium titanate, *Journal of Applied Physics*, 27, 78-84, 1956.

[46] R.W. ASTHEIMER & F. SCHWARZ: Thermal imaging using pyroelectric detectors, *Applied Optics*, 7(9), 1687-1695, 1968.

[47] E.H. PUTLEY: Solid state devices for infrared detection, *Journal of Scientific Instrumentation*, 43, 857-868, 1966.

[48] E.M. WORMSER: Sensing the invisible world, *Applied Optics*, 7, 1667-1671, 1968.

[49] S.S. BORG: Thermal imaging using pyroelectric detectors, *Applied Optics*, 7, 1697-1703, 1968.

[50] R.V. JONES: Infrared detection in British Air Defence, 1935-38, *Infrared Physics*, 1, 153-162, 1961.

[51] F. LeCARVENNEC: Research on a new target for thermal television, *Advances in Electronics and Electronic Physics*, Proceedings of 4th Symposium Photo-electronic imaging devices, 28, 256-272, 1969.

[52] M.F. TOMPSETT: A pyroelectric thermal imaging camera tube, *IEEE Transactions on Electron Devices*, 18(11), 1070-1074, 1971.

[53] B.R. HOLEMAN & W.M. WREATHALL: Thermal imaging camera tubes with pyroelectric target, *Journal of Physics D: Applied Physics*, 4, 1898-1909, 1971.

[54] E.H. PUTLEY, R. WATTON, W.M. WREATHALL & S.D. SAVAGE: Thermal imaging with pyroelectric television tubes, *Advances in Electronics and Electronic physics*, 33A, 285-292, 1972.

[55] R. WATTON, D. BURGESS & P. NELSON: The thermal behavior of reticulated targets in the pyroelectric vidicon, *Infrared Physics*, 19, 683-688, 1979.

[56] C.H. JONES: Medical thermography, *IEE Proceedings*, 134, A2, 225-236, 1987.

[57] H.G. LUBSZYNSKI, S. TAYLOR & J. WARDLEY: Some aspects of vidicon performance, *Journal of British Institute Radio Engineers*, 20(5), 1960.

[58] B. HARPER & T. NORMAN: Recent advances in pyroelectric thermal imaging relevant to medical thermography, *Journal of Photographic Science*, 37, 175-178, 1989.

[59] L.E. GARN & E.J SHARP: Pyroelectric vidicon target materials, *IEEE Transactions on parts, hybrids and packaging*, 208-221, 1974.

[60] R. WATTON: Infrared television: Thermal imaging with the pyroelectric vidicon, *Physical Technology*, 11, 62-66, 1980.

[61] J.D. HARDY & C. MUSCHENHEIM: The radiation of heat from the human body IV The emission, reflection and transmission of infrared radiation by the human skin, *Journal of Clinical Investigation*, 13, 817-831, 1934.

[62] R. ELAM, D.W. GOODWIN & K.L. WILLIAMS: Optical properties of the human epidermis, *Nature*, 198, 4884 1963.

[63] D.J. WATMOUGH & R. OLIVER: Emissivity of human skin in the waveband between 2 and 6 μm , *Nature*, 219, 622-624, 1968.

[64] P.MITCHELL, C.H. WYNDHAM, T. HODGSON, et al: Measurement of the total normal emissivity of skin without the need for measuring skin temperature, *Physics in Medicine and Biology*, 12(3), 359-366, 1967.

[65] J. STEKETEE: Spectral emissivity of skin and pericardium, *Physics in Medicine and Biology*, 18(5), 686-694, 1973.

[66] A.J. WELSH, A.B. BRADLEY, J.H. TORRES, et al: Laser probe ablation of normal and atherosclerotic human aorta in vitro: a first thermographic and histologic analysis, *Circulation*, 76(5), 1353-1363, 1987.

[67] M. ANBAR & S. HEJAZI: The black body behaviour of human skin, *International Congress of Thermology*, abstract, 1992.

[68] J. H. TORRES, T.A. SPRINGER, A.J. WELSH & J.A. PEARCE: Limitations of a thermal camera in measuring surface temperature of laser-irradiated tissue, *Lasers in Surgery and Medicine*, 10, 510-523, 1990.

[69] D.J. MACEY & R. OLIVER: Image resolution in infrared thermography, *Physics in Medicine and Biology*, 17(4), 563-571, 1972.

[70] G.E. KOPCHOK, R.A. WHITE, G.H. WHITE, et al: CO₂ and argon laser vascular welding: acute histologic and thermodynamic comparison, *Lasers in Surgery and Medicine*, 8, 584-588, 1988.

[71] E.M.B. SORENSEN, S. THOMSEN, A.J. WELSH & A.F. BADEAU: Morphological and surface temperature changes in femoral arteries following laser irradiation, *Lasers in Surgery and Medicine*, 7, 249-257, 1987.

[72] C.A. VANCE, J. FISHER, D.J. WHEATLEY, et al: Laser assisted vessel anastomosis of coronary arteries in vitro: optimization of bonding conditions, *Lasers in Medical Science*, 3, 219-227, 1988.

[73] R. MARCHESINI, S. ANDREOLA, H. EMANUELLI, et al: Temperature rise in biological tissue during Nd:YAG laser irradiation, *Lasers in Surgery and Medicine*, 7, 307-329, 1987.

[74] J. MNITENTAG, E.F. MARQUES, M.P. RIBEIRO, et al: Thermographic study of laser on arteries, *Lasers in Surgery and Medicine*, 7, 307, 307-329, 1987.

[75] S. WEBB (ed.): The Physics of Medical Imaging, Institute of Physics Publishing, Bristol and Philadelphia, 1988.

[76] J. CREZEE & J.J.W. LAGENDIJK: Experimental verification of bioheat transfer theories: measurement of temperature profiles around large artificial vessels in perfused tissue, *Physics in Medicine and Biology*, 35(7), 905-923, 1990.

[77] P.E. MCCLAIN, & E.R. WILEY: Differential Scanning Calorimeter Studies of the thermal transitions of collagen, *Journal of Biological Chemistry*, 247(3), 692-697, 1972.

[78] J. WOODHEAD-GALLOWAY: Collagen: the anatomy of a protein, Edward Arnold Ltd., 1980.

[79] G.M. BERNACCA, W.R. DIMIRTI, A.C. FISHER, et al, Chemical modification of bovine pericardium and its effect on calcification in the rat subdermal model, *Biomaterials*, 13(6), 345-352, 1992.

[80] L.C.U. JUNQUEIRA, G. BIGNOLAS & R.R. BRENTANI: Picrosirius staining plus polarization microscopy, a specific method for collagen detection in tissue sections, *Histochemical Journal*, 11, 447-455, 1979.

[81] S.G. BROOKS, S. ASHLEY, H. WRIGHT, et al: The histological measurement of laser-induced thermal damage in vascular tissue using the stain picrosirius red F3BA, *Lasers in Medical Science*, 6, 399-405, 1991.

[82] F.A. DUCK: Physical Properties of Tissue: A comprehensive reference book, Academic Press, 1990.

[83] D.J. WATMOUGH, P.W. FOWLER & R. OLIVER: The thermal scanning of a curved isothermal surface: Implications for clinical thermography, *Physics in Medicine and Biology*, 15(1), 1-8, 1970.

[84] R.WATTON, C. SMITH, B. HARPER & W.M. WREATHALL: Performance of the pyroelectric vidicon for thermal imaging in the 8-14

micron band, IEEE Transactions on Electron Devices, 21(8), 462-469, 1974.

[85] W.G. CADY: Piezoelectricity, M^cGraw-Hill Book Company, Inc., 1946.

